CENTRO DE INVESTIGACIONES EN ÓPTICA A.C.

Luminescence Properties of $ZrO_2:Yb^{3+} – Er^{3+}$ Nanocrystals

THESIS SUBMITTED AS PARTIAL FULFILLMENT OF THE REQUIREMENTS FOR THE DEGREE OF MASTER OF SCIENCE (OPTICS) AT CENTRO DE INVESTIGACIONES EN ÓPTICA

By

DAVID O. SOLÍS SANTANA

B. in Electronic Engineering

Advisor:

Dr. ELDER DE LA ROSA CRUZ

Researcher at C.I.O.

LEÓN, GTO., MÉXICO **AUGUST 2006**

I gratefully appreciate the support and assistance from:

My advisor Dr. Elder de la Rosa and Dr. Luis A. Diaz by their supervising and guiding for this work and share their knowledge during my permanence at C.I.O.

Dr. Pedro Salas, Dr. Carlos Angeles Chávez and Dr. Ascención Montoya, at I.M.P., for their help in the XRD, TEM and HRTEM characterization.

CONACyT as this work is supported by its scholarship.

My colleague Luis Meza for his collaboration in the workable algorithm programs implemented.

Tzarara López because of her cooperation.

Summary

Sixteen ZrO_2 nanocrystalline samples, single and codoped, with different concentrations of Erbium and Ytterbium ions were synthesized by sol-gel method and annealed for 5 h. at 1000 ºC. ZrO_2: The strongest measured Yb^{3+} (2%), Er^{3+} (1%) codoped sample presented 100% tetragonal phase with a crystallite size of ~ 78 nm. The structural and morphological characterization showed that the introduction of different ion concentrations affect the crystalline structure stability. The samples were pumped at 968 nm with a semiconductor laser source. The up-converted luminescence properties and the change in the peak intensities of the measured green and red bands were studied. These bands can be ascribed to the $^2H_{11/2} + {}^4S_{3/2} \rightarrow {}^4I_{15/2}$ and $^4F_{9/2} \rightarrow {}^4I_{15/2}$ Erbium transitions. With this research work it is expected to have control of the intensity variations of the peaks by changing the Yb^{3+} and Er^{3+} dopant concentrations. Thus, the strongest red emission signal was obtained for the ZrO_2: Yb^{3+} (4%), Er^{3+} (1%) codoped sample and the red and green emission bands had a relationship of 636:100. The ZrO_2: Yb^{3+} (10%), Er^{3+} (1%) sample was suitable for almost pure red emission, with a ratio value of 13.56 times the green emission. Unfortunately the total emission was 80% weaker compared with the strongest measured ZrO_2: Yb^{3+} (2%), Er^{3+} (1%) sample. In codoped samples the red/green ratio is dominated by cross relaxation (CR) process, i.e. $(^2H_{11/2} + {}^4S_{3/2} \rightarrow {}^4I_{9/2}) + ({}^4I_{15/2} \rightarrow {}^4I_{13/2})$. For the red enhancement we found that the dopant concentration ratio value was not unique, that is, we found that more than one dopant concentration value ratio for different red enhancement. Therefore we proved that it is possible to control the red/green emission ratio in ZrO_2:Yb^{3+}, Er^{3+} nanophosphors and get enhancement of the red emission.

16 muestras nanocristalinas de ZrO_2, dopadas y codopadas con diferentes concentraciones de iones de Erbio e Yterbio fueron preparadas por el método de sol-gel y calcinadas por 5 h a 1000 ºC. La muestra más intensa, correspondiente a Yb^{3+} (2%) Er^{3+} (1%), presentó 100% de fase tetragonal y un tamaño de cristal de aproximadamente 78 nm. La caracterización estructural y morfológica mostró que la introducción de iones a diferentes concentraciones afecta la estabilidad de la estructura cristalina. Las muestras fueron excitadas con un láser de semiconductor a 968 mn. Las propiedades luminiscentes y el cambio de intensidades de las bandas verde y roja fueron estudiadas. Dichas bandas están relacionadas a las transiciones del Erbio $^2H_{11/2} + {}^4S_{3/2} \rightarrow {}^4I_{15/2}$ y $^4F_{9/2} \rightarrow {}^4I_{15/2}$. En este trabajo se espera tener control de la variación de las intensidades modificando la concentración de dopantes. De esta forma, la emisión roja más intensa fue obtenida con la muestra ZrO_2: Yb^{3+} (4%), Er^{3+} (1%) con una relación entre bandas roja y verde de 636:100. La muestra ZrO_2: Yb^{3+} (10%), Er^{3+} (1%) resultó con una emisión prácticamente roja, con una razón 13.56 veces más intensa que la emisión verde; aunque la emisión fue 80% más débil comparada con la muestra más intensa ZrO_2: Yb^{3+} (2%), Er^{3+} (1%). En las muestras codopadas la razón verde/rojo es dominada por el proceso de relajación cruzada (CR), i.e. $(^2H_{11/2} + {}^4S_{3/2} \rightarrow {}^4I_{9/2}) + ({}^4I_{15/2} \rightarrow {}^4I_{13/2})$. Para el mejoramiento de la emisión roja se encontró que la razón entre concentraciones no era única; sin embargo es posible el control de la razón entre bandas roja/verde en los nanofósforos de ZrO_2:Yb^{3+}, Er^{3+} e incrementar la emisión roja.

Preface

Introduction

The word *phosphor* appeared around the 17th century and its meaning remains unchanged. After the discovery of the "Bolognian stone", similar ones were reported from several places in Europe and these light-emitting stones were named *phosphors*. Finally, the word *luminescence* was first introduced in 1888 and initiates, in this way, a new field of knowledge. Nowadays, the word *luminescence* is defined as a phenomenon in which the electronic state of a substance is excited by some kind of external energy and the excitation energy is given off as light.

At the present time, the major and important applications of phosphors are displays, solid state lighting, amplifiers, image converters in medicine, dosimetry, sensors, solar cells, fuel cells, catalysis, photo detectors, cutting tools, optical memories, biology, cosmetics, etc. Research and development of these applications belong to the fields of illuminating engineering, electronics, chemistry, solid-state physics, and image engineering. However, these materials, and others, in the nanometer scale may exhibit physical properties distinctively different from that of bulk. That is to say, materials in this size range exhibit

some remarkable specific properties and due to that fact, actually has become a consolidated research field.

In general, nanotechnology can be understood as a technology of design, fabrication and applications of nanostructures and nanomaterials. Nanotechnology also includes essential understanding of fundamental relationships between physical properties and phenomena and material dimensions in the nanometer scale.

Although research in nanostructured materials began over two decades ago, it was until the late 1990s that the first significant results were reported. Today, nanostructured materials and nanotechnology have major significance for both fundamental and technical research. These new kind of materials can adopt different forms: nanoparticles, nanocrystals, nanotubes, nanowires, nanorods, etc. They can be produced from semiconductors, dielectrics, metals, organic and inorganics; also including alloys, hybrids, polymers, etc. The advances, applications and importance of nanostructures will become the day-to-day nanotechnology of the future.

This thesis work is centred in *upconverted luminescence variation by changing dopant concentration of Yb^{3+} and Er^{3+} rare-earth ions on zirconium nanocrystals in addition to control the produced up-conversion, particularly in the enhancement of red emission*. Several aspects have been earned during the development of this work in order to achieve the purpose proposed. Some of them are the understanding and knowledge acquired over the sol-gel process for the nanocrystals preparation; the ability to use spectroscopy instrumentation and awareness over the analysis process. According to that, Chapter 1 is considered to present the basic terminology used about phosphors and a glance on nanophotonics, as it is the field of interest. Also in the chapter are shown the fundamentals about nanoscale electronic interactions, some of which were taken into account to enhance on samples elaborated for this work. Following in Chapter 2 is shortly examined the ability to fabricate and process nanomaterials and nanostructures, as is the first corner stone in nanotechnology. Many technologies have been applied and these technical approaches can be grouped in several ways. In Chapter 3 it is shown the sol-gel process and the derived synthesis procedure used for these nanocrystals. Likewise, in order to explore novel physical properties and realize potential applications of nanostructures and nanomaterials, this chapter briefly describes the characterization methods that were employed for this intention. The luminescence properties of ZrO_2:Yb^{3+}– Er^{3+} nanocrystals are presented in Chapter 4. Properties of Yb–Er samples are reported as the same as others doped only with either erbium or ytterbium. Finally, in Chapter 5 the experimental results are disclosed, and conclusions about the acquired data are explained.

With this thesis work it is tried to achieve an applicable result on ZrO_2:Yb^{3+}– Er^{3+} nanocrystals. I hope that goal had been accomplished.

Contents

Chapter 1

Nanoposphors' Properties

1.1. TERMINOLOGY

Prior to enter in more complex concepts, it is considered necessary to give a brief explanation about the origin and meaning of the terminology related to phosphors.

The word phosphor appeared around the 17th century and its meaning remains unchanged. It is considered that, Vincentinus Casciarolo of Bologna, Italy, was the person who found a heavy crystalline stone with a gloss at the foot of a volcano, and fired it in a charcoal oven intending to convert it to a noble metal. Casciarolo obtained no metals but found that the sintered stone emitted red light in the dark after exposure to sunlight, became know as the "Bolognian stone". The stone found appears to have been barite ($BaSO_4$), and the fired product BaS, which is now known to be a host for phosphor materials.

After this discovery, similar ones were reported from several places in Europe, and these light-emitting stones were named *phosphors*, that means "light bearer" in Greek. The word *phosphorescence* was derived from the word phosphor, and is used to denote a long after-glow of a few hours, that is, persisting light emission from a substance after the exciting radiation has ceased. The word *fluorescence* was introduced to distinguish the emission from phosphorescence and denotes the imperceptible short after-glow of the mineral fluorite (CaF_2) following excitation. Finally, the word *luminescence*, which includes both fluorescence and phosphorescence, was first used by Eilhardt Wiedemann, a German physicist, in 1888. This word originates from the Latin word lumen, which means light.

Presently, the word *luminescence* is defined as a phenomenon in which the electronic state of a substance is excited by some kind of external energy and the excitation energy is given off as light. Here, the word light includes not only electromagnetic waves in the visible region of 400 to 700 nm, but also the near-ultraviolet and the near-infrared regions.

In modern usage, light emission from a substance during the time when it is exposed to exciting radiation is called *fluorescence*, while the after-glow if detectable by the human eye after the cessation of excitation is called *phosphorescence*. However, it should be noted that these definitions are applied only to inorganic materials; for organic molecules, different terminology is used. For organics, light emission from a singlet excited state is called fluorescence, while that from a triplet excited state is defined as phosphorescence.

The definition of the word phosphor itself is not clearly defined and usually means inorganic phosphors, like those in powder form and synthesized for practical applications. Single crystals, thin films, and organic molecules that exhibit luminescence are rarely called phosphors. In a broader sense, the word phosphor is equivalent to "solid luminescent material."

1.2. APPLICATIONS OF PHOSPHORS

The major and important applications of phosphors are in light sources, display devices, and detector systems. Research and development of these applications belong to the fields of illuminating engineering, electronics, chemistry, solid-state physics, and image engineering.

The applications of phosphors can be classified according to the excitation source for the phosphors. Figure 1.1 lists various kinds of phosphor devices according to the method used to excite the phosphor [1]. It gives a summary of phosphor devices by the manner in which the phosphors are applied.

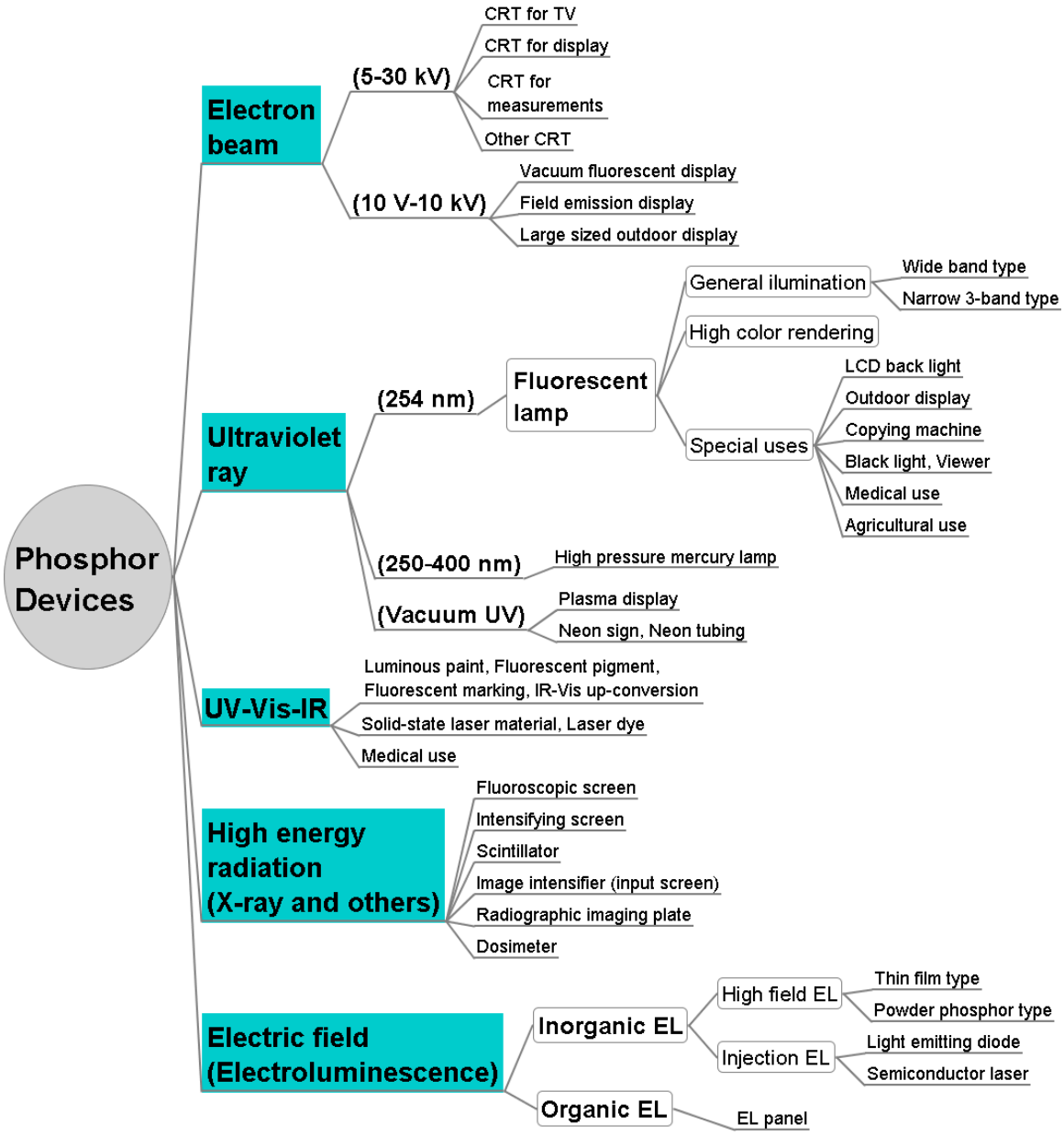

Figure 1.1: Phosphor devices [2].

The main interest of this thesis work is over UV-VIS-IR excited phosphors, in order to develop light sources and detector systems based on the up-conversion phenomena. Due to the fact that luminescence is involved in the desired purpose, a good apply of enhanced photonics properties would be adequate.

1.3. BRIEF GLANCE ON NANOPHOTONICS

Nanotechnology deals with small structures or small-sized materials. The typical dimension spans from subnanometer to several hundred nanometers. Materials in the micrometer scale mostly exhibit physical properties the same as that of bulk form; however, materials in the nanometer scale may exhibit physical properties distinctively different from that of bulk. Materials in this size range exhibit some remarkable specific properties; a transition from atoms or molecules to bulk form takes place in this size range.

In general, nanotechnology can be understood as a technology of design, fabrication and applications of nanostructures and nanomaterials. Nanotechnology also includes essential understanding of fundamental relationships between physical properties and phenomena and material dimensions in the nanometer scale, is also referred to as nanoscience.

According to the above concept, nanophotonics could be defined by the fusion of nanotechnology and photonics. It deals with the interaction of light with matter on nanometer size scale. Nanophotonics can conceptually be classified in three ways of interactions: nanoscale confinement of radiation, nanoscale confinement of matter and nanoscale photo processes. The first one confines light to nanoscale dimensions much smaller than the wavelength of light. The second approach limits interactions between light and matter to nanoscopic dimensions. This defines the field of nanomaterials. The last way induces photochemistry or light-induced phase change. This approach provides methods for nanofabrication of photonic structures [3].

To make nanomaterials for photonics, various ways are used for confining the dimensions of matter [3]. Nanoparticles can be made of either inorganic or organic materials. Nanomers, which are nanometer size of monomeric organic structures, are organic analogues of nanoparticles and also exhibit size-dependent optical properties. Metallic nanoparticles exhibit unique optical response and enhanced electromagnetic field and constitute the area of "plasmonics." In addition, there are nanoparticles which up-convert two absorbed IR photons into a photon in the visible UV range; conversely, there are nanoparticles, called quantum cutters, that down-convert an absorbed vacuum UV photon to two photons in the visible range. A hot area of nanomaterials is photonic crystals, which consist of a periodic dielectric structure with a repeat unit of the order of wavelength of light. Nanocomposites also involve nanodomains of two or more dissimilar materials that are phase-separated on a nanometer size scale. Each nanodomain in the nanocomposite can impart a particular optical property to the bulk media. Flow of optical energy by energy transfer between different domains can also be controlled.

As could be noticed, integrating nanophotonics to the previous phosphors' technology is a convenient way to achieve a major number of enhanced properties. For that reason, nanophotonics also offers numerous opportunities for multidisciplinary research.

1.4. NANOSCALE ELECTRONIC INTERACTIONS

Confinement of electrons is the principal cause of nanoscale electronic interactions, which produce major modifications or new manifestations in the optical properties of a material. Figure 1.2 lists these interactions.

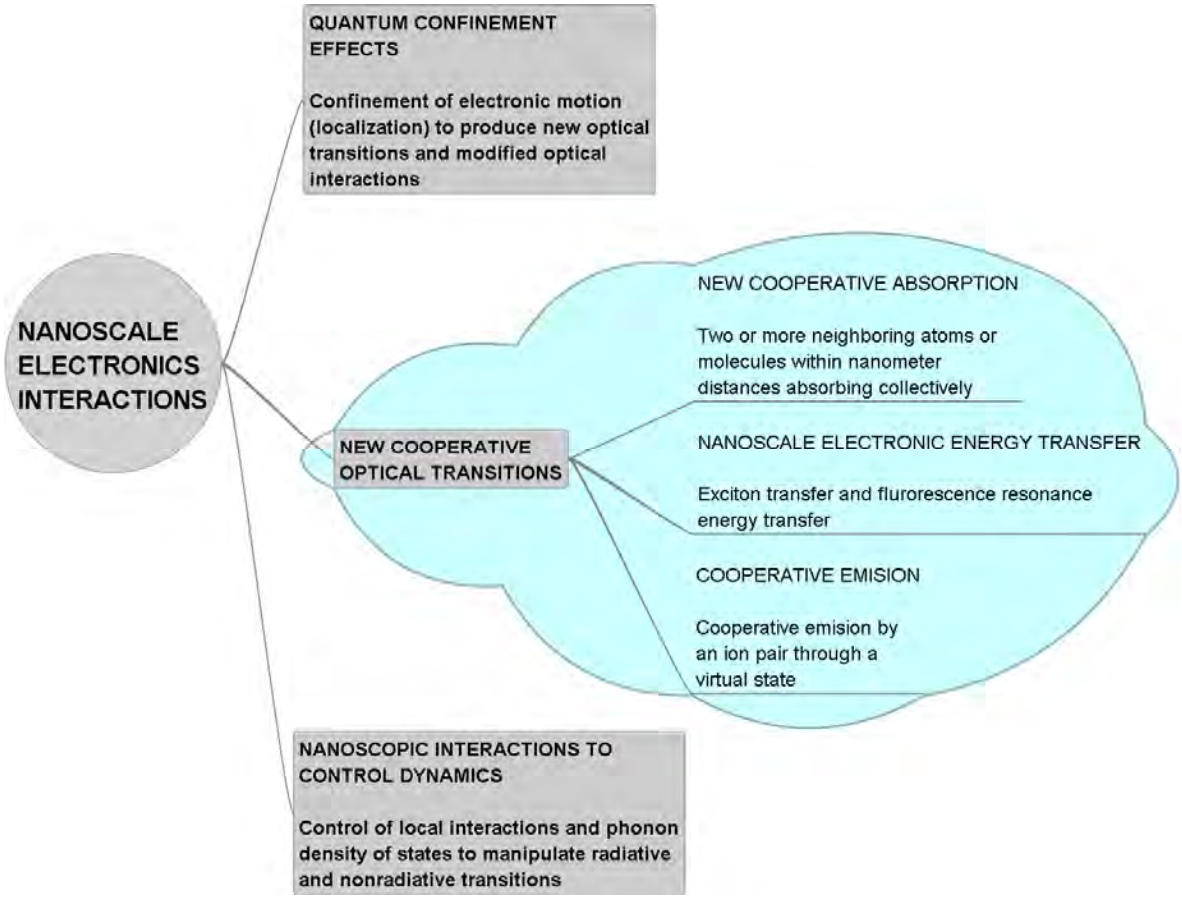

Figure 1.2: Nanoscale electronic interactions and its consequences in the optical properties of materials [4].

1.4.1. Quantum Confinement Effects

Quantum confinement produces a number of important manifestations in the electronic and optical properties of semiconductors. Manifestations that are important in relation to the optical properties are summarized in figure 1.3.

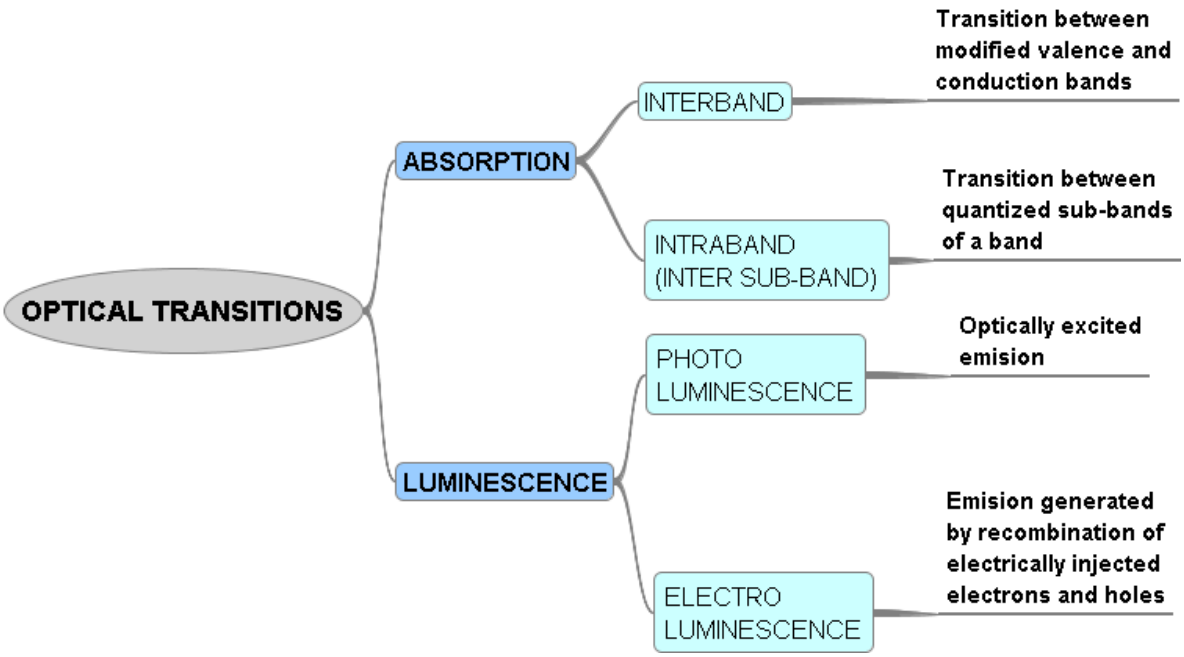

Figure 1.3: Quantum confinement effects [5].

Size Dependence of Optical Properties. Quantum confinement produces a blue shift in the bandgap as well as appearance of discrete sub-bands corresponding to quantization along the direction of confinement. As the dimensions of confinement increase, the bandgap decreases; hence the interband transitions shift to longer wavelengths, finally approaching the bulk value for a large width.

Increase of Oscillator Strength. Quantum confinement produces a major modification in the density of states both for valence and conduction bands. Instead of a continuous, smooth distribution of the density of states, the energy states are squeezed in a narrow energy range. This packing of energy states near the bandgap becomes more pronounced as the dimensions of confinement increase from quantum well, to quantum wire, to quantum dots. For quantum dots, the density of states has nonzero values only at discrete (quantized) energies. The oscillator strength of an optical transition for an interband transition depends on the joint density of states of the levels in the valence band and the levels in the conduction bands, between which the optical transition occurs. Furthermore, it also depends on the overlap of the envelope wave-functions of electrons and holes. Both these factors produce a large enhancement of oscillator strength upon quantum confinement. This effect is quite pronounced for quantum wires and quantum dots, which are more confined structures.

New Intraband Transitions. These transitions, corresponding to promotion of electrons from one level to another in the conduction band or hole from one level to another in the valence band, are also known as free carrier absorption in the bulk semiconductor. They depend on the presence of free carriers as a result of impurity doping (excess electrons or holes) or as a result of charge injection introduced by a bias field (photoinjection). In the

bulk, such transitions from one *k* level to another *k* level of the conduction band (or the valence band) require a change of quasi-momentum *k* and thus become allowed only by coupling with lattice phonons, which can provide or take up this momentum change. Thus, these processes are generally weak compared to interband transitions in the same bulk, because interband transitions do not require a change in *k*.

In quantum-confined structures such as a quantum well, there are sub-bands characterized by the different quantum numbers corresponding to quantization along the direction of confinement (growth). Thus for the conduction band, an electron can make a jump from one sublevel to another without changing its now two-dimensional quasi-momentum *k*. These intraband (or inter-sub-band) transitions still require the presence of a carrier in the conduction band (electrons) or in the valence band (holes).

Increased Exciton Binding. Quantum confinement of electrons and holes also leads to enhanced binding between them and thereby produces increased exciton binding energy compared to the exciton binding energy for the bulk sample.

A simple theoretical model (variational calculations) predicts that the Coulomb interactions between free electrons and holes in a two-dimensional system (quantum wells) are four times that in a three-dimensional system (bulk). However, the actual binding energy is somewhat smaller than the four times bulk value, because of the wave-function penetration into the barriers [6]. This binding produces excitonic states just below the bandgap, giving rise to sharp excitonic peaks at temperatures where the exciton binding energy is higher than the thermal energy. Thus, excitonic resonances are very pronounced in quantum-confined structures and, in the strong confinement conditions, can be seen even at room temperature

Increase of Transition Probability in Indirect Gap Semiconductor. The emission produced by the transition of an electron from the conduction band to the valence band is either extremely weak or nonexistent in the bulk form of an indirect gap semiconductor. An optical transition for an indirect bandgap semiconductor requires a change of quasi-momentum and thus involves the participation of phonons. However, in the quantum-confined structures, confinement of electrons produces a reduced uncertainty Δx in its position and, consequently, produces a larger uncertainty Δk in its quasi-momentum. Confinement, therefore, relaxes the quasi-momentum Δk selection rule, thus allowing enhanced emission to be observed in porous nanopartides. The area of luminescent nanoparticles is currently a great deal of activity.

1.4.2. Nanoscopic Interaction Dynamics

In the case of nanoscopic interactions, a particular radiative transition (emission at a particular wavelength) is enhanced by local interactions. Even in the case of insulating materials for which electronic wave-functions are localized within an atom, ion, or molecule, the immediate surrounding (within nanoscopic region) plays an important role in determining the fate of an electronic excited state. Thus a nanostructure control either by wisely choosing the nanoenvironment of the species to be excited or by utilizing a

nanoconfined structure (such as a nanoparticle) can be utilized to manipulate the excitation dynamics [7,8].

Examples are rare-earth ions and molecules for which the electronic wave-functions are fairly localized within the ion (or the molecule). In the case of rare-earth ions, important transitions are $f \rightarrow f$ and $f \rightarrow d$ involving the f and d orbitals of the rare-earth ions. The states in these ions split into levels by many electron and spin-orbit interactions. These levels are characterized by term symbols, represented as ${}^{2S+1}L_J$, where S is the total spin represented in its numerical value, L is the overall orbital angular momentum represented by a capital letter (S for $L = 0$, P for $L = 1$, etc.); the letter J in numerical value represents the overall angular momentum [9].

For simplicity we shall consider a system where an ion or a molecule is dispersed as a guest in a host matrix (or a nanoparticle). Thus, exciton interactions with nearest neighbor molecules are not considered. For this case of the localized electronic states, the following nanoscopic interactions play key roles in controlling the excitation dynamics:

Local Field Interactions. Even though the electronic wave-functions may be localized within the impurity (molecular or ionic), the electronic interactions may be different when the impurity is in ground or excited states. Thus, the excitation energy between the ground state of the impurity and its excited state is dependent on the nanoscopic environment, and the change in the energy gap can be manipulated by changing the nanoscopic environment. A clear example is what is called crystal field effect (or ligand field effect) for transition metal and rare-earth ions, where the symmetry (number and geometric arrangement of nearest neighbor host centers) surrounding the impurity center leads to a splitting of the *d* orbitals and thus shifting of the various energy levels. This has a profound effect on the excitation dynamics.

Electron-Phonon Coupling. Phonons are the vibrations of the lattice and, in the bulk, are ascribed into two types:

> *Low-Frequency Acoustic Phonons*. These phonons form a band described by the dispersion of their frequency, ω, as a function of the wavevector. Their dispersion (ω_k versus k) and density of states are described by the Debye model, in which at low frequencies the dispersion is linear and the slope is the speed of sound. This band spans from $\omega_k = 0$ at $k = 0$.
>
> *Optical Phonons*. These are high-frequency phonons and have a nonzero value of ω at $k = 0$.

The electron-phonon interaction is produced by the variation of the electronic interaction during lattice vibration of a given phonon mode (displacement's pattern). In other words, all phonon modes may not have the same amplitude at the impurity site. For example, certain optical modes may have very large amplitudes at the impurity site and very little at the host site. These modes are called *localized phonons* [10,11].

Electron-phonon interactions play an important role in determining two types of processes in electronic excitation; these are the *Dephasing of Electronic Transition* and *Relaxation of the Excited State.*

In the *Dephasing of Electronic Transition*, the electron-phonon interactions cause fluctuation of the electronic excitation energy and thus cause line broadening that is temperature dependent. This is called *homogeneous line broadening*. Often, the electronic transitions are inhomogeneously broadened due to the variation of interaction from one site to another.

For the *Relaxation of the Excited State*, the population of the excited state decreases by radiative or nonradiative transition from the excited state to a lower electronic state. The energy difference between the two electronic states is converted into phonon energy by creation of phonons due to electron-phonon interaction. This process of population relaxation is characterized by a population relaxation time *T* which also contributes to line broadening due to the Heisenberg uncertainty principle $\left(\Delta\nu \cdot T \approx \hbar\right)$. This broadening is called *lifetime broadening*.

In the case of the excess energy in nonradiative relaxation of electronic level 2 to electronic level 1 being dissipated by creating phonons, the process is known as a *direct process*. If it is accomplished by creation of only one phonon, it is called a *one-phonon process*. If many phonons are needed to make up for the energy difference between levels 2 and 1, the relaxation is designated as *multiphonon process* [12].

Another type of process is a Raman process in which a specific phonon mode interacts with the electronic excitation to accept the excess energy and create another phonon mode of higher frequency (for anti-Stokes Raman process). This type of process requires existing population of phonons and exhibits strong temperature dependence.

Nanostructure manipulation can be used to modify electron-phonon interaction. First, the phonon spectra and the phonon density of states can be modified by simply the selection of the host lattice that has a strong influence on the multi phonon relaxation process. Second, the electron-phonon coupling can also be influenced by the amplitude of the highest-frequency phonon of the host lattice at the impurity site or coupling of the localized phonons of the impurity with the phonons of the host.

Finally, the phonon spectrum of the host lattice is strongly influenced by reducing the size of the host from the bulk to a nanocrystal size. Important modification is in the acoustic phonon range where there is an appearance of a low-frequency gap and the formation of discrete vibrational states. Another modification of the phonon spectrum is the introduction of surface phonon modes that are localized at the interface of the nanoparticle and the surrounding medium. The surface phonon mode is strongly influenced by the dielectric constant of the surrounding medium and can introduce new channels of surface-induced nonradiative relaxations.

Impurity Pair Interactions (e.g., Ion-Ion Interactions). These interactions introduce new channels of excitation dynamics. The more common are the: (i) energy up-conversion where absorption of two photons produce emission of a photon of higher energy and (ii) energy down-conversion, also called quantum cutting, in which the absorption of a high-energy photon produces emission of two photons of lower frequencies. An important type of relaxation in both of these processes is cross-relaxation whereby an ion transfers part of its excitation energy to another ion. These ion-pair interactions show strong dependence on the ion-pair distance and thus on the nanostructure.

Nanoscale electronic interactions also produce new types of optical transitions and enhanced optical communications between two electronic centers. These are brief explained in next section.

1.4.3. New Cooperative Transitions

In a collection of ions, atoms, or molecules, two neighboring species can interact to produce new optical absorption bands or allow new multiphoton absorption processes. Example of that is the formation of biexcitons in a semiconductor or in a quantum-confined structure. This produces new optical absorption and emission from a biexcitonic state, whose energy is lower than that of two separate excitons. This difference in energy corresponds to the binding energy of the two excitons.

Another type of nanoscale electronic interaction giving rise to new optical transitions manifests when an electron-donating group (or molecule) is in the nearest neighboring proximity within nanoscopic distance of an electron withdrawing group or molecule (electron acceptor). The examples are organometallic structures involving a binding between an inorganic (metallic) ion and many organic groups (ligands). These types of structures produce novel optical transitions involving metal-to-ligand charge transfer or in some cases the reverse charge transfer induced by light absorption [13].

Yet another type of cooperative transition is provided by dimer formation between a species A in the excited electronic state (often labeled as A *) and another species B in the ground electronic state [13]. If A and B are the same, the resulting excited-state dimer is called an excimer. If A and B are different, the resulting heterodimer is called an exciplex. They both are still neutral species in the exciplex state, but bound together by favorable nanoscopic interactions. The excimer and exciplex emission is a very sensitive probe to the nanoscopic structure and orientation surrounding a molecule and has been extensively used to probe local environment and dynamical processes in biology.

Still another example of cooperative transition is shown by rare-earth ion pairs where one ion absorbs energy and transfers it to another ion, which then absorbs another photon to climb to yet another higher electronic level. The emission can then be up-converted in higher energy compared to the excitation. The excess electronic energy supplied by an optical transition (or by a chemical reaction as in a chemical laser) can be transferred from one center (ion, atom, or molecule) to another, often on nanoscopic scale, although long-range energy transfer can also be achieved. This electronic energy transfer

involves transfer of excess energy and not the transfer of electrons. Hence, in this process, one center has the excess energy (excited electronic state) and acts as an energy donor which transfers the excitation to an energy acceptor. Consequently the excited electron in the energy donor returns to the ground state while an electron in the energy acceptor group is promoted to an excited state. The interaction among energetically equivalent centers produces exciton migration either coherently (through many closely spaced levels forming an exciton band) or incoherently by hopping of an electron-hole pair from one center to another.

Another type of energy transfer is between two different types of molecules, a process often called fluorescence resonance energy transfer (FRET). This type of transfer, often used with two fluorescent centers within nanometers apart, is detected as fluorescence from the energy acceptor when the energy donor molecule is optically excited to a higher electronic level. FRET is a popular method in bioimaging to probe nanoscale interactions among cellular components, such as to monitor protein-protein interactions [13]. To maximize the FRET process, there should be a significant spectral overlap between the emission spectrum of the donor and the absorption spectrum of the acceptor.

Cooperative emission is another example of manifestation of electronic interactions. Here two neighboring centers within nanoscopic distances, when electronically excited, can emit a photon of higher energy through a virtual state of the pair centers. This process is exhibited by rare-earth ions and produces up-converted emission of a higher energy photon than the energy of excitation of individual ions. The interaction is again manifested when the two neighboring ions are separated within nanometers. The interaction between the two ions may be of multipole-multipole or electron exchange type, depending on the nature of electronic excitation in individual ions. It should be pointed out that the emission is not from a real level of the ion pair, but from a virtual level, which is not an allowed electronic level either of the individual ion or of the ion pair [3].

To achieve the effects produced by nanoscopic interactions dynamics, it is necessary to consider the use of a determined nanostructure. During the development of the work described in this thesis, it has been making use of rare-earth doped nanostructures in order to enhance a particular radiative transition.

1.4.4. Rare-Earth Doped Nanostructures

An example of a nanostructure that provides a control of excited-state dynamics to enhance a specific radiative process is the rare-earth doped nanoparticles. These nanoparticles do not show quantum confinement effects; nevertheless they are used in many different applications.

Rare-earth ion doped glasses have been used for applications such as optical amplification [14], lasing [15], optical data storage [16], and chemical sensing [17]. Most of the rare-earth ions used are in the 3+ oxidation state (with an effective charge of +3). In such a case, the lowest-energy electronic transitions are $4f \rightarrow 4f$ involving the inner *f*-atomic orbitals [9]. These transitions are very narrow and exhibit multiple structures

derived from electronic interactions, as well as spin-orbit coupling. In fact, great number of ions emit from a number of excited energy levels, thus exhibiting multiple radiative channels. Under controlled conditions, 2+ oxidation states can be produced for some rare-earth ions such as Eu and Sm, where the extra electron occupies the 5*d* orbital and can provide a $5d \rightarrow 4f$ transition. This transition is dipole allowed and approximately 10^6 times more intense than the $f \rightarrow f$ transition of the corresponding trivalent ion. Furthermore, the $d \rightarrow f$ transition is considerably blue-shifted (shorter wavelength) and broad, similar to what is observed for organic molecules. Both $f \rightarrow f$ and $d \rightarrow f$ transitions involve electrons that are localized in atomic orbitals of the ions.

A nanostructure control of the environment surrounding a rare-earth ion has important manifestations influencing the optical properties, such as:

Control of Local Interaction Dynamics. The efficiency of emission from a specific excited energy level is determined by the amount of competing nonradiative decay due to coupling with phonon modes (lattice vibrations) of the surrounding dielectric host. Qualitatively, the larger the number of phonons needed to convert the excitation energy into phonon energy, the lower is the efficiency of the nonradiative process. Hence, to enhance the emission efficiency by reducing nonradiative rate it is desirable to have the rare-earth ion incorporated into a dielectric host of very low frequency phonons. ZrO_2 and Y_2O_3 are examples of such hosts with their highest phonon frequencies of 470 cm^{-1} and 300-380 cm^{-1}, respectively, compared to Al_2O_3 (870 cm^{-1}) and SiO_2 (1100 cm^{-1}) [18]. They thus provide much improved emission efficiency. Because these media are crystalline, one can use nanocrystals of Y_2O_3 and ZrO_2 containing rare-earth ions to provide low-frequency phonon media and then disperse these nanocrystals in SiO_2 or other glass bulk media that can easily be produced in the form of a film, a fiber, or a channel waveguide.

Control of Oxidation State. The manipulation of local environment can produce stabilization of the 2+ oxidation state for a rare-earth ion. An example is the europium ion, which generally forms a 3+ oxidation state. It has shown that by co-doping with Al and sintering above 1000°C, a spontaneous reduction of Eu3+ ion occurs to produce Eu^{2+} [19] whereby the sharp and narrow emissions in the range of ~600 nm (red) from the Eu^{3+} ions are replaced by a broad emission band of Eu^{2+} at ~440 nm (blue).

Generation of New Up-Conversion Processes. Rare-earth ions also exhibit a number of up-conversion processes whereby an IR excitation produces an up-converted emission from a higher level [20]. Many new channels of up-conversion involve interaction with another ion within a nanoscopic domain (i.e., ion-pair interactions). Thus, nanostructure design can be used to enhance these processes.

Generation of Quantum Cutting Processes. Quantum cutting refers to an optical down-conversion process in which the energy of an absorbed photon is split to produce emission of two photons of lower energies [21]. In the case of rare-earth ions, the absorption of vacuum UV photons has been shown to produce emission of two-photons in the visible, which is of considerable interest for producing mercury-free fluorescent tubes and plasma display panels. It was also demonstrated that quantum cutting can be observed in infrared

by the absorption of visible photons [22]. Nanostructure control can be utilized to produce quantum cutting by energy transfer between two different ions or from host to active ion. The efficiency of these two-photon down-conversion processes have been reported to be as high as 200% [23].

Modification of Phonon Spectrum. Even though the electronic spectra of rare-earth ions show no quantum confinement effect, the phonon spectrum of the lattice shows important manifestations when change in going from bulk to nanocrystal environment as previously discussed. In the acoustic-phonon spectrum a gap appears with the formation of discrete vibrational states [24]. This modification of the phonon spectrum produces important manifestations in the electron-phonon interaction and therefore multiphonon relaxations and phonon-induced line broadening of electronic transitions. Thus, for the $^7F_0 \rightarrow {}^5D_0$ transition of Eu^{3+} ions in Eu_2O_3 a different temperature dependence ($\sim T^3$) is found for the line width in nanoparticles compared to $\sim T^7$ dependence in the bulk form. As an example, the decay rates from the upper levels of the $^5D_1$ manifold by a one-phonon process are dramatically reduced by up to two orders of magnitude compared to those observed in micron-sized materials [25].

Size Dependence of Emission Bands. The size dependence of the electron-phonon coupling, derived from the change in the phonon spectrum, together with a change in the crystal field strength can produce a shift of the emission peak which is not due to quantum confinement of electrons. For the ZnS nanoparticles containing Eu^{2+} ions, a size dependence of the emission peak involving the $4d \rightarrow 4f$ transition in Eu^{2+} has been observed [26]. The emission bands of the 4.2, 3.2, and 2.6 nm-size ZnS:Eu^{2+} nanoparticles result from decreases in both the electron-phonon coupling and the crystal field strength with the decreasing particle size. Variation of the charge-transfer band intensity was demonstrated in Eu^{3+} doped Lu_2O_3 nanocrystallites to be dependent on size of nanoparticles [27].

An example of the application of nanostructure control to enhance a particular optical transition is provided by the Er^{3+} ions. Erbium-doped fiber amplifiers (EDFA) are utilized as very efficient optical amplifiers widely used for telecommunications at 1.55 μm. One can manipulate, by nanostructure control, the excited-state dynamics to produce emission from a given level (thus emission of a specific color). Consequently, one can derive different types of emission from the same ion. The 1.5 μm emission from erbium used for amplification is produced by pumping at 980 nm with co-pumping at 1400 nm to enhance the efficiency. The lifetime of this transition in commercially sold optical amplifiers is typically of the order of 8 ms. Nanostructure control by using a multicomponent environment to manipulate the local interactions around the erbium ion has produced nanoparticles with a much longer lifetime of up to 17 ms [28]. This increased lifetime allows more efficient amplification because as the nonradiative process is reduced an increased lifetime approaching to the theoretical limit of radiative lifetime can be realized. This will ensure that all absorbed photons are used to produce emission (used for the radiative process).

The second factor that has to be considered to enhance EDFA is the number density of the emitter. The number density of erbium ions should be as high as possible without inducing "concentration quenching" which occurs when two ions communicating with each other produce nonradiative dissipation of excited state energy. Therefore, it is important to ensure that no ion clustering takes place at higher concentration. By nanostructure control, one can also increase the number density without concentration quenching caused by ion clustering. Hence, a nanostructure-controlled nanoparticle technology can produce efficient optical amplification.

The effects that bring forth the generation of new up-conversion processes are desirable for developing and enhancing systems based on the up-conversion phenomena. Hence, the work described in this thesis is interested on rare-earth doped nanostructures for up-converting phosphors.

1.4.5. Up-Converting Nanophores

Part of the researches in nanometer control is related to producing efficient up-conversion. Some of the up-conversion processes that efficiently occur in a rare-earth or transition metal ion doped medium [20] are shown in figure 1.4. The most noticeable up-conversion processes in these ions involve absorption of two photons on distinct levels. Thus, these processes are different from the direct or simultaneous two-photon processes where the absorption of two photons occurs simultaneously without involving any real intermediate one-photon levels.

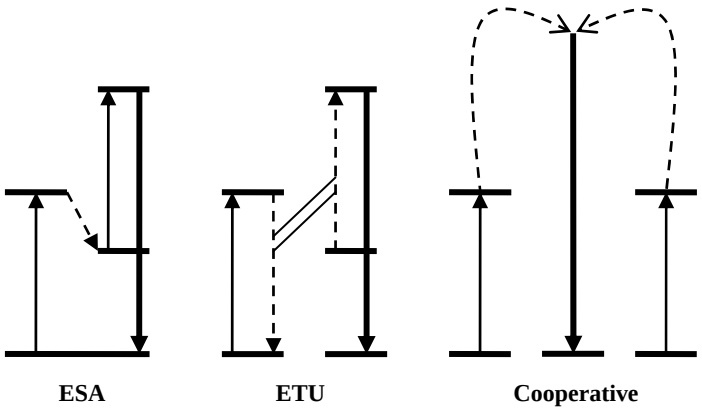

Figure 1.4: Types of up-conversion processes.

The up-conversion process in the rare-earth ions can be divided into two broad classes, as described in figure 1.5. The nanostructure's control, in the case of excited-state absorption (ESA), provides the ability to minimize nonradiative relaxation (loss of population) of the intermediate level generated by the first photon. For cooperative mechanism, the nanostructure design involves the control of distances between the ion pairs within nanoscopic region. Because the dominant electronic interactions between the two interacting ions are electric multipole or exchange type, both of them are strongly dependent on the ion-ion separation.

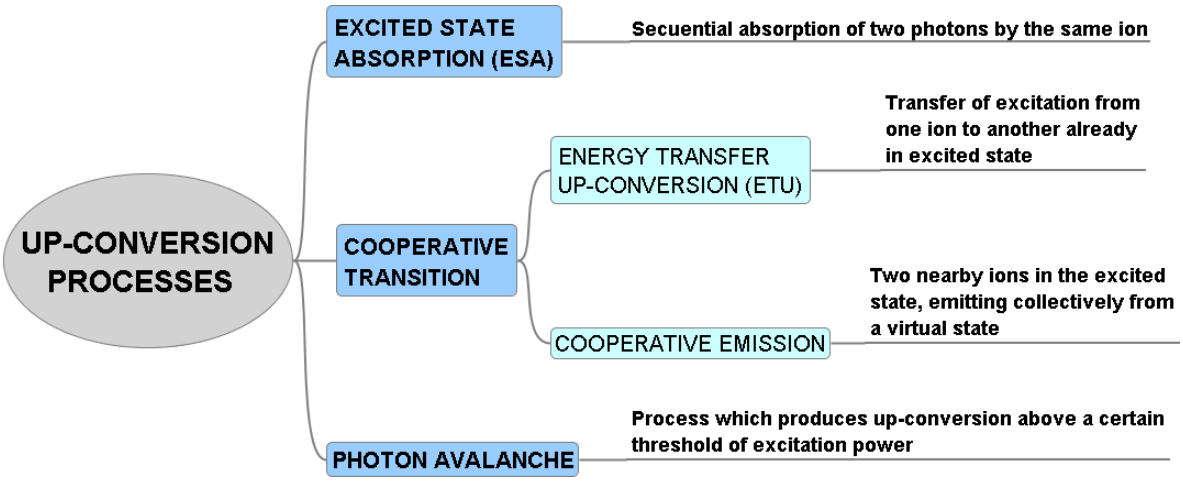

Figure 1.5: Up-conversion processes occurring in the rare-earth ions [29].

1.4.5.1. Excited-state absorption

The *excited state absorption* (ESA) process is essentially a single ion mechanism and thus it occurs in materials with relatively weak doping levels. It is a two photon process in which an incoming photon from the pump beam will bring the ion to an intermediate excited state and a second will proceed to bring the ion to the upper emitting level [30]. The upconverted luminescence intensity in this process usually varies quadratically with the pump beam but varies linearly with the concentration of the rare-earth dopant [31].

1.4.5.2. Cooperative transition

One cooperative transition is the *energy transfer up-conversion* (ETU). In this process two ions in close proximity are involved, which are excited by the pump beam to an intermediate level. The two ions are coupled by a nonradiative process in which one relaxes to a lower lying state, while the other ion is promoted to the upper emitting level [32]. In other words, a ion which has already undergone GSA and consequently is promoted to its intermediate excited state, transfers its energy non-radiatively to a neighboring ion, also in the intermediate state, thus promoting that ion to the upper emitting level while the prior ion returns to the ground state. ETU differs from ESA process in that the upconversion luminescence also varies cuadratically with the dopant concentration [30].

The other cooperative transition is the *cooperative emission*, in which two neighboring ions in the excited state are separated within nanometers and when the two nearby ions are electronically excited can emit a photon of higher energy through a virtual state of the ion pair. The cooperative emission is emitting collectively from a virtual state which is not an allowed electronic level either of the individual ion or of the ion pair. Analyzing the upconverted luminescence signal intensity (I_{UPC}) as function of the pumping

intensity (I_{PUMP}), it follows the equation $I_{UPC} = k \cdot I^{n}_{PUMP}$ where n has the value of two when the cooperative emission is present; and it is necessary to consider that energy of this luminescence must be multiple of two of the energy pump.

1.4.5.3. Photon Avalanche

The *photon avalanche* is an up-conversion process which produces up-conversion above a certain threshold of excitation power [33]. Below this threshold, very little up-converted fluorescence is produced and the medium is transparent to the pump beam (in the IR for the rare-earth ions). Above the pump threshold, the pump beam is strongly absorbed and the fluorescence intensity increases by orders of magnitude.

The mechanism of photon avalanche is illustrated by the energy diagrams of figure 1.6. In this process the pump beam does not have sufficient energy to directly populate level 2 by ground-state absorption (GSA). However, there is strong excited-state absorption (ESA) from level 2 to level 3 at the pump wavelength. Thus, if somehow the metastable (intermediate) level 2 becomes populated, it readily absorbs the pump photon to level 3, which produces an up-converted emission.

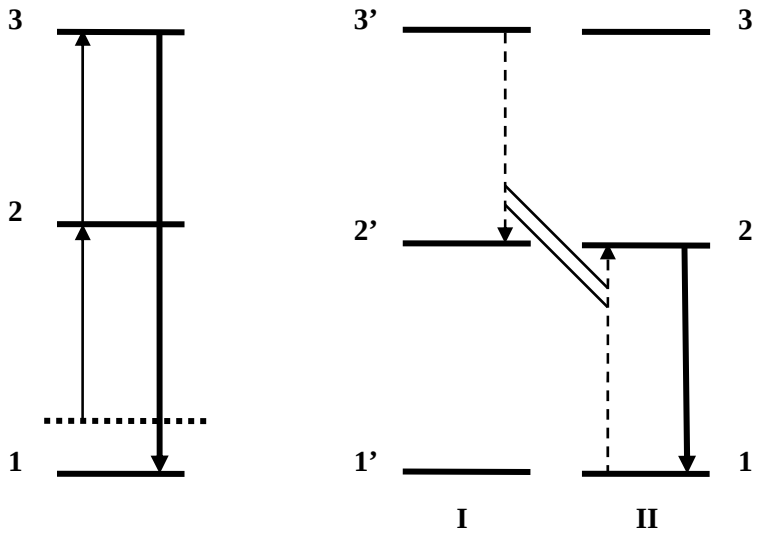

Figure 1.6: Mechanisms of population of the intermediate level in photon avalanche up-conversion.

The population of level 2 is created by two mechanisms. Initially, population of level 2 is created by weak excitation from level 1 involving assistance of phonons. In the diagram it is shown as originating from a phonon state (dotted line) or it could be through the phonon side band. As soon as level 2 is populated, it readily absorbs another photon

from the pump beam due to strong excited-state absorption and reaches level 3. In some ions, level 3 can then produce an up-converted emission. Some excited ions transfer part of its energy from level 3 to another ion by a nonradiative energy transfer mechanism, called cross-relaxation (abbreviated as CR), which results in both ions being in level 2. This cross-relaxation process is represented in the figure by the dashed line. Now both ions are in state 2 as a result of photon absorption and subsequent energy transfer. Under the right pumping conditions two ions can produce four in the intermediate level, four can produce eight, etc., from where they readily populate level 3 to further initiate cross-relaxation and more ESA to increase level 3 population resulting in a dramatic increase of fluorescence as an avalanche process. The strong pump power dependence comes from the strong dependence of CR on the population of level 3, and hence on the pump power. Graphing the upconverted luminescence logarithmic dependence with the pump beam, the PA process implies the appearance of an inflection point in the graph, related to the threshold level of the pump intensity [30].

The requirement for photon avalanche can thus be summarized as follows:

- The excitation energy must not be in resonance with any ground-state absorption but between an intermediate metastable level and the upper emitting state.
- Excited-state absorption must be strong.
- Rare-earth ion concentration should be high enough for ion-ion interactions to produce efficient cross-relaxation populating the intermediate state.

Nanoscale manipulation has two advantages. First, the initial population of level 1 through phonon interactions can be wisely controlled by optimizing the phonon density of states and electron-phonon coupling. Second, the ion-ion interaction to produce efficient cross-relaxation can also be optimized by a nanostructure control.

1.4.5.4. Advantages of Rare-Earth Up-Converting Nanophores

The advantages offered by these types of up-conversion processes are that they can be induced even by a low-power laser. In contrast, a simultaneous two-photon process requires a high intensity pulse laser source.

The nanoparticles containing the up-converting rare-earth ions can be called up-converting nanophores. Their advantage is that they can be dispersed in a glass or plastic medium for display. They can also be surface functionalized to be dispersable in an aqueous medium for bioimaging. For these purposes, a major challenge has been to produce small nanophores in the desired size range of < 50 nm at the same time providing highly efficient up-conversion. To achieve this goal it has been used low-frequency phonon host nanocrystals such as ZrO_2 and Y_2O_3. It was observed that the up-conversion luminescence intensity depends on the crystal structure and particle size [34].

The asymmetric structure of the low-symmetry site of the rare-earth ions allows intermixing of the *f* states with higher electronic configuration and as a result the optical transition probabilities increases. The up-conversion luminance value for same

concentration of Er^{3+} ions in $BaTiO_3$ is much higher than that in the TiO_2 host [35] because this oxide matrix has low phonon energy that reduces the probability of multiphonon nonradiative process. The presence of a large energy gap between the emitting and the terminal levels also reduces the nonradiative decay. This reduction leads to an increase in the emission efficiency.

The efficiency of these materials is dependent on the excited-state dynamics of the rare-earth ions and their interactions with the host matrix. This interaction can be a function of the host phase and the dopant concentration. The excited-state dynamics is also dependent on the energy migration between the active ions, the statistical distribution of the active ions, and the site symmetry of the active ions in the host matrix.

If one disperses these up-converting nanoparticles in a homogeneous medium, like glass or in some way proper for bioimaging in a solution, they should be transparent. These bulk media should not scatter light because the nanoparticles are ≤ 35 nm and yet they are very efficient up-converters. One can also disperse the nanoparticles in a charge-transporting medium to generate electro luminescence, which means a recombination of electron-hole pairs at a nanoparticle in a plastic matrix. This combination can provide the features of luminescence characteristic like inorganics, but in a flexible physical form of a plastic matrix.

REFERENCES AND NOTES

[1] Shigeo Shionoya, chapter one of *Phosphor Handbook*, CRC Press, 1999

[2] Based on table 1 appeared in section 1.3 of [1]

[3] Paras N. Prasad, *Nanophotonics*, John Wiley & Sons, Inc., 2004

[4] Based on table 2.3 of [3]

[5] Based on table 4.2 of [3]

[6] McCombe, B. D.; Petrou, A., Optical Properties of Semiconductor Quantum Wells and Superlattices, in *Handbook of Semiconductors*, Vol. 2, *Optical Properties*, M. Balkanski, ed., Elseiver Science Publishers, Amsterdam, 1994, Chapter 6, pp. 285-384

[7] Some further reading references are: [8], and Jüstel et al., *New Developments in the Field of Luminescent Materials for Lighting and Displays.* Angew. Chem. Int. Ed. **37**, 3084-3103 (1998)

[8] Gamelin, D. R., and Güdel, H. V. *Upconversion Processes in Transition Metal and Rare Earth Metal Systems*. Top. Cur. Chem. **214**, 1-56 (2001)

[9] Dieke, G.-H., *Spectra and Energy Levels of Rare Earth Ions in Crystals*, Interscience, New York, 1968

[10] For details of phonon modes in a crystal lattice, is suggested the book by Kittel, C., *Introduction to Solid State Physics*, 7th edition, John Wiley & Sons, New York, 2003

[11] For phonons and phonon interactions in molecular solids, check the review made by Hochstrasser, R. M., and Prasad, P. N. *Optical Spectra and Relaxation in Molecular Solids*, in Excited States, Vol. 1, E. C.-Lin, ed. Academic Press, New York, 1974, pp. 79-128

[12] Multiphonon relaxation process is often described by using the theory developed by Huang and Rys (1950) in which the multiphoton relaxation is induced by a single-phonon mode. For a detailed description of this process and the expression for the nonradiative rate, a good reference is Yeh et al. *Multiphonon Relaxation and Infrared-to-Visible Convertion of Er^{3+} and Yb^{3+} Ions in Barium-Thorium Fluoride Glass*. J. Appl. Phys. **62**, 266-275 (1987)

[13] Prasad, P. N., *Introduction to Biophotonics*, John Wiley & Sons, New York, 2003

[14] Digonnet, M. J. F., ed., *Rare Earth Doped Fiber Laser and Amplifiers*, Marcel Dekker, New York, 1993

[15] Weber, M. J. *Science and Technology of Laser Glass*. J. Non-Cryst. Solid. **123**, 208-222 (1990)

[16] Nogami et al. *Room Temperature Persistent Spectra Hole Burning in Sm^{2+}-Doped Silicate Glasses Prepared by Sol-Gel Process*. Appl. Phys. Lett. **66**, 2952-2954 (1995)

[17] Samuel et al. *Miniaturization of Organically Doped Sol-Gel Materials: A Micron-Size Fluorescent pH Sensor*. Matter. Lett. **21**, 431-434 (1994)

[18] Patra, A.; Friend, C. S.; Kapoor, R., and Prasad, P. N. *Upconversion in Er^{3+}:ZrO_2 Nanocrystals*. J. Phys. Chem. B **106**, 1909-1912 (2002)

[19] Biswas, A.; Friend, C. S., and Prasad, P. N. *Spontaneous Reduction of Eu^{3+} Ion in Al Co-Doped Sol-Gel Silica Matrix During Densification*. Matter. Lett. **39**, 227-231 (1999)

[20] [8]; Scheps R. *Upconversion Laser Processes*. Prog. Quantum Electron. **20**, 271-358 (1996); de Araüjo et al. *Frequency Upconversion in Rare-Earth Doped Fluorinated Glasses*. C. R. Chim. **5**, 885-898 (2002)

[21] Wegh, R. T.; Donker, H.; Oskam, K. D., and Meijerink, A. *Visible Quantum Cutting in Eu^{3+}-Doped Gadolinium Fluorides via Down Conversion*. J. Lumin. **82**, 93-104 (1999a)

[22] Strek, W.; Deren, P., and Bednarkiewicz, A. *Cooperative Process in $KYb(WO_4)_2$ Crystal Doped with Eu^{3+} and Tb^{3+} Ions*. J. Lumin. **87-89**, 999-1001 (2000)

[23] Wegh, R. T.; Van Loef, E. V. D., and Meijerink, A. *Visible Quantum Cutting via Down Conversion in $LiGdF_4$:Er^{3+}, Tb^{3+} Upon Er^{3+} $4f^{11} \rightarrow 4f^{10}5d$ Excitation*. J. Lumin. **90**, 111-122 (2000)

[24] Meltzer, R. S., and Hong, K. S. *Electron-Phonon Interactions in Insulating Nanoparticles: Eu_2O_3.* Phys. Rev. B **61**, 3396-3403 (2000)

[25] Yang, H.-S.; Hong, K. S.; Feofilov, S. P.; Tissue, B. M.; Meltzer, R. S., and Dennis, W. M. *Electron-Phonon Interaction in Rare Earth Doped Nanocrystals*. J. Lumin. **83-84**, 139-145 (1999)

[26] Chen, W.; Malm, J.-O.; Zwiller, V.; Wallenberg, R., and Bovin, J.-O. *Size Dependence of Eu^{2+} Fluorescence in ZnS:Eu^{2+} Nanoparticles*. J. Appl. Phys. **89**, 2671-2675 (2001)

[27] Strek, W.; Zych, E., and Hreniak, D. *Size Effects on Optical Properties of Lu_2O_3:Eu_{3+} Nanocrystallites*. J. Alloys Comp. **344**, 332-336 (2002)

[28] Biswas, A.; Friend, C. S.; Kapoor, R., and Prasad, P. N. *Er^{3+}-Doped Multicomponent Sol-Gel processed Silica Glass for Optical Signal Amplification at 1.5 μm*. Appl. Phys. Lett. **82**, 2389-2391 (2003)

[29] Based on table 6.1 of [3]

[30] Vetrone, Fiorenzo, Boyer, J.C.; Capobianco, J. A.; Speghini, A.; Bettinelli, M. *Luminiscence Spectroscopy and Near-Infrared to Visible Upconversion of Nanocrystalline $Gd_3Ga_5O_{12}$: Er^{3+}*. J. Phys. Chem. B, **107**, 10747-10752 (2003)

[31] Vetrone, Fiorenzo, Boyer, J.C.; Capobianco, J. A.; Speghini, A.; Bettinelli, M., *J. Phys. Chem*. B, **106**, 5622-5628 (2002)

[32] Auzel, F. C. R., *Acad. Sci*. (Paris), **262**, 1016-1019 (1966)

[33] Joubert, M. F. *Photon Avalanche Upconversion in Rare-Earth Lasers Materials*. Opt. Matter. **11**, 181-203 (1999); [8]

[34] Patra, A.; Friend, C. S.; Kapoor, R., and Prasad, P. N. *Effect of Crystal Nature on Upconversion Luminescence in Er^{3+}:ZrO_2 nanocrystals*. Appl. Phys. Lett. **83**, 284-286 (2003a)

[35] Patra, A.; Friend, C. S.; Kapoor, R., and Prasad, P. N. *Fluorescence Upconversion Properties of Er^{3+}-Doped TiO_2 and $BaTiO_3$ Nanocrystallites*. Chem Mater. **15**, 3650-3655 (2003)

Chapter 2

Synthesis and Structural Characterization Methods

2.1. INTRODUCTION

In order to explore novel physical properties and realize potential applications of nanostructures and nanomaterials, the ability to fabricate and process nanomaterials and nanostructures is the first corner stone in nanotechnology. Nanostructured materials are those with at least one dimension belonging to nanometer scale, and include nanoparticles (also quantum dots), nanorods and nanowires, thin films, and bulk materials made of nanoscale building blocks or consisting of naoscale structures. Many technologies have been explored to fabricate nanostructures and nanomaterials. These technical approaches can be grouped in several ways. One way is to group them according to the group of media, for example:

- Vapor phase growth, including laser reaction pyrolysis for nanoparticle synthesis and atomic layer deposition (ALD) for thin film deposition.
- Liquid phase growth, including colloidal processing for the formation of nanoparticles and self assembly of monolayers.
- Solid phase formation, including phase segregation to make metallic particles in glass matrix and two-photon induced polymerization for the fabrication of three-dimensional photonic crystals.
- Hybrid growth, including vapour-liquid-solid (VLS) growth of nanowires.

Another way is to group the techniques according to the form of products, which it can be as follows:

- Nanoparticles by means of colloidal processing, flame combustion and phase segregation.
- Nanorods or nanowires by template-based electroplating, solution-liquid-solid growth (SLS), and spontaneous anisotropic growth.
- Thin films by molecular beam epitaxy (MBE) and atomic layer deposition (ALD).
- Nanostructured bulk materials, for example, photonic bandgap crystals by self-assembly of nanosized particles.

Applying the criteria considered by this group, the figure 2.1 is presented, in order to give a better panorama about the principal techniques that are used to fabricate and process nanomaterials and nanostructures. With the scheme, one can infer the wide spectra of applied processes and techniques. The type of particles and the synthesis process performed and reported in this thesis work are also indicated in figure 2.2. In next section will be a brief description of the methods for zero-dimensional particles, especially on homogeneous nucleation.

Other way to group different fabrication and processing techniques are the top-down and bottom-up approaches. Attrition or milling is a typical top-down method in making nanoparticles, whereas the colloidal dispersion is a good example of bottom-up approach in the synthesis of nanoparticles. Lithography may be considered as a hybrid approach, since the growth of thin films is bottom-up whereas etching is top-down, while nanolithography and nanomanipulation are commonly a bottom-up approach.

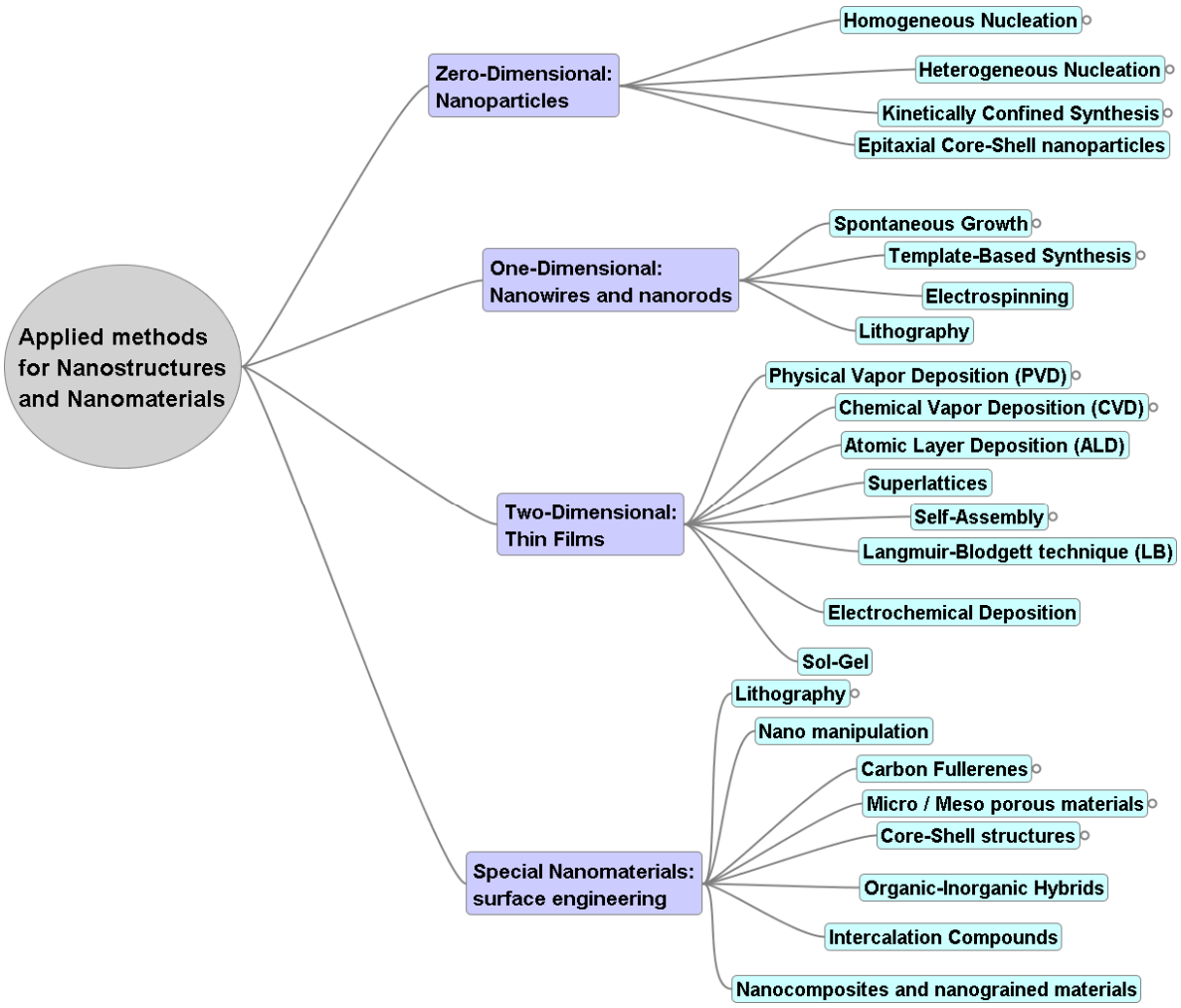

Figure 2.1: General applied methods for nanostructures and nanomaterials fabrication.

The biggest problem with top-down approach is the imperfection on the surface structure. Such imperfections would have a significant impact on physical properties and the surface chemistry since the surface over volume ratio in nanostructures and nanomaterials is very large.

Bottom-up approach refers to the build-up of a material from the bottom: atom by atom, molecule by molecule, or cluster by cluster. In that way, bottom-up approach promises a better chance to obtain nanostructures with less defects, more homogeneous chemical composition and better range ordering. This is because this approach is driven mainly by the reduction of Gibbs free energy, so that, produced nanostructures and nanomaterials are in a state closer to a thermodynamic equilibrium state. On the contrary, top-down approach most likely introduces internal stress, in addition to surface defects and contaminations [1].

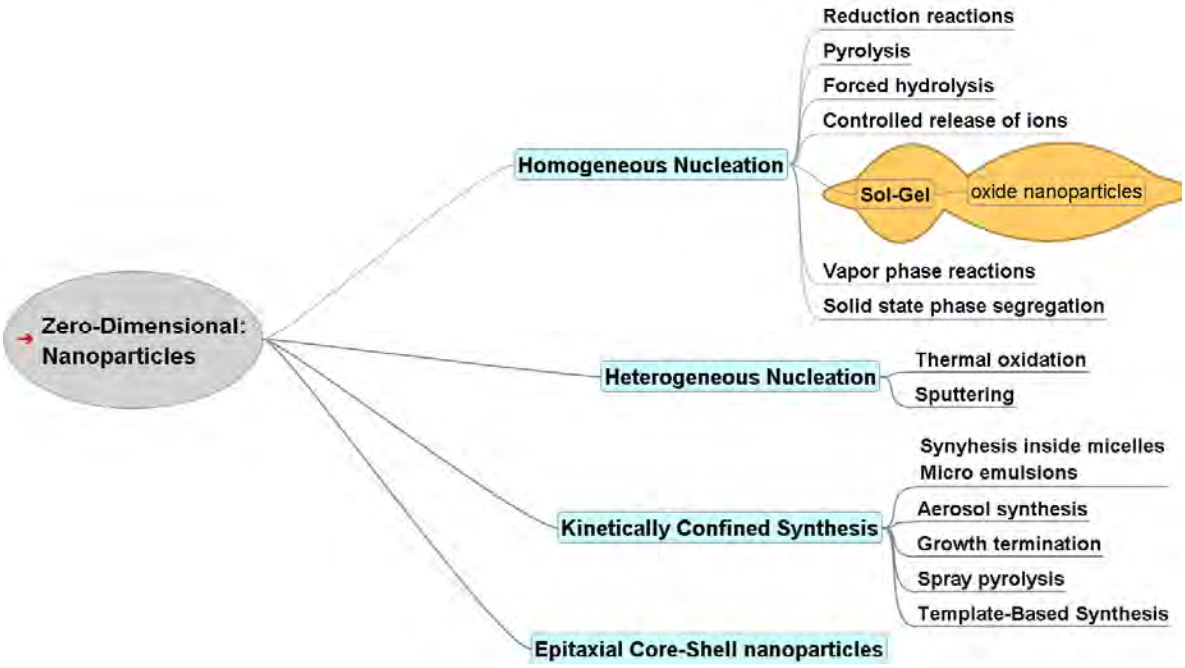

Figure 2.2: Methods applied for zero-dimensional particles fabrication.

2.2. BRIEF GLANCE AT ZERO-DIMENSIONAL NANOPARTICLES

Bottom-up approaches are far more popular in the synthesis of nanoparticles and many methods have been developed. For example, nanoparticles are synthesized by homogeneous nucleation from liquid or vapor, or by heterogeneous nucleation on substrates. Nanoparticles or quantum dots can also be prepared by phase segregation through annealing appropriately designed solid materials at elevated temperatures. Nanoparticles can be synthesized by confining chemical reactions, nucleation and growth processes in a small space such as micelles.

Various synthesis methods or techniques can be grouped into two categories: *thermodynamic equilibrium approach* and *kinetic approach*. In the *thermodynamic approach*, synthesis process consists of (i) generation of supersaturation, (ii) nucleation, and (iii) subsequent growth. In the *kinetic approach*, formation of nanoparticles is achieved by either limiting the amount of precursors available for the growth such as used in molecular beam epitaxy, or confining the process in a limited space such as aerosol synthesis or micelle synthesis [1].

For the fabrication of nanoparticles, a small size is not the only requirement. For any practical application, the processing conditions need to be controlled in such a way that resulting nanoparticles have the following characteristics: (i) identical size of all particles (also called mono sized or uniform size distribution), (ii) identical shape or morphology, (iii) identical chemical composition and crystalline structure, and (iv) individually

dispersed or monodispersed, i.e. no agglomeration. If agglomeration does occur, nanoparticles should be readily redispersible.

2.2.1. Homogeneous Nucleation

For the formation of nanoparticles by homogeneous nucleation, a supersaturation of growth species must be created. A reduction in temperature of an equilibrium mixture, such as a saturated solution would lead to supersaturation. Another method is to generate a supersaturation through *in situ* chemical reactions by converting highly soluble chemicals into less soluble chemicals. Nanoparticles can be synthesized through homogeneous nucleation in three mediums: liquid, gas and solid; however, the fundamentals of nucleation and subsequent growth processes are essentially the same.

2.2.1.1. Fundamentals of homogeneous nucleation

When the concentration of solute in a solvent exceeds its equilibrium solubility or the temperature decreases below the phase transformation point, a new phase appears. Consider the homogeneous nucleation of a solid phase from a supersaturated solution. In this case, the solution with solute exceeding the solubility (supersaturation) possesses a high Gibbs free energy, and the overall energy of the system would be reduced by segregating solute from the solution. This reduction of Gibbs free energy is the driving force for both nucleation and growth. The change of Gibbs free energy per unit volume of the solid phase, ΔG_v, is dependent on the concentration of the solute [1]:

$$\Delta G_V = -\frac{kT}{\Omega}\ln\left(C/C_O\right) = -\frac{kT}{\Omega}\ln\left(1+\sigma\right) \qquad (2.1)$$

where C is the concentration of the solute, C_0 is the equilibrium concentration or solubility, k is the Boltzmann constant, T is the temperature, Ω is the atomic volume, and σ is the supersaturation defined by $(C\text{-}C_0)/C_0$.

Without supersaturation ΔG_v is zero, and no nucleation would occur. When $C > C_0$, ΔG_v is negative and nucleation occurs spontaneously. However, this energy reduction is counter balanced by the introduction of surface energy, accompanied with the formation of a new phase and thus in an increase in the surface energy $\Delta\mu_s$ of the system. The newly formed nucleus is stable only when its radius exceeds a critical size, r^*. A nucleus smaller than r^* will dissolve into the solution to reduce the overall free energy, whereas a nucleus larger than r^* is stable and continues to grow.

In the synthesis and preparation of nanoparticles or quantum dots by nucleation from supersaturated solution or vapour, the critical size represents the limit on how small nanoparticles can be synthesized. To reduce the critical size and free energy, one needs to increase the change of Gibbs free energy, ΔG_v, and reduce the surface energy of the new phase. Equation (2.1) indicates that ΔG_v can be significantly increased by increasing the supersaturation σ, for a given system. Temperature can also influence surface energy. Surface energy of the solid nucleus can change more significantly near the roughness

temperature. Other possibilities include: (i) use of different solvent, (ii) additives in solution, and (iii) incorporation of impurities into solid phase, when other requirements are not compromised.

The nucleation occurs only when the supersaturation reaches a certain value above the solubility, which corresponds to the energy barrier for the formation of nuclei. Initially there will be no nucleation until the concentration of the growth species increases and reaches the minimum saturation required to overcome the critical energy barrier, then the nucleation rate increases very rapidly in like manner to concentration. After the initial nucleation, the concentration or supersaturation of the growth species decreases and the change of Gibbs free energy reduces. When the concentration decreases below a specific concentration which corresponds to the critical energy, no more nuclei would form, whereas the growth will proceed until the concentration of growth species has attained the equilibrium concentration or solubility [1]. Although growth process cannot proceed when there is no nucleus, growth rate is above zero for a concentration above its equilibrium solubility. Once nuclei are formed, growth occurs simultaneously. Above the minimum concentration nucleation and growth are inseparable processes; however, these two processes proceed at different speeds.

For the synthesis of nanoparticles with uniform size distribution, it is best if all nuclei are formed at the same time. In this case, all the nuclei are likely to have the same or similar size, since they are formed under the same conditions. In addition, all the nuclei will have the same subsequent growth and in consequence, mono sized nanoparticles can be obtained. It is obvious that it is highly desirable to have nucleation in a very short period of time. In practice, to achieve a sharp nucleation, the concentration of the growth species most be increased abruptly to a very high supersaturation and then quickly brought below the minimum concentration for nucleation. Below this concentration, no more new nucleus forms, whereas the existing nuclei continue to grow until the concentration of the growth species reduces to the equilibrium concentration. The size distribution of nanoparticles can be further altered increasing or decreasing depending on the kinetics of the subsequent growth process. The formation of uniformly sized nanoparticles can be achieved if the growth process is appropriately controlled.

2.2.1.2. Subsequent growth of nuclei

The growth process of the nuclei involves multiple steps and the main steps are: (i) generation of growth species, (ii) diffusion of the growth species from bulk to the growth surface, (iii) adsorption of the growth species onto the growth surface and (iv) surface growth through irreversible incorporation of growth species onto the solid surface. These steps can be further grouped into two processes. Supplying the growth species to the growth surface is termed as *diffusion*, which includes the generation, diffusion and adsorption of growth species onto the growth surface whereas incorporation of growth species adsorbed on the growth surface into solid structure is denoted as *growth*. A diffusion-limited growth would result in a different size distribution of nanoparticles as compared with that by growth-limited process.

2.2.1.2.1. *Growth controlled by diffusion*

When the concentration of growth species reduces below the minimum concentration for nucleation, nucleation stops, whereas the growth continues. If the growth process is controlled by the diffusion of growth species from the bulk solution to the particle surface, the growth rate is given by [2]:

$$dr/dt = D\left(C - C_S\right)\frac{V_m}{r} \tag{2.2}$$

where r is the radius of spherical nucleus, D is the diffusion coefficient of the growth species, C is the bulk concentration, C_s is the concentration on the surface of solid particles, and V_m is the molar volume of the nuclei. By solving this differential equation and assuming the initial size of nucleus r_0 and the change of bulk concentration negligible, we have:

$$r^2 = 2D\left(C - C_S\right)V_m t + r_o^{\,2} \tag{2.3}$$

For two particles with initial radius difference δr_0 the radius difference δr decreases as time increases or particles grow bigger, according to:

$$\delta r = \frac{r_o \delta r_o}{r} \tag{2.4}$$

These equations indicate that the radius difference decreases with increase of nuclear radius and prolonged growth time. The diffusion controlled growth promotes the formation of uniformly sized particles.

2.2.1.2.2. *Growth controlled by surface processes*

When the diffusion of growth species from the bulk to the growth surface is sufficiently rapid, the growth rate is controlled by the surface process. There are two mechanisms for the surface processes: *mononuclear growth* and *poly-nuclear growth*. For the *mononuclear growth*, the growth proceeds layer by layer; the growth species are incorporated into one layer and proceeds to another layer only after the growth of the previous layer is complete. There is a sufficient time for the growth species to diffuse on the surface. The growth rate is thus proportional to the surface area.

During *poly-nuclear growth*, which occurs when the surface concentration is very high, surface process is so fast that second layer growth proceeds before the first layer growth is complete. The growth rate of particles is independent of particle size or time. The relative radius difference remains constant regardless of the growth time and the absolute particle size [3]. Although the absolute radius difference remains unchanged, the relative radius difference would be inversely proportional to the particle radius and the growth time.

As particles get bigger, the radius difference becomes smaller; so this growth mechanism also favors the synthesis of monosized particles.

Figure 2.3 illustrates schematically the radius difference as functions of particle size for all three mechanisms of subsequent growth discussed above. It is obvious that a diffusion controlled growth mechanism is required for the synthesis of mono sized particles by homogeneous nucleation. It has been suggested that the growth of nanoparticles involve all three mechanisms [3]. When the nuclei are small, monolayer growth mechanism may dominate, poly-nuclear growth may become predominant as the nuclei become bigger. Diffusion is predominant for the growth of relatively large particles. But this would only be the case when no other procedures or measures were applied to prevent certain growth mechanisms. Naturally, different growth mechanisms can become predominant when particular favourable growth conditions are established.

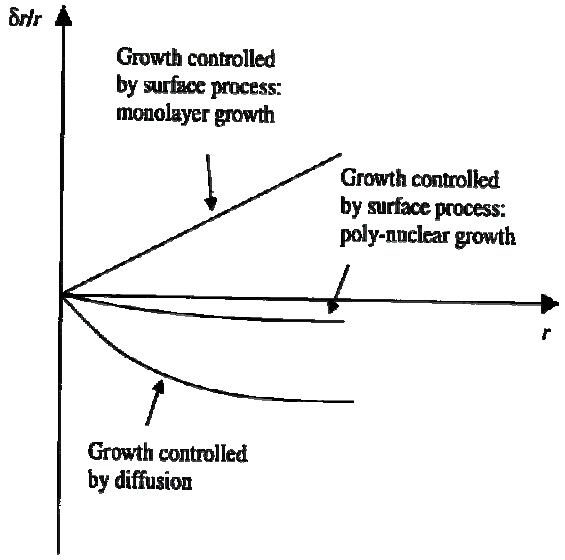

Figure 2.3: Diagram illustrating the radius difference as functions of particle size for all three mechanisms of subsequent growth [4].

For the formation of monosized nanoparticles, diffusion-limited growth is desired. There are several ways to achieve diffusion-limited growth. For example, when the concentration of growth species is kept extremely low, diffusion distance would be very large and consequently diffusion could become the limiting step. Increasing the viscosity of solution is another possibility. Introduction of a diffusion barrier such as a monolayer on the surface of a growing particle is yet another approach. Controlled supply of growth species offers another method to manipulate the growth process. When growth species is generated through chemical reactions, the rate of reaction can be manipulated through the control of the concentration of by-product, reactant and catalyst.

In the case of the synthesis of various types of nanoparticles through solution processes, formation of nanoparticles dispersed in a solvent is the most common approach

and offers several advantages such as: stabilization of nanoparticles from agglomeration, extraction of nanoparticles from solvent, surface modification and application, processing control and mass production.

2.2.2. Nanoparticles through Homogeneous Nucleation

Homogeneous nucleation comprises several available methods for synthesize zero-dimensional nanomaterials. Methods based on homogeneous nucleation are presented again in figure 2.4. Additionally in the scheme is showed the final products according to each technique. As one can infer, the final products could be metallic, semiconductor or both, depending on the used method. In this thesis work it has been considered to give a brief description of the approaches belonging to the homogeneous nucleation-based methods for synthesizing nanoparticles.

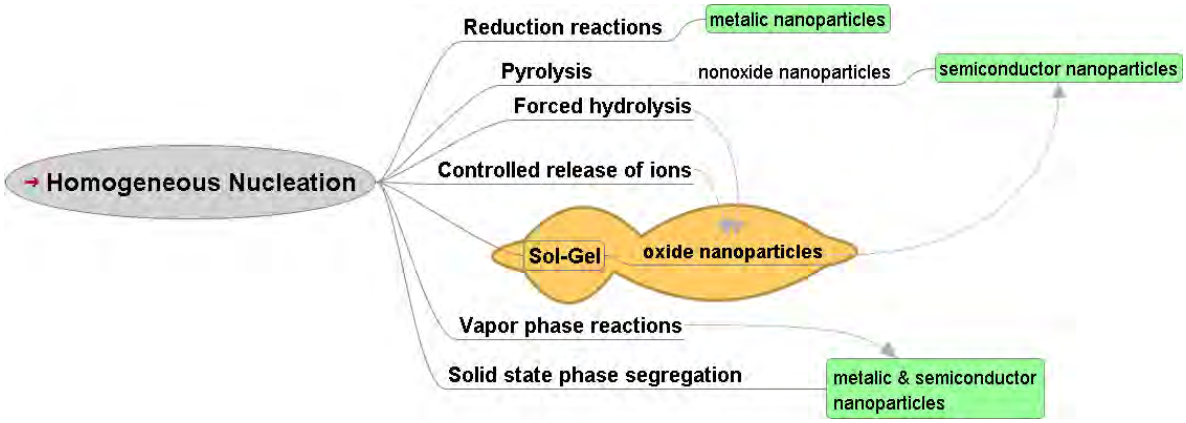

Figure 2.4: Synthesis methods based on homogeneous nucleation and resultant form of products.

2.2.2.1. Synthesis of metallic nanoparticles

Reduction of metal complexes in dilute solutions is the general method in the synthesis of metal colloidal dispersions. A variety of methods have been developed to initiate and control the reduction reactions [5–9]. The formation of mono sized metallic nanoparticles is achieved in most cases by a combination of a low concentration of solute and polymeric monolayer adhered onto the growth surfaces. Both low concentration and a polymeric monolayer would hinder the diffusion of growth species from the surrounding solution to the growth surfaces. So that the diffusion process is likely to be the rate limiting step of subsequent growth of initial nuclei resulting in the formation of uniformly sized nanoparticles.

In the synthesis of metallic nanoparticles, or more specifically, metallic colloidal dispersion, various types of precursors, reduction reagents, other chemicals, and methods were used to promote or control the reduction reactions, the initial nucleation and the subsequent growth of initial nuclei. Table 2.1 briefly summarizes the precursors, reduction

reagents and polymeric stabilizers commonly used in the production of metallic colloidal dispersions.

Summary of recursors, reduction reagents and polymer stabilizers	
Precursors	
Metal anode	Pd, Ni, Co
Palladium chloride	$PdCl_2$
Hydrogen hexachloroplatinate IV	H_2PtCl_6
Potassium tetrachloroplatinate II	K_2PtCl_4
Silver nitrate	$AgNO_3$
Silver tetraoxylchlorate	$AgClO_4$
Chloroauric acid	$HAuCl_4$
Rhodium chloride	$RhCl_3$
Reduction Reagents	
Hydrogen	H_2
Sodium citrate	$Na_3C_6H_5O_7$
Hydroxylamine hydrochloride	NH_4OH + HCl
Citric acid	$C_6H_8O_7$
Carbon monoxide	CO
Phosphorus in ether	P
Methanol	CH_3OH
Hydrogen peroxide	H_2O_2
Sodium carbonate	Na_2CO_3
Sodium hydroxide	NaOH
Formaldehyde	HCHO
Sodium tetrahydroborate	$NaBH_4$
Ammonium ions	NH_4-
Polymer stabilizers	
Poly(vinylpyrrolidone), PVP	
Polyvinylalcohol, PVA	
Polyethyleneimine	
Sodium polyphosphate	
Sodium polyacrylate	
Tetraalkylammonium halogenides	

Table 2.1: Summary of precursors, reduction reagents and polymer stabilizers related to the production of metallic colloidal dispersions [10].

Metallic nanoparticles can also be prepared by an electrochemical deposition method [11,12]. This method employs a simple electrochemical cell containing only a metal anode and a metal or glassy carbon cathode. The electrolyte consists of organic solutions of tetraalkylammonium halogenides, which also serve as stabilizers for the produced metal nanoparticles. Upon application of an electric field, the anode undergoes oxidative dissolution forming metal ions, which would migrate toward the cathode. The reduction of metal ions by ammonium ions leads to the nucleation and subsequent growth of metallic nanoparticles in the solution. With this method, nanoparticles of Pd, Ni and Co with diameters ranging from 1.4 to 4.8 nm have been produced. Furthermore, it was found that the current density has an appreciable influence on the size of metallic particles; increasing the current density results in a reduced particle size [11].

2.2.2.1.1. *Influences of reduction reagents*

The size and size distribution of metallic colloids vary significantly with the types of reduction reagents used in the synthesis. In general, a strong reduction reaction promotes a fast reaction rate and favours the formation of smaller nanoparticles [13,14]. A weak reduction reagent induces a slow reaction rate and favours relatively larger particles. However, a slow reaction may result in either wider or narrower size distribution. If the slow reaction leads to continuous formation of new nuclei or secondary nuclei, a wide size distribution would be obtained. On the other hand, if no further nucleation or secondary nucleation occurs, a slow reduction reaction would lead to diffusion-limited growth, since the growth of the nuclei would be controlled by the availability of the zerovalent atoms. Consequently, a narrow size distribution would be obtained.

2.2.2.1.2. *Influences of polymer stabilizer*

Polymer stabilizers are introduced primarily to form a monolayer on the surface of nanoparticles to prevent its agglomeration. However, its presence during the formation of nanoparticles can have various influences on the growth process [15]. Interaction between the surface of a solid particle and polymer stabilizer may vary significantly depending on the surface chemistry of solid, the polymer, solvent and temperature. A strong adsorption of polymer stabilizers would occupy the growth sites and thus reduce the growth rate of nanoparticles. A full coverage of polymer stabilizer would also hinder the diffusion of growth species from the surrounding solution to the surface of growing particle.

Polymer stabilizers may also interact with solute, catalyst, or solvent, and thus directly contribute to reaction. For example, it has been reported that PVP is actually a weak acid and capable of combining with hydroxyl ions [16]. As a result, the effective quantity of PVP as a stabilizer would be smaller than that was added. Polymer stabilizers have also been found to have catalytic effect on reduction reactions [17]. Furthermore, the pH of the solution would increase with an increasing concentration of PVP.

2.2.2.2. Synthesis of nonoxide nanoparticles

In the case of semiconductor nanoparticles, the methods can be grouped as synthesis for nonoxide and for oxide semiconductor, because their syntheses are significantly different from each other. Nonoxide semiconductor nanoparticles are commonly synthesized by pyrolysis of organometallic precursors dissolved in anhydrate solvents at elevated temperatures in an airless environment in the presence of polymer stabilizer or capping material [18–20]. It should be noted that in the synthesis of metallic nanoparticles, polymers attached on the surface are commonly termed as *polymer stabilizers*. However, in the synthesis of semiconductor nanoparticles, polymers on the surface are generally referred to as *capping materials.* Capping materials are linked to the surface of nanocrystallites via either covalent bonds or by other kind such as dative bonds [21].

The formation of monodispersed semiconductor nanocrystallites is generally achieved by the following approaches [1]. First, temporally discrete nucleation is attained by a rapid increase in the reagent concentrations upon injection, resulting in an abrupt supersaturation. Second, Ostwald ripening during aging at increased temperatures promotes the growth of large particles at the expense of small ones, narrowing the size distribution. Third, size selective precipitation is applied to further enhance the size uniformity. It is noted that although organic molecules are used to stabilize the colloidal dispersion, similar to that in the formation of metallic colloidal dispersions, the organic mono layers on the surfaces of semiconductor nanoparticles play a relatively less significant role as a diffusion barrier during the subsequent growth of initial nuclei. This is because there is a less extent or negligible subsequent growth of initial nuclei due to the depletion of growth species and the drop of temperature at the nucleation stage.

An increased temperature results in an increased solubility, and thus a reduced supersaturation of growth species in the solution. As a result, nuclei with small sizes may become unstable and dissolve back into the solution; dissolved species will then deposit onto the surfaces of large particles. This dissolution-growth process is also known as Ostwald ripening, in which large particles grow at the expense of small particles [22]. Such a growth process would result in the production of highly mono dispersed colloidal dispersions from systems that may initially be polydispersed [23]. An increased temperature will promote the growth of nanoparticles with a narrow size distribution. The effect of lowering the synthesis temperature results in a wider size distribution with an increased amount of small particles. A lowered temperature would result in an increased supersaturation favoring continued nucleation with smaller sizes. Thermal decomposition of complex precursor in a high-boiling solvent represents another method in the production of compound semiconductor nanoparticles with a narrow size distribution [24,25].

Size-selective precipitation would further narrow the size distribution of the colloids prepared. For the fraction process to work well it is crucially important that the shape and surface derivation of the initial crystallites be uniform and that the initial polydispersity in size be relatively small [26]. It should be noted that although the subsequent growth of initial nuclei appears less important in the monodispersed semiconductor synthesis as compared to that of monodispersed metal nanoparticles (due to the depletion of reagents as discussed above), the capping material provides an important steric barrier for diffusion and thus favours the diffusion controlled subsequent growth of existing nuclei.

2.2.2.3. Synthesis of oxide nanoparticles

Compared to the synthesis of metallic and non-oxide nanoparticles, the approaches used in the fabrication of oxide nanoparticles are less elaborated and there are less defined general strategies for the achievement of monosized distribution. Although all the fundamental considerations for homogeneous nucleation and diffusion controlled subsequent growth are applicable to the oxide systems, the practical approaches vary noticeably from system to system. Reaction and growth in the formation of oxide nanoparticles are more difficult to manipulate since oxides are generally more stable thermally and chemically than most semiconductors and metals.

2.2.2.3.1. *Forced hydrolysis*

The simplest method for the generation of uniformly sized colloidal metal oxides is based on forced hydrolysis of metal salt solutions. It is well known that most polyvalent cations readily hydrolyze and that deprotonation of coordinated water molecules is greatly accelerated with increasing temperature. Since hydrolysis products are intermediates to precipitation of metal oxides, increasing temperature results in an increasing amount of deprotonated molecules. When the concentration far exceeds the solubility, nucleation of metal oxides occurs. In principle, to produce such metal oxide colloids, one just needs to age hydrolyzed metal solutions at elevated temperatures. It becomes obvious that hydrolysis reaction should proceed rapidly and produce an abrupt supersaturation to ensure a burst of nucleation, resulting in the formation of a large number of small nuclei, eventually leading to the formation of small particles [27].

Both hydrolysis and condensation reactions, as any other chemical reactions, are strongly dependent on reaction temperatures. An elevated temperature would result in a drastic increase of reaction rate. The high temperature favours a fast hydrolysis reaction and results in the high supersaturation that in turn leads to the formation of a large number of small nuclei. Dilution before heating to high temperatures is very important to ensure a controlled nucleation and subsequent diffusion-limited growth. A long aging period would permit the occurrence of Ostwald ripening to further narrow the size distribution.

2.2.2.3.2. *Controlled release of ions*

Controlled release of constituent anions or cations has a significant influence on the kinetics of nucleation and subsequent growth of oxide nanoparticles. It is achieved by the spontaneous release of anions from organic molecules. Solutions of urea $CO(NH_2)_2$ when heated liberate hydroxide ions which can cause precipitation of metal oxide or hydroxide [28,29]. For example, the decomposition of urea is used to control the nucleation process in the synthesis of Y_2O_3: Eu nanoparticles [30]. Yttrium and europium chlorides were dissolved in water and the pH was adjusted to ~1 with hydrochloride acid or potassium hydroxide. An excess of urea, typically 15x, was dissolved into the solution. The solution was then raised to > 80 °C for 2 hours. The urea decomposed slowly and there was a burst of nucleation when a certain pH value of ~4-5 was reached.

In general, certain types of anions are commonly introduced into the system as a catalyst. In addition to the catalytic effect, anions commonly exert other influences on the processing and the morphology of the nanoparticles [31].

2.2.2.3.3. S*ol-gel processing*

The most studied and best-established example of oxide colloidal is silica colloids [32] though various oxide nanoparticles have been studied [33,34]. Commonly oxide particles in colloidal dispersions are synthesized by sol-gel processing. Sol-gel processing is also commonly used in the fabrication of various core-shell nanostructures [35] and

surface engineering of nanostructures [36]. Before discussing the general approaches for the synthesis of oxide nanoparticles, let us briefly discuss the sol-gel processing first.

Sol-gel processing is a wet chemical route for the synthesis of colloidal dispersions of inorganic and organic-inorganic hybrid materials, particularly oxides and oxide-based hybrids. From such colloidal dispersions, powders, fibers, thin films and monoliths can be readily prepared. Although the fabrication of different forms of final products requires some specific considerations, the fundamentals and general approaches in the synthesis of colloidal dispersions are the same. Sol-gel processing offers many advantages, including low processing temperature and molecular level homogeneity. Sol-gel processing is particularly useful in making complex metal oxides, temperature sensitive organic-inorganic hybrid materials, and thermodynamically unfavorable or metastable materials [37].

By a careful control of sol preparation and processing, monodispersed nanoparticles of various oxides, including complex oxides, organic-inorganic hybrids, and biomaterials, can be synthesized. The key issue is to promote temporal nucleation followed by diffusion-controlled subsequent growth. The particle size can be varied by changing the concentration and aging time [37]. In a typical sol, nanoclusters formed by hydrolysis and condensation reactions commonly have a size ranging from 1 to 100 nm. It should also be noted that in the formation of mono dispersed oxide nanoparticles, the stabilization of colloids is generally achieved by electrostatic double layer mechanism. Therefore, polymer steric diffusion barrier existing in the formation of metal and non-oxide semiconductor colloids is generally not present in the formation of metal oxides. So the diffusion controlled growth is achieved through other mechanisms such as controlled release and a low concentration of growth species in the sol.

Typical sol-gel processing consists of hydrolysis and condensation of precursors. Precursors can be either metal alkoxides or inorganic and organic salts. Organic or aqueous solvents may be used to dissolve precursors, and catalysts are often added to promote hydrolysis and condensation reactions. The specific sol-gel process applied for the synthesized nanoparticles is described on next chapter.

2.2.2.4. Synthesis for metallic and semiconductor nanoparticles

There are some methods that are applicable for both metallic and semiconductor nanoparticles, such as *vapour phase reactions* and *solid state phase segregation*. Following is given a brief description of these methods.

2.2.2.4.1. *Vapor phase reactions*

Nanoparticles can also be synthesized by vapor phase reactions following the same mechanisms as in the synthesis of nanoparticles in liquid medium. In general, reaction and synthesis are carried out at elevated temperatures and under a vacuum. Vacuum is needed to ensure a low concentration of growth species so as to promote diffusion-controlled subsequent growth. Grown nanoparticles are normally collected on a non-sticking substrate

placed down stream at a relatively low temperature. Obviously only a small fraction of nanoparticles do settle on the substrate surface. Furthermore, the nanoparticles that settled on the substrate surface may not represent the true particle size distribution. It is also difficult to introduce stabilization mechanism during synthesis to prevent the formation of agglomerates. Despite the aforementioned challenges, it has been demonstrated that various nanoparticles can be synthesized by vapor phase reactions. For example, the gas aggregation technique has been applied in the synthesis of silver nanoparticles of 2-3 nm in diameter [38]. Another example is the production of highly dispersed silica particles less than 100 nm in diameter by combustion of silicon tetrachloride in a hydrogen torch [39].

2.2.2.4.2. ***Solid state phase segregation***

Nanoparticles of metals and semiconductors in glass matrix are commonly formed by homogeneous nucleation in solid state [40,41]. First the desired metal or semiconductor precursors were introduced to and homogeneously distributed in the liquid glass melt at high temperatures during glass making, before quenching to room temperature. Then the glass was annealed by heating to a temperature about the glass transition point and held for a pre-designed period of time. During the annealing, metal or semiconductor precursors were converted to metals and semiconductors. As a result, supersaturated metals or semiconductors formed nanoparticles through nucleation and subsequent growth via solid-state diffusion.

Homogeneous glasses are made by dissolving metals, in the form of ions, in the glass melts and then rapidly cooled to room temperature. In such glasses metals remain as ions [42]. Upon reheating to an intermediate temperature region, metallic ions are reduced to metallic atoms by certain reduction agents such as antimony oxide that is also added into the glasses. Metallic nanoparticles can also be nucleated by ultraviolet, X-ray, or γ-ray radiation if a radiation-sensitive ion such as cerium is present [42]. The subsequent growth of the nuclei takes place by solid-state diffusion [43]. For example, glasses with nanoparticles of gold [42], silver [44] and copper [45] can all be prepared with such an approach. Although metallic ions may be highly soluble in the glass melts or glasses, metallic atoms are not soluble in glasses. When heated to elevated temperatures, metallic atoms acquire needed diffusivity to migrate through the glasses and subsequently form nuclei. These nuclei would grow further to form nanoparticles of various sizes. Since solid-state diffusion is relatively slow, it is relatively easy to have a diffusion-controlled growth for the formation of mono sized particles.

Nanoparticles dispersed in glass matrix can be synthesized through sol-gel processing as well. There are two approaches: (i) mixing presynthesized colloidal dispersion with matrix sol before gelation, and (ii) making a homogeneous sol containing desired ions for the formation of nanoparticles first and annealing the solid product at elevated temperatures.

2.3. NANOSCALE CHARACTERIZATION

The task of making structures on nanometer scales, already complex, is further complicated by the difficulty of "seeing" what is taking place at these extreme dimensions. The properties and improved performance exhibited by nanomaterials are strongly dependent on their composition, size, surface structure, and inter-particle interactions. Hence characterization of these properties is important in the development of nanomaterials and in understanding structure-function relationship. This requires the use of different microscopic and spectroscopic methods suitable for investigation of nanostructures that here will be briefly described [46].

2.3.1. X-Ray Diffraction

X-ray diffraction, often abbreviated as XRD, is extensively used to characterize the crystalline structure of nanoparticles and to estimate the crystalline sizes [47]. It often utilizes X-ray diffraction from nanoparticles in powder form, which is thus called powder diffraction [48]. A comprehensive review of powder diffraction is provided by Langford and Louer (1996). It is based on the principle of elastic scattering of X-rays by a periodic lattice characterized by long-range order. It is a reciprocal space-based method (that is, it gives information about types of periodicity present in the material, rather than the real space distribution of individual atoms), and it gives an ensemble average information on the crystal structure and the particles size of a nanostructured material. When a beam of monochromatic X-rays hits on a sample, the ray penetrates the sample and gets diffracted by the periodic lattice of a crystalline material, according to the well-known Bragg's equation:

$$n\lambda = 2d \cdot \sin\theta \tag{2.5}$$

where n is an integer, λ is the X-ray wavelength, *d* is the spacing between crystallographic planes giving rise to a particular diffracted beam and θ is the incidence angle.

The diffraction pattern generated by constructive interference of the scattered X-rays provides crystallographic information on the materials. In the case of nanomaterials, the sample can be in form of powder or as a thin film that is exposed to a beam of X-rays, where the angle of incidence is varied. For a sample consisting of polycrystalline (powder) materials, the X-ray diffractogram is a series of peaks conforming to the values where Bragg's law of diffraction is satisfied.

Nanoparticles, less than approximately 100 nm in size, show appreciable broadening of their X-ray diffraction lines. The observed line broadening can be used to estimate the average size of the nanocrystals (or crystalline domains). In the simplest case of stress-free particles, the size can be estimated from a single diffraction peak. The particle/grain size, *D*, is related to the X-ray line broadening by Scherrer's formula [47]:

$$D = \frac{0.9\lambda}{\beta \cdot \cos\theta} \tag{2.6}$$

where λ is the wavelength, θ is the diffraction angle, and β is the corrected full width (in radian) at half-maximum intensity. In those cases where stress may be present, a more rigorous method involving several diffraction peaks is required. However, Scherrer's formula should be used only as a rough guide for particle size. Particle size distribution (if there is polydispersity) and/or the presence of stress often provide results for crystallite sizes (average values) that are different from those obtained by TEM. A significant development in the XRD study of nanostructured materials is the use of synchrotron sources providing very bright and continuous spectrum of X-ray radiations, allowing studying small quantities of nanoparticles.

A significant development in the XRD study of nanostructured materials is the use of synchrotron sources providing very bright and continuous spectrum of X-ray radiations, allowing studying small quantities of nanoparticles.

2.3.2. X-Ray Photoelectron Spectroscopy

X-ray photoelectron spectroscopy (XPS), also commonly known as electron spectroscopy for chemical analysis (ESCA), is used to study the composition and electronic states of the surface region of a sample. It makes use of the photoelectric effect in which a photon (X-ray in this case) strikes the surface of a material to eject electrons that leave the surface with various energies. This technique is capable of providing information on the oxidation states, immediate chemical environment, and concentration of the constituent atoms [49].

The sample is irradiated with a monochromatic soft X-ray beam of energy in the range 200-2000 eV. These X-ray photons have a limited penetration depth depending on the angle of incidence, photon energy, and the material under study. The kinetic energy, with which the photoelectron leaves, is a function of the binding energy and hence of the chemical environment of the particular atom. Only the electrons from the first few nanometers of the sample surface are generally probed in this method. The electrons leaving the sample are detected by an electron spectrometer according to their kinetic energy.

The XPS of a specimen is represented by a spectrum displaying the flux of emitted electrons as a function of the binding energy (determined from the kinetic energy of the ejected electron). This spectrum gives information about different elements on the sample surface such as peaks due to contaminants and atomic concentrations. The peaks areas are used (with appropriate sensitivity factors) to determine the concentrations of the constituent elements. The shape of each peak and the binding energy can be slightly altered by the chemical state of the emitting atom.

2.3.3. Electron Microscopy

Electron microscopy has emerged as a powerful tool for characterization of the size and shape of nanostructured materials [50]. Like optical microscopy, it provides an image

of the material in direct space. However, the nanometer scale resolution provided by electron microscopes is highly suitable for imaging of nanomaterials, whereas the resolution provided by common optical microscopes is in hundreds of nanometers. Even for UV light, an optical microscope is limited to the resolutions of ~200 nm. Electron microscopes utilize electrons of energies in the few thousand electron volt range, which is a thousand times greater than that of a visible photon of energy ~2 to 3 eV. Using the de Broglie equation $\lambda = \hbar p$ for relation between the wavelength λ, and the momentum *p*, the wavelength of an electron of energy ~3600 eV is calculated to be 0.02 nm. But, because of the aberrations of an electron lens the resolution actually achieved is significantly less. However, a resolution of 0.1 nm can be obtained with an electron microscope.

The two principal electron microscopy methods described here are transmission electron microscopy (TEM) and scanning electron microscopy (SEM). TEM is the electron microscopic analogue of transmission optical microscope in which a focused beam of electrons is used, instead of light, to see through (using transmitted electrons) the specimen. SEM involves scanning of a focused electron beam across the sample.

In next sections SEM, TEM and HRTEM are briefly presented describing some of the pluses and minuses of each. The intention is to provide basic information on the fundamentals of the main characterization methods currently available [51].

2.3.3.1. Scanning Electron Microscopy (SEM)

The old standby SEM operates by magnetically scanning a focused electron beam typically from 1 kV to 40 kV in energy across the surface of a sample in high vacuum. The incident electrons, upon interacting inelastically with the sample material, produce secondary electrons. Positioned close to the sample is a detector that picks up some of the secondary electron yield. By measuring the detector response as the beam is rastered over the sample an image is constructed. Electron beam sources are either thermal emission from heated *W* or *LaB* filaments, or field emission. Figure 2.6 shows an SEM image.

Sample requirements. The sample in SEM needs to be at least a little bit conducting and grounded. Really insulating samples present an imaging challenge because charging of the sample can deflect later beam scans resulting in a distorted image. Often insulating samples are sputter coated with a very thin layer of metal to aid in imaging. Further, a clean sample surface is highly desirable since the local energy deposition of the electron beam can cause chemical changes in any surface layer of contaminants, ruining the sample. Sample materials with high Z such as Au produce high secondary yields and look "bright" in SEM micrographs, while light elements are more difficult to image.

Resolution limits. SEM resolution is limited by the beam spot size (can be as small as 1 nm), beam jitter, and the spread of secondary electron yield. There is a trade off that goes on between beam energy and resolution of fine surface features. On the one hand, high incident energies mean reduced transit times between emitter and detector and so reduced vulnerability to vibrational noise. However, higher energies mean that the secondary yield takes place deeper into the sample material making it difficult to resolve surface detail.

Other limitations. In most SEM chambers, there is frequently a dilute gas of hydrocarbon junk drifting around often due to back streaming from pumps or improperly degreased chamber construction components. The electron beam can cause some kind of reaction which deposits carbon from this junk onto the sample. On larger scale objects this is not a big deal since the layer is usually thin (~20 Å for a few minutes of viewing over a 0.5 μm^2 area) and carbon is fairly transparent because of its low Z. However, on real nanoscale objects this is clearly very serious and can limit SEM imaging to a one-shot procedure for noncritical samples.

2.3.3.2. Transmission Electron Microscopy (TEM)

TEM is an extremely powerful technique that can give truly atomic resolution images. As one might infer from the name, it is similar to SEM but works by firing an energetic (between 100 and 500 kV) beam of electrons with a very small spot size thrown to the sample, through some more optics and onto a detector. Imaging techniques include bright field imaging where widely scattered electrons miss the detector and bright spots indicate transmission; and dark field imaging where the minimally scattered electrons are diverted and scatterers show up as bright spots. One can also do electron diffraction and holography looking at interference effects between unscattered and scattered electrons. All of these approaches require a bright coherent source of electrons.

Sample requirements. To get decent transmittance, bulk samples must be thinned down to a few hundred nm thickness usually by mechanical polishing followed by ion milling. TEM sample preparation is truly an application of enhanced skill. Some very impressive results have been seen recently in nanoscale images with *in situ* sample fabrication.

Resolution limits. True atomic-resolution images are possible with TEM though it is a complex proceeding. Thicker samples lead to more contrast while simultaneously leading to more multiple scatterings and reduced transmittance.

Variations. One very powerful variation is electron energy loss spectroscopy (EELS) where a sensitive calorimeter looks at the energy of transmitted electrons. This allows imaging at the band structure of the sample.

2.3.3.3. High Resolution Transmission Electron Microscopy (TEM)

High Resolution Transmission Electron Microscopy (HRTEM) is an imaging mode of the transmission electron microscope (TEM) that allows the imaging of the crystallographic structure of a sample at an atomic scale. HRTEM can provide structural information at better than 0.2 nm spatial resolution [52]. At lower resolution, amplitude contrast images can be used to observe material features in the 1μm-0.5nm range [53]. Because of its high resolution, it is an invaluable tool to study nanoscale properties in most crystalline inorganic materials, including ceramics, semiconductors and metals, where the positions of individual atomic columns can be resolved, at least in low-index zones [54].

When recorded under optimum conditions, electron micrographs can be directly interpreted in terms of the projected crystal potential. In other cases, image simulations are necessary to match proposed structures to image features [55].

As opposed to conventional microscopy, HRTEM does not use amplitudes (i.e. absorption by the sample) for image formation. Instead, contrast arises from the interference in the image plane of the *electron wave* with itself. Due to our inability to record the phase of these waves, we generally measure the amplitude resulting from this interference; however the phase of the electron wave still carries the information about the sample and generates contrast in the image, thus the name phase-contrast imaging. This is true only if the sample is thin enough so that amplitude variations do not contribute to the image (known as *weak phase object approximation*, WPOA).

First however, both phase and amplitude of the electron wave in the image plane must be measured. As our instruments only record amplitudes, an alternative method to recover the phase has to be used. At present there are two methods in use:

Holography. Developed by Gabor expressly for TEM applications, uses a prism to split the beam into a reference beam and a second one passing through the sample. Phase changes between the two are then translated in small shifts of the interference pattern, which allows recovering both phase and amplitude of the interfering wave.

Focal series method. Takes advantage of the fact that the CTF is focus dependent. A series of about 20 pictures is shot under the same imaging conditions with the exception of the focus which is incremented between each take. Together with exact knowledge of the CTF the series allows for computation of the *exit wave* phase.

As a result of the interaction with the sample, the electron *exit wave* right below the sample is a superposition of a plane wave and a multitude of diffracted beams with different in plane spatial frequencies. The *exit wave* now passes through the imaging system of the microscope where it undergoes further phase change and interferes as the *image wave* in the imaging plane (photo plate or CCD). It is important to realize that the recorded image is not a direct representation of the samples crystallographic structure. The relationship between the *exit wave* and the *image wave* is a highly nonlinear one and is a function of the aberrations of the microscope. It is described by the contrast transfer function (CTF).

The phase Contrast Transfer Function (CTF) is a function of limiting apertures and aberrations in the imaging lenses of a microscope. It describes their effect on the *exit wave* phase and propagates it to the *image wave*. To calculate back the phase of the *exit wave*, the wave in the image plane is back propagated numerically to the sample. If all properties of the microscope are well known, it is possible to recover the real *exit wave* phase with very high accuracy.

Sample requirements. For highest resolution, specimens must be <10nm thick. In general, specimens prepared by chemical thinning, crushing, or ion beam milling will contain

suitable regions. High magnification imaging requires high electron dose, so specimens need to be relatively beam insensitive. The technique, by itself, provides very limited chemical information. Heating experiments must be designed to minimize contamination of the microscope.

Resolution limits. One of the difficulties with HRTEM is that image formation relies on phase-contrast. In phase contrast imaging, contrast is not intuitively interpretable as the image is influenced by strong aberrations of the imaging lenses in the microscope.

Some alternative characterization techniques that were not described are Scanned Probe Microscopy (SPM), Atomic Force Microscopy (AFM), Magnetic Force Microscopy (MFM), Electrostatic Force Microscopy (EFM), Magnetic Resonance Force Microscopy (MRFM), Scanning Tunnelling Microscopy (STM), Near Field Scanning Optical Microscopy (NSOM), among others. The list presented here is by no means exhaustive, and new techniques are being developed all the time. In this dynamic area there are several developments of new techniques, and a wealth of new information is learned, some of which may lead to other new methods.

REFERENCES AND NOTES

[1] Guozhong Cao, *Nanostructures & Nanomaterials*. Imperial College Press. 2004
[2] A.E. Nielsen, *Kinetic of Precipitation*, MacMillan, New York, 1964
[3] R. Williams, P.M. Yocom, and F.S. Stofko, *J. Colloid Interf. Sci*. **106**, 388 (1985)
[4] Figure appeared in [1].
[5] A. Henglein, *Chem. Rev*. **89**, 1861 (1989)
[6] Z.L. Wang, *Adv. Mater*. **10**, 13 (1998)
[7] G. Schmid, *Chem. Rev*. **92**, 1709 (1992)
[8] G. Schmid (ed), *Clusters and Colloids*, VCH, New York, 1994
[9] G. Schon and U. Simon, *Colloid Polym Sci*. **273**, 101 (1995)
[10] Table 3.1 appeared in [1]
[11] M. T. Reetz and W. Helbig, *J. Am. Chem. Soc*. **116**, 7401 (1994)
[12] J. A. Becker, R. Schafer, R. Festag, W. Ruland, J. H. Wendorff, J. Pebler, S. A. Quaiser, W. Helbig and M. T. Reetz, *J. Chem. Phys*. **103**, 2520 (1995)
[13] K. H. Lieser, Angew. *Chem. Int. Ed. Engl*. **8**, 188 (1969)
[14] V. K. La Mer, *Ind. Eng. Chem. Res*. **44**, 1270 (1952)
[15] A. Henglein, *Chem. Mater*. **10**, 444 (1998)
[16] K. Chou and C. Ren, Mater. *Chem. Phys*. **64**, 241 (2000)
[17] A. Henglein, B. G. Ershov, and M. Malow, *J. Phys. Chem*. **99**, 14129 (1995)
[18] M. L. Steigerwald and L. E. Brus, *Acc. Chem*. Res. **23**, 183 (1990)
[19] M. G. Bawendi, M. L. Steigerwald and L. E. Brus, *Annu. Rev. Phys. Chem*. **41**, 477 (1990)
[20] C. B. Murray, C. R. Kagan, and M. G. Bawendi, *Ann. Rev. Mater. Sci*. **30**, 545 (2000)
[21] S. A. Majetich and A. C. Carter, *J. Phys Chem*. **97**, 8727 (1993)
[22] A. L. Smith, *Particle Growth in Suspensions*, Academic Press, New York, 1983
[23] H. Reiss, *J. Chem. Phys*. **19**, 482 (1951)
[24] O. I. Mićić, J. R. Sprague, C. J. Curtis, K. M. Jones, J. L. Machol, A. J. Nozik, H. Huyesen, B. Fluegel, G. Mohs, and N. Peyghambarian, *J. Phys. Chem*. **99**, 7754 (1995)
[25] O. I. Mićić, J. R. Sprague, C. J. Curtis, K. M. Jones, J. L. Machol, A. J. Nozik, *J. Phys. Chem*. **98**, 4966 (1994)
[26] C. B. Murria, D. J. Norris, and M. G. Bawendi, *J. Am. Chem*. Soc. **110**, 3046 (1988)
[27] W. Stöber, A. Finx, and E. Bohn, *J. Colloid Interf. Sci*. **26**, 62 (1968)
[28] E. Matijević, and W. P. Hsu, *J. Colloid Interf. Sci.* **118**, 506 (1987)
[29] G. Wakefield, E. Holland, P. J. Dobson, and J. L. Hutchison, *Adv. Mater*. **13**, 1557 (2001)
[30] D. Sordelet and M. Akinc, *J. Colloid Interf. Sci.* **122**, 47 (1988)
[31] E. Matijević, *Ann. Rev. Mater.* **15**, 483 (1985)
[32] R. K. Iler, *The Chemistry of Silica: Solubility, Polymerization, Colloid and Surface Properties, and Biochemistry*, Willey, New Cork, 1979
[33] E. Matijević, *Chem. Mater.* **5**, 412 (1993)
[34] E. Matijević, *Langmuir* **10**, 8 (1994)
[35] S. T. Selvan, C. Bullen, M. Ashokkumar, and P. Mulvaney, *Adv. Mater*. **13**, 985 (2000)
[36] F. Caruso, *Adv. Mater*. **13**, 11 (2001)

[37] For more details, readers may wish to consult the abundant literature in this field. For instance, the following provide an excellent and comprehensive coverage on sol-gel processing and materials:
C. J. Brinker and G. W. Scherer, *Sol-Gel Science: the Physics and Chemistry of Sol-Gel Processing*, Academic Press, Sand Diego, CA, 1990
Alain C. Pierre, *Introduction to Sol-Gel Processing*, Kluwer, Boston, MA, 1998
J. D. Wright and N.A.J.M. Sommerdijk, *Sol-Gel Materials: Chemistry and Applications*, Gordon and Breach Science Publishers, Amsterdam, 2001
[38] S. A. Nepijko, D. N. Levlev, W. Schulze, J. Urban, and G. Erlt, *Chem. Phys. Chem*. **3**, 140 (2000)
[39] E. Wagner and H. Brünner, *Angew. Chem*. **72**, 744 (1960)
[40] M. Yamane and Y. Asahara, *Glasses for Photonics*, Cambridge Univ. Press, Cambridge, 2000
[41] R. H. Doremus, *Glass Science*, 2nd edition, John Wiley & Sons, New York, 1994
[42] S. D. Stookey, *J. Am. Ceram. Soc*. **32**, 246 (1949)
[43] R. H. Doremus, in *Nucleation and Crystallization in Glasses and Melts*, the American Ceramic Society, Columbus, OH, p.117, 1967
[44] R. H. Doremus, *J. Chem. Phys.* **41**, 414 (1965)
[45] R. H. Doremus, S.C. Kao, and R. Garcia, *Appl. Opt.* **31**, 5773 (1992)
[46] Wang, Z. L., ed. *Characterization of Nanophase Materials*, Wiley-VCH, Weinheim, Germany, 2000
[47] For more details it is suggested Cullity, B. D. and Stock, S. R., *Elements of X-ray Diffraction*, 3rd edition, Prentice Hall, Upper Saddke River, NJ, 2001
[48] A comprehensive review of powder diffraction is provided by Langford, J. I., and Louër, D., Powder Diffraction, *Rep. Prog. Phys*. **59**, 131-234 (1996)
[49] A good reference source for XPS is the three-volume-set handbook by Crist, B. V., *Handbook of Monochromatic XPS Spectra*, 3-Volume Set, John Wiley & Sons, New York, 2000
[50] Heimendahl, M. V., *Electron Microscopy of Materials: An Introduction*, Academic Press, New York, 1980
[51] For technique details, recommended literature are:
Brundle, C. R.; Evans, C. A., and Wilson, S., *Encyclopedia of Materials Characterization*, Butterworth-Heinemann, Stoneham, MA, 1992
Vickerman, J. C., *Surface Analysis: The Principle Techniques*, John Wiley & Sons, New York, 1997
[52] D.J. Smith. *Reports Prog. Phys*. p 1513-1580. (1997)
[53] P. Hirsch, et al, in: *Electron Microscopy of Thin Crystals*. Krieger, Malabar FLA. 1977
[54] P.R. Buseck, J.M. Cowley, and L. Eyring. *High-Resolution Transmission Electron Microscopy and Associated Techniques*. Eds. Oxford University Press. New York. 1988
[55] J.C.H. Spence, in: *Experimental High Resolution Electron Microscopy*. Oxford University Press, 2nd ed. 1988

Chapter 3

Synthesis and Structural Characterization of ZrO_2:Yb^{3+}, Er^{3+} Nanocrystals

3.1. SOL – GEL PROCESS OVERVIEW

The goal of sol-gel processing and ultrastructure processing in general is to control the surfaces and interfaces of materials during the earliest stages of production [1]. The emphasis is on limiting and controlling physical and chemical variability by the production of uniquely homogeneous structures or producing extremely fine-scale (10-100 nm) phases. Creating controlled surface, compositional gradients and achieving unique physical properties by combining inorganic and organic materials are also goals of ultrastructure processing.

Three approaches are used to prepare advanced materials by sol-gel process:

- Method 1. Gelation of a solution of colloidal powders
- Method 2. Hydrolysis and polycondensation of oxide or nitrate precursors followed by hypercritical drying of gels
- Method 3. Hydrolysis and polycondensation of alkoxide precursors followed by aging and drying under ambient atmospheres.

Sols are dispersions of colloidal particles in a liquid. *Colloids* are solid particles with diameters of 10-100 nm [2]. A *gel* is an interconnected, rigid network with pores of submicrometer dimensions and polymeric chains whose average length is greater than a micrometer. The term "gel" embraces a diversity of combinations of substances that can be classified in four categories [3]: (i) well-ordered lamellar structures; (ii) covalent polymeric networks, completely disordered; (iii) polymer networks formed through physical aggregation, predominantly disordered; and (iv) particular disordered structures.

For example, a silica gel may be formed by network growth from an array of discrete colloidal particles (method 1) or by formation of an interconnected 3-D network by the simultaneous hydrolysis and polycondensation of an organometalic precursor (methods 2 and 3). When the pore liquid is removed as a gas phase from the interconnected solid gel network under hypercritical conditions (critical-point drying, method 2), the network does not collapse and a low density *aerogel* is produced. Aerogels can have pore volumes as large as 98% and densities as low as 80 kg /m^3 [4]. When the pore liquid is removed at or near ambient pressure by thermal evaporation (called drying, used in methods 1 and 3) and shrinkage occurs, the monolith is termed a *xerogel*. If the pore liquid is primarily alcohol based, the monolith is often termed an *alcogel*. The generic term *gel* usually applies to either aerogels or alcogels, whereas aerogels are usually designated as such.

A gel is defined as *dried* when the physically adsorbed water is completely evacuated. This occurs between 100 and 180 °C. The surface area of dried gels made by method 3 is very large (>400 m^2/g), and the average pore radius is very small (<10 nm). Larger pore radii can be produced by thermal treatment [5], by chemical washing during aging [6] or by additions of HF to the sol [7]. A dried gel still contains a very large concentration of chemisorbed hydroxyls on the surface of the pores. Thermal treatment in the range 500 –800 °C desorbs the hydroxyls and thereby decreases the sensitivity of the gel to rehydration stresses, resulting in a *stabilized* gel.

Heat treatment of a gel at elevated temperatures substantially reduces the number of pores and their connectivity, this is termed *densification*. The density of the monolith increases and the volume fraction of porosity decreases during sintering. The porous gel is transformed to a dense glass when all pores are eliminated. Densification is complete at 1250 – 1500 °C for silica gels made by method 1 and as low as 1000 °C for gels made by method 3, in general such temperature depend on the type of material [8]. The densification temperature decreases as the pore radius decreases and surface area of the gels increases.

3.1.1. Sol – Gel Process Steps

The processing steps involved in making sol-gel-derived zirconium oxide samples are briefly described below. Detailed explanations of synthesis process for other materials are well described in the reference [9].

Step I: Mixing. In method 1, a suspension of colloidal powders or sol, is formed by mechanical mixing of colloidal particles in water at a pH that prevents precipitation [10]. In methods 2 and 3, the one we are using, a liquid alkoxide precursor such as $Zr(OR)_4$ (where R is CH_3, C_2H_5, or C_3H_7) is hydrolyzed by mixing with water as it is shown in figure 3.1.

Figure 3.1: Chemical equation for hydrolysis.

The hydrated tetrahedra interact in a condensation reaction (figure 3.2), hence forming ≡Zr–O–Zr≡ bonds.

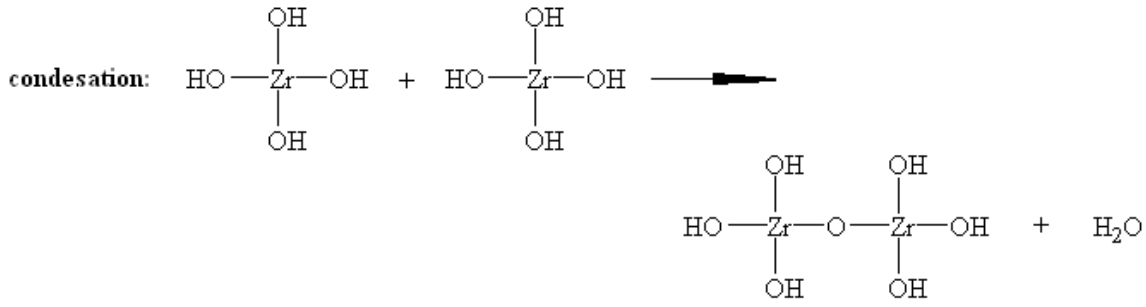

Figure 3.2: Chemical equation for condensation.

Linkage of additional ≡Zr–OH tetrahedra occurs as a polycondensation reaction (figure 3.3) and eventually results in a ZrO_2 network. The H_2O and alcohol expelled from the reaction remains in the pores of the network.

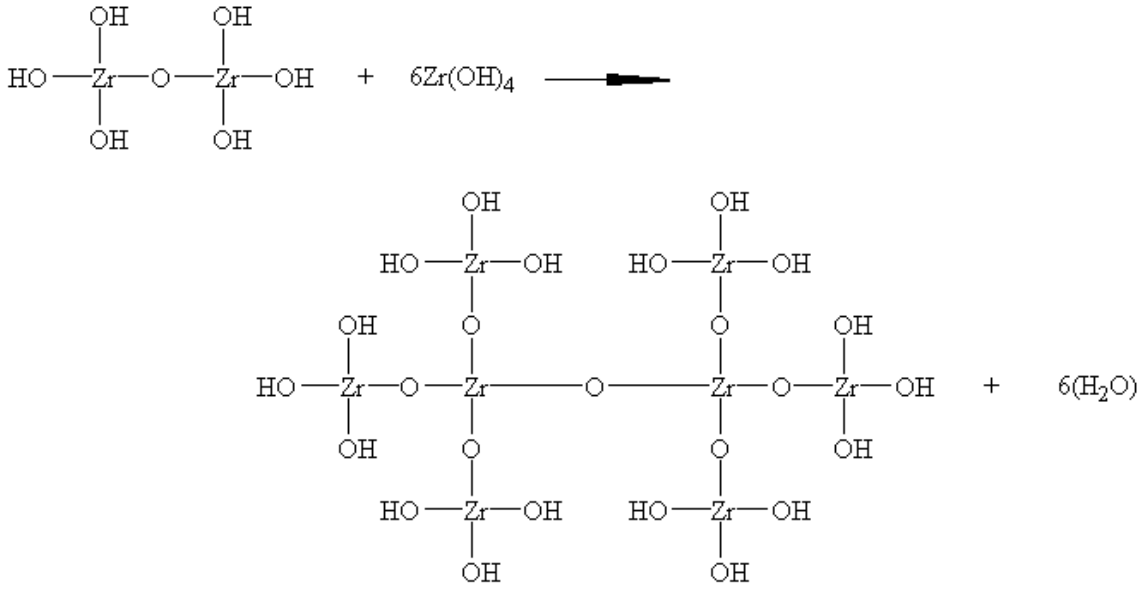

Figure 3.3: Polycondensation reaction.

The hydrolysis and polycondensation reactions initiate at numerous sites within the ETOH + H_2O solution as mixing occurs. When sufficient interconnected Zr–O–Zr bonds are formed in a region, they respond cooperatively as colloidal (submicrometer) particles or a sol. The size of the sol particles and the cross-linking within the particles (i.e., density) depend upon the pH and ratio R, defined as $R = H_2O/Zr(OR)_4$, among other variables.

Step 2: Casting. Since the sol is a low-viscosity liquid, it can be cast into a mold. The mold must be selected to avoid adhesion of the gel.

Step 3: Gelation. With time the colloidal particles and condensed zirconium species link together to become a three-dimensional network. The physical characteristics of the gel network depend greatly upon the size of particles and extent of cross-linking prior to gelation. At gelation, the viscosity increases sharply and a solid object results in the shape of the mold. With appropriate control of the time-dependent change of viscosity of the sol, fibers can be pulled or spun as gelation occurs.

Step 4: Aging. Aging of a gel, also called syneresis, involves maintaining the cast object for a period of time, hours to days, completely immersed in liquid. During aging, polycondensation continues along with localized solution and reprecipitation of the gel network, which increases the thickness of interparticle necks and decreases the porosity.

The strength of the gel thereby increases with aging. An aged gel must develop sufficient strength to resist cracking during drying. This step is especially important for the preparation of bulk samples.

Step 5: Drying. During drying the liquid is removed from the interconnected pore network. Large capillary stresses can develop during drying when the pores are small (<20 nm). These stresses will cause the gels to crack catastrophically unless the drying process is controlled by decreasing the liquid surface energy by addition of surfactants or elimination of very small pores (method 1) by hypercritical evaporation. This process avoids the solid-liquid interface in method 2. Stress is also reduced by obtaining monodisperse pore sizes by controlling the rates of hydrolysis and condensation (method 3). After hypercritical drying in method 1, the aerogel has a very low density and is a very good thermal insulator when sandwiched between glass plates and evacuated [11].

Step 6: Dehydration or Chemical Stabilization. The removal of surface silanol (Zr–OH) bonds from the pore network results in a chemically stable ultraporous solid. Porous gel made in this manner by method 3 is optically transparent with interconnected porosity and has sufficient strength to be used as unique optical components when impregnated with optically active polymers such as fluors, wavelength shifters, dyes, or nonlinear polymers [12].

Step.7: Densification. Heating the porous gel at high temperatures causes densification. The pores are eliminated and the density ultimately becomes equivalent to the obtained for standard methods or equivalent to fused quartz in the case of silica. The densification temperature depends considerably on the dimensions of the pore network, the connectivity of the pores and surface area.

The purity and homogeneity of dense gel made by method 3 are superior to other processing methods. The ability to produce optics with nearly theoretical limits of optical transmission, lower coefficients of thermal expansion, and greater homogeneity, along with net shape casting, represents major advances resulting from sol-gel processing [13].

The general sol-gel process has been briefly described, however, for the synthesis of ZrO_2: Yb^{3+}, Er^{3+} nanophosphors it was necessary the applying of a specific sol-gel derived method. In next section, related aspects of this implementing are reported.

3.2. SYNTHESIS METHOD FOR ZrO_2: Yb^{3+}, Er^{3+} NANOCRYSTALS

In this thesis work, the phosphor under study (ZrO_2:Yb^{3+}, Er^{3+}) has zirconium dioxide as a host matrix and, ytterbium–erbium (combined and separated) as active ions. The process employed to synthesize these nanophosphors approaches overly to the one described previously. The used chemical equation describing molar composition is as follows.

$$a \cdot Yb_2O_3 - b \cdot Er_2O_3 - (100 - a - b) \cdot ZrO_2 \quad (\%\ \text{mol}) \tag{3.1}$$

The required material was calculated to elaborate 1.0 g of each doped nanophosphor for each composition under study.

Substance	Zirconium n-propoxide	ETOH	H_2O	HNO_3	HCl
Molar rate [%]	1	40	4	0.9	0.3

Table 3.1: Used molar ratio for required substances.

3.2.1. Synthesis Procedure

The molar ratio used for sol-gel preparation of nanocrystals is shown in table 3.1. The ZrO_2:Yb^{3+}, Er^{3+} co-doped nanoparticles were obtained with various Yb^{3+} and Er^{3+} concentrations. The samples were obtained using zirconium n-propoxide (ZP) 70% purity, erbium nitrate ($Er(NO)_3)_3 \cdot 5H_2O$) and ytterbium chloride ($YbCl_3 \cdot 6H_2O$) 99.99% purity as precursors. All components were mixed in a solution of ethanol (ETOH), and then hydrochloric acid and nitric acid are added at room temperature applying vigorous stirring.

For a better control of the alcohoxolation process through the removal of protons, the amount of ethanol was calculated to achieve an elevated molar ratio. The solution thus obtained was stirred for 1 h and then CO_2-free distilled water in a molar rate 1:4 was added dropwise to manipulate the gel and oxolation processes. Due to the high reactivity of ZP, strict handling was required of the hydrolysis process to control the homogeneity, avoid the opacity and precipitation. The whole process is shown in figure 3.4.

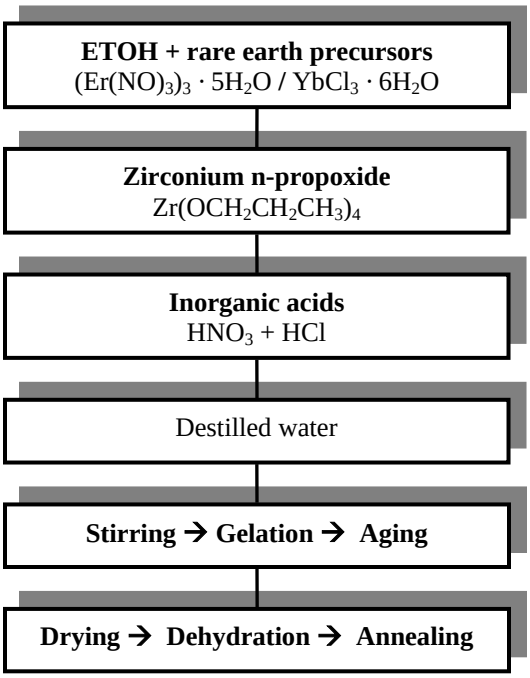

Figure 3.4: Schematic diagram of the synthesis process used for ZrO_2:Yb^{3+}, Er^{3+} nanocrystals sample preparation.

In order to study the influence of the ytterbium and erbium content on the luminescence properties, doped samples were prepared by adding different molar concentrations of Er_2O_3 and Yb_2O_3. The corresponding related molar calculations are shown in table 3.2

	Yb [gr]	Er [gr]	ETOH [ml]	ZP [ml]	HNO3 [ml]	HCL [ml]	H2O [ml]
2%Yb 0.1%Er	0.12056	0.00690	18.05320	3.41345	0.47455	0.18933	0.54829
2%Yb 0.2%Er	0.12033	0.01377	18.00069	3.40353	0.47317	0.18878	0.54669
2%Yb 0.5%Er	0.11966	0.03423	17.84436	3.37397	0.46906	0.18714	0.54194
2%Yb 1%Er	0.11854	0.06782	17.58768	3.32543	0.46232	0.18445	0.53415
2%Yb 2%Er	0.11638	0.13315	17.08838	3.23103	0.44919	0.17922	0.51898
10%Yb 0.1%Er	0.52030	0.00595	14.30870	2.70545	0.37612	0.15006	0.43456
10%Yb 1%Er	0.51276	0.05867	13.96023	2.63956	0.36696	0.14641	0.42398
1%Yb 1%Er	0.06045	0.06916	18.12223	3.42651	0.47637	0.19006	0.55038
3%Yb 1%Er	0.17442	0.06652	17.07356	3.22823	0.44880	0.17906	0.51853
4%Yb 1%Er	0.22819	0.06527	16.57873	3.13466	0.43580	0.17387	0.50351
4%Yb 0%Er	0.06162	0.00000	18.66131	3.52843	0.44880	0.17906	0.56676
2%Yb 0%Er	0.12079	0.00000	18.10591	3.42342	0.47637	0.19006	0.54989
1%Yb 0%Er	0.06162	0.00000	18.66131	3.52843	0.44880	0.17906	0.56676
0%Yb 0.2%Er	0.00000	0.01434	19.12567	3.61623	0.50275	0.20058	0.58086
0%Yb 1%Er	0.00000	0.07057	18.67847	3.53168	0.49099	0.19589	0.56728
0%Yb 2%Er	0.00000	0.13845	18.13859	3.42960	0.47680	0.19023	0.55088

Table 3.2: Calculated quantities required to synthesize samples under study.

All samples were aged at 65 ºC for 15 ~ 18 h and then grinded in an agata mortar to obtain a fine powder. Afterwards the samples were dried at 300 ºC for 2 h, dehydrated (stabilized) at 500 ºC for 2 h and annealed at 1000 ºC for 5 h applying increment ramps of temperature, as shown in figure 3.5. A special oven that supports temperature ramps was used and it required about 13 hours for the complete dried to annealing process. After annealing, powder is grinded again to be ready for characterization.

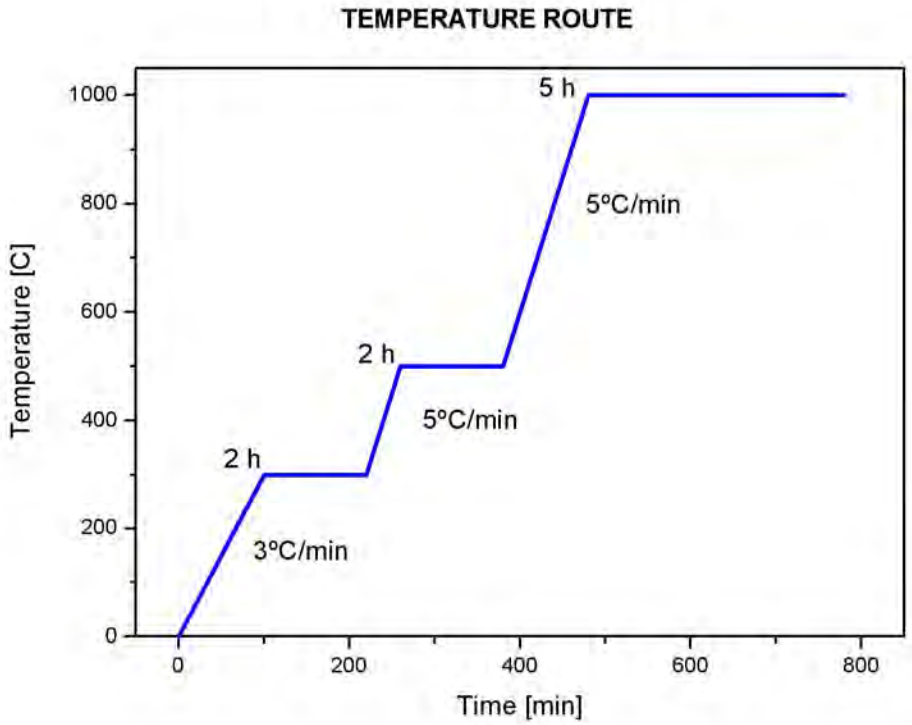

Figure 3.5: Temperature route applied during synthesis of samples.

Once all the samples were synthesized and prepared for subsequent analysis, the structural characterization of these nanocrystals is reported in next section.

3.3. STRUCTURAL CHARACTERIZATION AND MORPHOLOGY

In order to get information about composition, crystalline structure, dimensional and shape properties of the nanocrystals, the considered techniques that were available for the characterization are the following: Attenuated Total Reflectance Fourier–Transform Infra Red spectroscopy (ATR/FTIR), X-Ray Diffraction spectroscopy (XRDS), High Resolution and normal Transmission Electron Microscopy (HR/TEM).

3.3.1. ATR/FTIR

In the mid-infrared, absorption of radiation is related to fundamental vibrations of the chemical bonds. Internal reflection spectrometry provides information related to the presence or absence of specific functional groups, as well as the chemical structure of polymer compounds. Absorption bands are assigned to functional groups, e.g., C=O stretch and C-H bend. Shifts in the frequency of absorption bands and changes in relative band intensities indicate changes in the chemical structure or changes in the environment around the polymer compound. The same analysis of vibrational spectra is applied to characterize the organic fouling layer that may be present on the compound surface. ATR/FTIR

spectrometry can be used to determine changes in surface chemistry after special chemical or physical treatments are applied, e.g., exposure to surfactants or chlorine and temperature annealing. ATR/FTIR spectrometry can also be used to identify unique features on the compound after chemical surface modification. The IR analysis performed on our nanocrystals and described in this section is intended to know the remaining residuals after annealing in the nanocrystals surface; it is a qualitative analysis in order to find possible agents affecting luminescent properties.

ATR/FTIR spectroscopy is based on the evanescent wave phenomenon, where a beam of electromagnetic radiation is internally reflected. The polymer coating on the internal reflection element (IRE), concentrates the analyte in the evanescent wave region, and an absorption spectrum of the analyte is obtained. The increase in analyte absorption is monitored as a function of diffusion time. FT-IR spectra were obtained using a Perkin Elmer Instruments Spectrophotometer, Spectrum BX FT-IR System at 25 ºC and 30% of relative humidity. The wave number ranges from 400 to 4000 cm^{-1} and with 20 scans.

The IR transmittance spectra are shown on figures 3.6, 3.7 and 3.8. The absorption peaks are numbered and the related functional groups are indicated on table 3.3. According to the table and spectra, there are small quantities of compounds related to the host as metal alkoxides or metal–OH bonds, CO_3 complexes and C, H, O, N based organics. During the sol-gel process water, zirconium n-propoxide and inorganic acids were used. Therefore, residuals of chemical reactions appear in the solution because of hydrolysis. Heating using temperature ramps is considered to remove these compounds; however in some way such compounds still remain. The most part of contaminant is ethyl esters $–O-CH_2CH_3$ produced by the large quantity of ethanol used. Free OH and CO_2 is also present in less quantity and may be produce during the reaction and also introduced by the exposition to ambient condition.

Residuals are very similar on both kinds of one ion doped samples; however ytterbium–erbium doped samples presented a noticeable reduction on residuals. Results reveal that samples doped just with one ion have more quantity residuals than samples doped with both ions. Even though these residuals are reduced changing the concentration these ones are not as low as two-ion doped samples. It is well-known that the residuals components, especially OH and CO_2, induce non-radiative relaxation by resonance coupling; fortunately its concentration apparently is low. At this stage we do not know the influence in the luminescence properties of other observed components. It is not possible to observe a systematic behavior of the resonance bands as function of type and concentration of ions. Thus, it is not possible to conclude if the presence of one specific ion reduces contaminants. Apparently, it is the synthesis process that retains such residuals. Because contaminants play an important role in the luminescence efficiency, it is considered that this behavior requires special attention and an exhaustive study is underway. Recent results obtained in our group show that the use of surfactants reduces contaminants and enhance the luminescence [14,15]

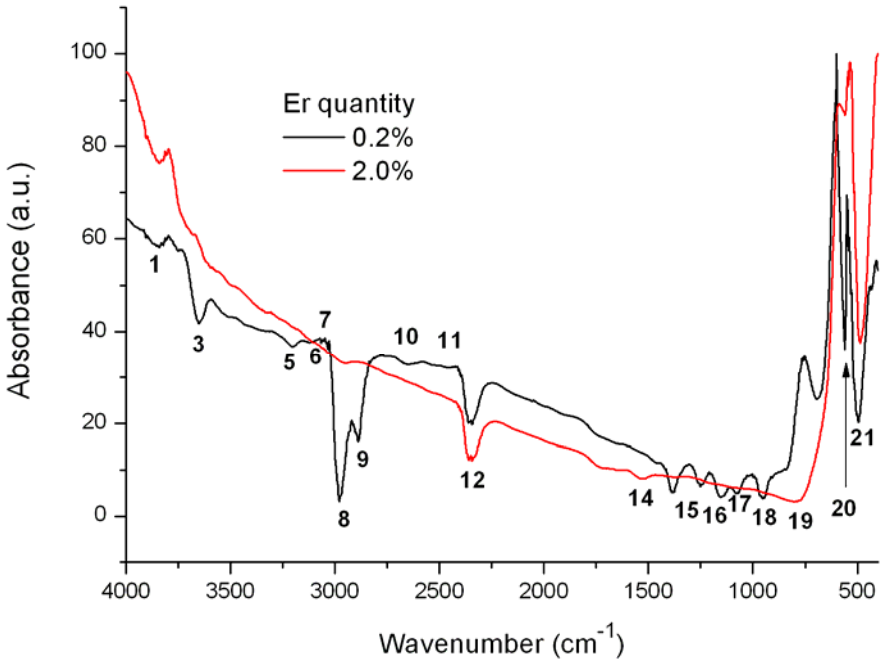

Figure 3.6: IR absorption spectra of erbium doped samples.

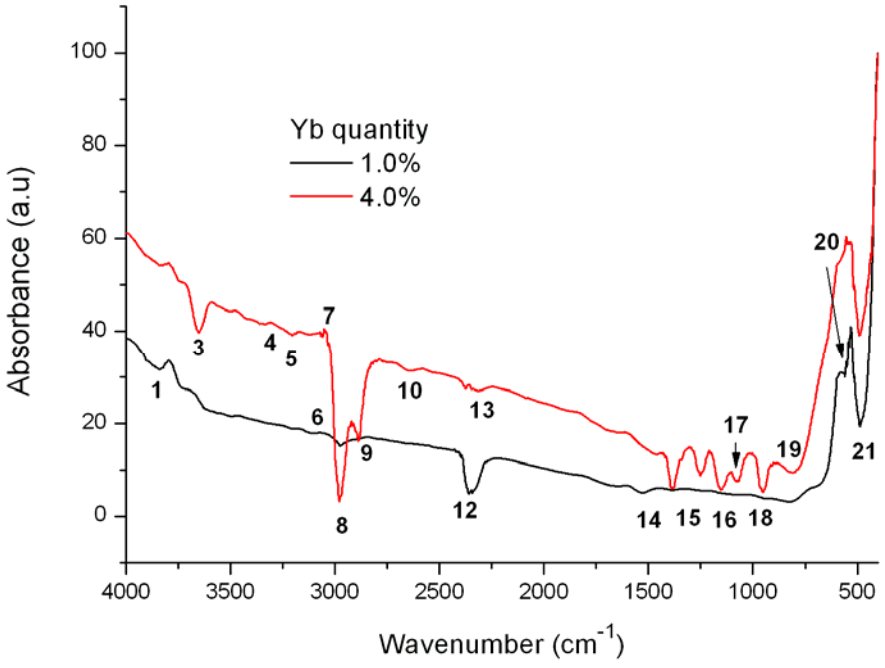

Figure 3.7: IR absorption spectra of ytterbium doped samples.

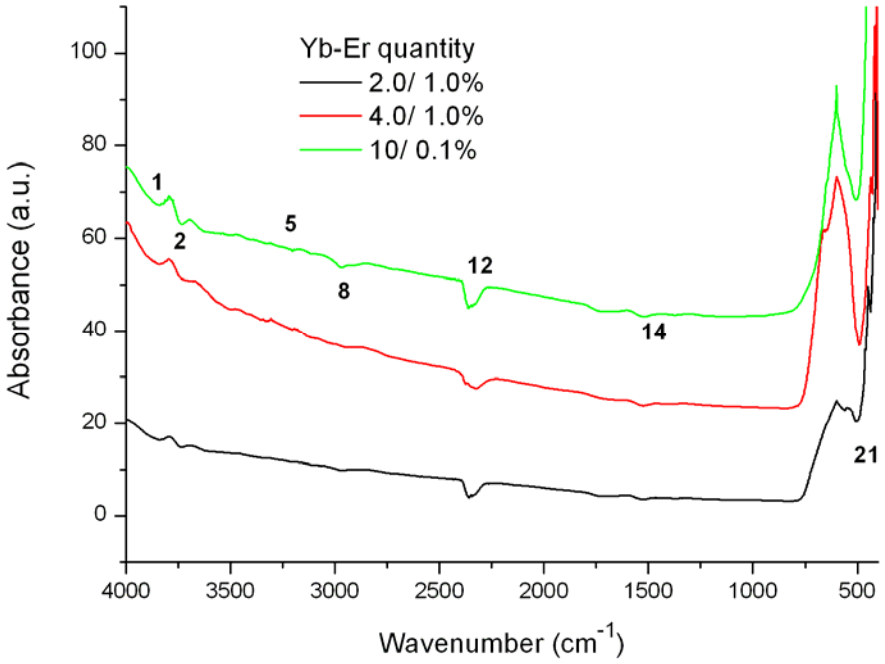

Figure 3.8: IR absorption spectra of ytterbium–erbium doped samples.

Reference number	Peak [cm-1]	Er	Yb	Yb-Er	Possible associated compound
1	**3840**	**X**	**X**	**X**	Hydrides, O–H stretching, Metal bonds M–OH
2	**3728**			**X**	Amino acids hydroalides
3	**3652**	**X**	**X**		Free O–H
4	**3332**		**X**		Primary amides (asymmetric N–H stretching)
5	**3204**	**X**	**X**	**X**	Hydrogen bonded oximes, Primary amides (sym. N–H stretching)
6	**3120**	**X**	**X**		Free amino acids NH_3
7	**3032**	**X**			C–H
8	**2980**	**X**	**X**	**X**	Ethyl esters –O–CH_2CH_3
9	**2890**	**X**	**X**		C–H, CH_3 stretching absorption, –O–CH_3 stretching
10	**2648**	**X**	**X**		Free amino acids (C–H stretching)
11	**2460**	**X**			O–H Hydrides, Free amino acids
12	**2360**	**X**	**X**	**X**	Carbon dioxide
13	**2314**		**X**		Amino acid
14	**1526**	**X**	**X**	**X**	Amino acid (II band)
15	**1388**	**X**	**X**		CO_3 complexes
16	**1154**	**X**	**X**		$=C(CH_3)_2$ rocking vibration
17	**1082**	**X**	**X**		Saturated primary alcohol CH_2–OH
18	**954**	**X**	**X**		ClO_3
19	**826**	**X**	**X**		Metal–OH, CO_3 complexes
20	**560**	**X**	**X**		Rare earth oxides
21	**510-490**	**X**	**X**	**X**	Metal alkoxides M–O stretching, M–O absorption

Table 3.3: Functional groups associated to found peaks in doped samples.

3.3.2. XRDS

Also known as XRD crystallography; in it, X-rays are diffracted through a crystalline material, revealing the interatomic spacing, atomic identities, and positions of atoms within the crystal. Diffraction is the most fundamental means of determining structure of minerals and other materials, and it is especially useful to characterize environmental samples. Conventionally, XRD has several limitations as the fact that it is limited to crystalline materials (since amorphous materials do not diffract), it is time-consuming and uses a relative large volume of sample. However, synchrotron-based XRD is useful to circumvent these limitations. Amorphous materials and thin films can also be analyzed thanks in part to the instrumental configuration of these instruments. Finally, XRD can be collected over a large range of angles, impossible with conventional instruments and invaluable when performing Rietveld refinements, which are used to determine the unit cell parameters and site occupancy for a powder XRD pattern given a crystal lattice.

The crystalline structure of bulk ZrO_2 depends on the annealing temperature (T_a) and shows three stable crystalline phases: monoclinic (*m*) structure at T_a < 1170 ºC, tetragonal (*t*) structure between 1170 and 2370 ºC and cubic (*c*) structure at T_a > 2370 ºC. Both optical and mechanical properties are function of the crystalline phase composition. Recently, the metastable *t* phase has been synthesized at 500 ºC by using the sol-gel technique, but it was transformed to *m* phase as annealing temperature was increased. Furthermore, it is demonstrated that it is possible to stabilize the metastable tetragonal structure of ZrO_2 up to 1000 ºC by doping with Sm^{3+} and Tb^{3+} ions [16]. The phase composition and average crystallite sizes are function of the ion concentration. This is due to the fact that stability and transformability of tetragonal phase is related directly with the crystallite size. The XRD patterns of undoped and Er^{3+} doped ZrO_2 nanocrystals are shown in figure 3.9. The diffraction pattern of undoped ZrO_2 nanocrystals is dominated for the monoclinic structure. The characteristic peaks of this structure are $(1,1,0)_m$, $(-1,1,1)_m$ and $(1,1,1)_m$ according to the standard JCPDS 37-1484 and are centered at 24.55º, 28.40º and 31.40º respectively. The XRD pattern is similar than the presented for 0.2 mol% of Er^{3+} doped sample. Here, and also for undoped sample, small peak, $(1,0,1)_t$, centered at 30.33º is observed. Such peak is characteristic of tetragonal phase according to the standard JCPDS 37-1413. The phase composition of samples doped with different concentrations of Yb^{3+}, Er^{3+} ions was estimated by using the equation proposed by Garvie [17]:

$$C_m = \frac{I_m(-1,1,1) + I_m(1,1,1)}{I_m(-1,1,1) + I_m(1,1,1) + I_t(1,0,1)}$$

$$C_t = 1 - C_m \tag{3.2}$$

where *m* and *t* refer to the monoclinic and tetragonal phases of zirconium and *I* stand for the integrated intensity of each peak. According to this, the estimated content of tetragonal phase in undoped samples was only 3 wt% while for 0.2 mol% Er doped sample was 4 wt%. The phase composition of nanophosphor changes with the increase of Er^{3+} ion.

For 1 mol% of Er^{3+} the tetragonal content increase to 6 wt% but for 2 mol% tetragonal content was 17 wt%. Notice that in this last case, the intensity of $(1,0,1)_t$ diffraction peak is almost similar to the intensity of $(1,1,1)_m$ diffraction peak. It has been reported up to 60 wt% of tetragonal for 3.5–4 mol% of Er^{3+} [18].

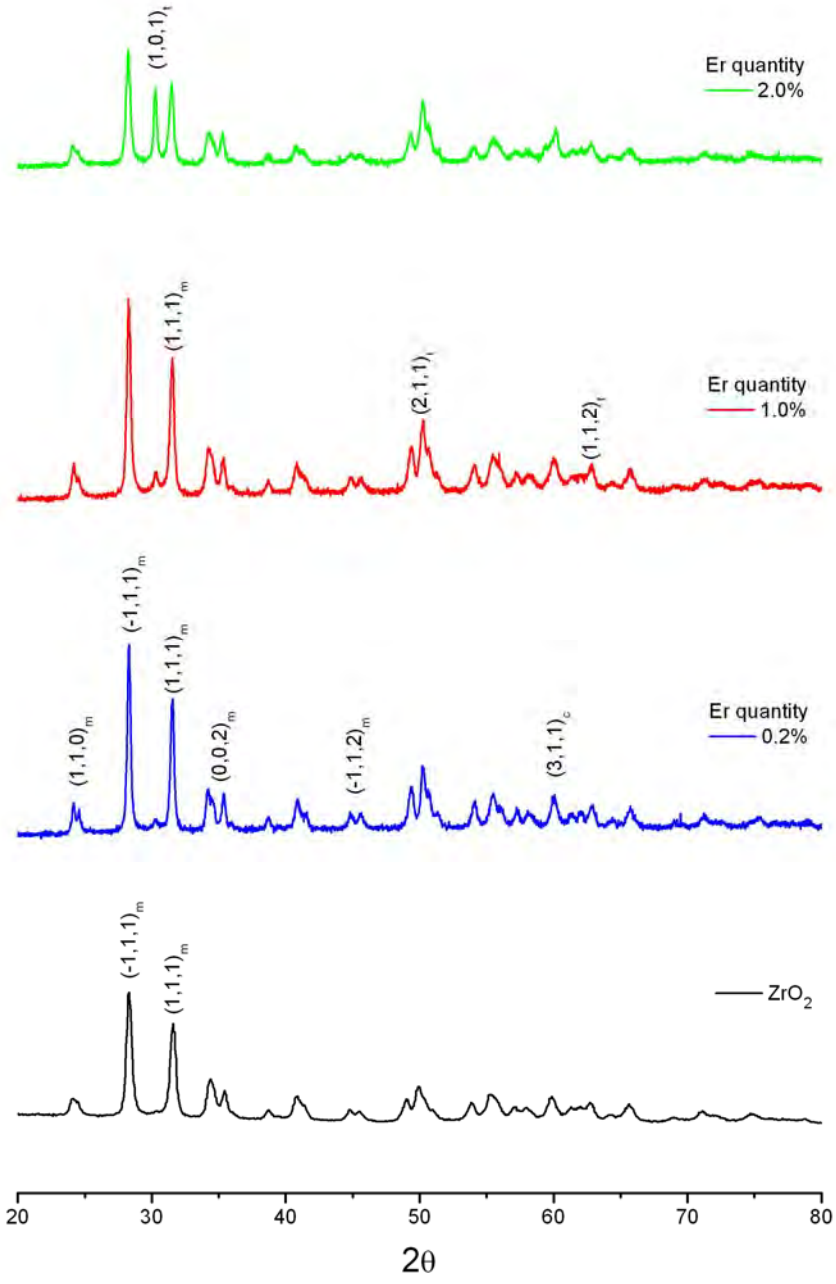

Figure 3.9: X-ray diffraction patterns of Er^{3+} doped samples.

Different rare earth ion has different influence on the phase stabilization as has been reported by our group [16]. The figure 3.10a shows the XRD patterns for Yb^{3+} doped ZrO_2 nanocrystals. The estimated tetragonal content for 2 mol% was 60 wt% and 100 wt% for 4 mol% doped samples. Notice that for 8 mol% of Yb^{3+} cubic crystalline phase is completely stabilized. No tetragonal content was observed for this concentration as is shown in figure 3.10b. Crystalline phase is confirmed analysing the close up of $(0,1,1)_t$ diffraction peak, for tetragonal is a double peak centred at 34.77° and 35.21°, while for cubic phase is just a single peak centred at 35°. These experimental results show that Yb^{3+} ion is dominant to stabilize crystalline phase.

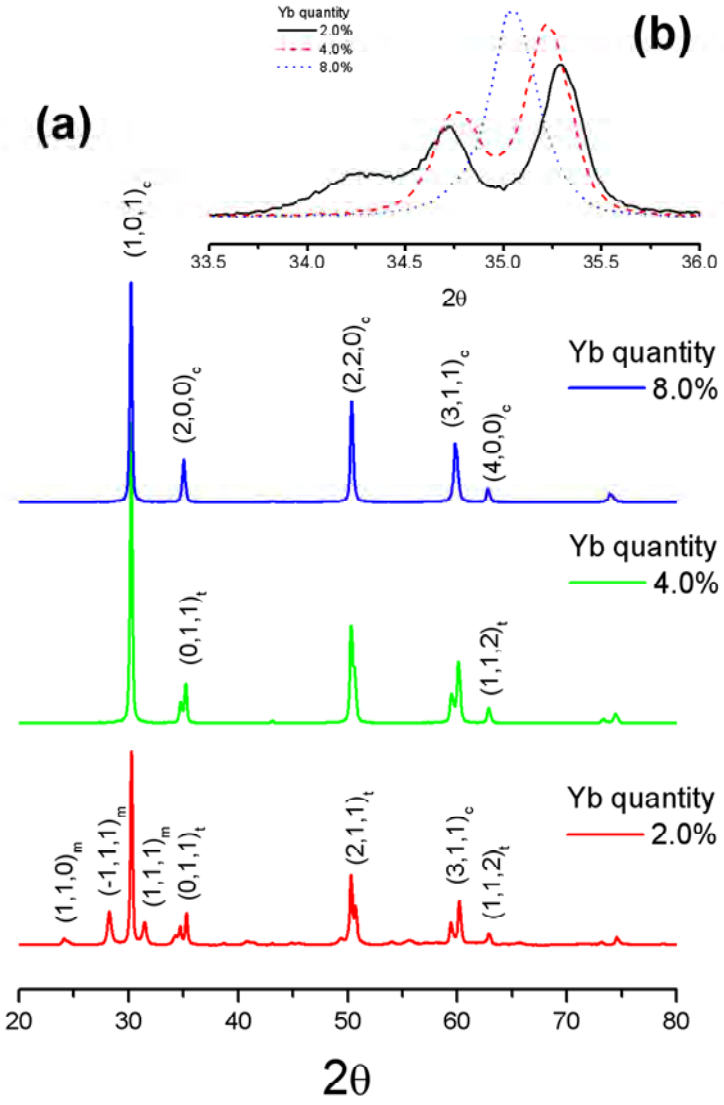

Figure 3.10: X-ray diffraction patterns of Yb^{3+} doped samples (a). The inset (b) shows a detailed of the characteristic double peak for tetragonal and single peak for cubic phase for 8 mol% doped sample.

The crystalline phase composition for ZrO_2:Yb^{3+}, Er^{3+} nanophosphors is a mixture of monoclinic, tetragonal and cubic phases as concentration increases, of course dominated by the Yb^{3+} ion content. The XRD patterns are shown in figure 3.11. Pure tetragonal was obtained for ZrO_2:Yb^{3+}(2%), Er^{3+}(1%) sample and 33 wt% cubic phase was obtained for ZrO_2:Yb^{3+}(4%), Er^{3+}(1%) sample. For higher concentration pure cubic phase was observed. That is to say, the stabilization of a given crystalline phase of ZrO_2 nanocrystals is Yb^{3+}–Er^{3+} concentration dependent. In ZrO_2:Yb^{3+}, Er^{3+} doped samples there is a noticeable small width of the diffraction peaks that indicates a uniform distribution of the average crystallite size. As discussed in Chapter 2, the average crystallite sizes can be estimated by using the Scherrer's equation [19]:

$$D = \frac{(0.9\lambda)}{\beta \cos(\theta)} \tag{3.3}$$

where λ stand for the X–ray wavelength, β is the corrected half-width of the strongest diffraction peak and θ is the diffraction angle. The estimated average crystallite size for Er^{3+} doped nanocrystals ranges from 30 to 50 nm for monoclinic phase. For Yb^{3+} doped samples, apparently the average crystallite size increases, for monoclinic the average is ~ 60 nm and for tetragonal ~ 90 nm. For ZrO_2:Yb^{3+}, Er^{3+} doped samples the average ranges from 50 to 70 nm for tetragonal phase, that is the dominant phase for most of the samples under study.

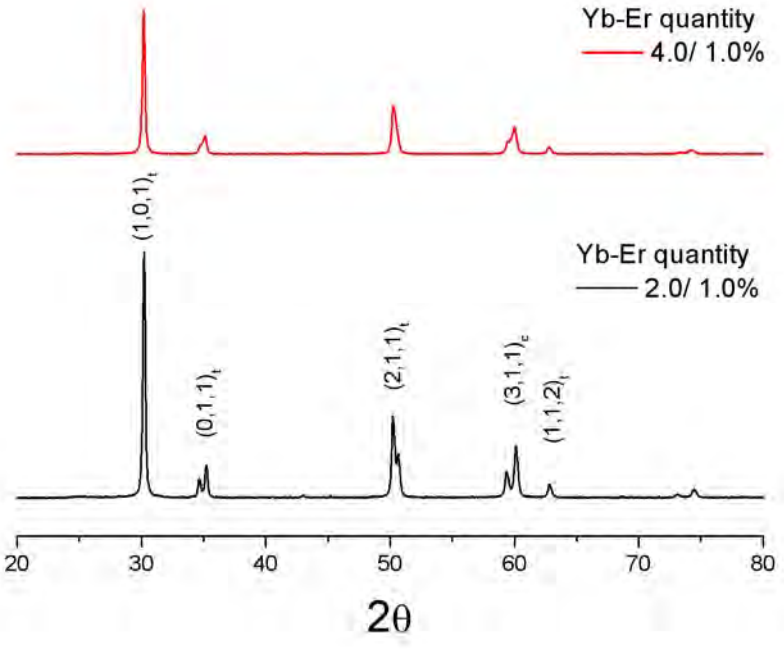

Figure 3.11: X-ray diffraction patterns of Yb^{3+}–Er^{3+} doped samples.

The phase composition, average crystallite size and lattice parameters for tetragonal, monoclinic and cubic structure of undoped and doped ZrO_2 nanocrystals were obtained by Rietveld method that corroborate the previous estimation. Rietveld method consist in simulate a theoretical curve of the XRD pattern fitting the experimental curve with the minimum error. Thus this process gives us very precise information about all parameters of all crystalline structures presented. The calculated data are presented in table 3.6 showing that our initial estimation was in good agreement. For low concentrations of Er^{3+} doped samples the large crystallite size of monoclinic at long annealing time is the result of a faster nucleation rate resulting in a crystal grows. Furthermore, the small crystallite size of tetragonal is the result of transformation from tetragonal to monoclinic after a critical size [16], remaining only tetragonal crystallite below such critical size. Notice that no segregation of dopant was observed.

(mol%)	Phase (weight%)	Cell Parameters				Cell Volume ($Å^3$)	Crystal Size nm
		a_o (Å)	b_o (Å)	c_o (Å)	β		
ZrO_2	Tetragonal (3)	3.585	3.585	5.210		66.96	17.1
	Monoclinic (97)	5.147	5.198	5.324	99.000	142.43	48.8
Er 0.2	Tetragonal (4.3)	3.600	3.600	5.182		67.16	17.5
	Monoclinic (95.7)	5.151	5.203	5.323	99.10	142.67	46.3
1	Tetragonal (6.5)	3.598	3.598	5.186		67.13	18.4
	Monoclinic (93.5)	5.154	5.205	5.317	99.08	142.64	35.6
2	Tetragonal (16.9)	3.600	3.600	5.180		67.13	47.7
	Monoclinic (83.1)	5.156	5.209	5.314	99.06	142.72	30.0
Yb 1.0	Tetragonal (7.2)	3.599	3.599	5.179		67.07	29.15
	Monoclinic (92.8)	5.155	5.207	5.312	99.09	142.60	60.3
2.0	Tetragonal (60.7)	3.601	3.601	5.175		67.10	92.9
	Monoclinic (39.3)	5.159	5.209	5.313	99.00	142.81	52.1
4.0	Tetragonal (100)	3.605	3.605	5.165		67.13	92.2
8.0	Cubic (100)	5.1257	5.1257	5.1257		134.67	53.6
Yb/Er 2/1	Tetragonal (100)	3.602	3.602	5.172		67.10	77.8
4/1	Tetragonal (67)	3.607	3.607	5.160		67.14	49.1
	Cubic (33)	5.124	5.124	5.124		134.51	79.9

Table 3.6: Lattice parameter, crystallite size and crystalline phase composition obtained from X–ray refinement.

Considering cell parameters for undoped and doped ZrO_2, table shows that cell parameters change with the type of ion and with concentration; such changes are produced by the different ion size of different dopants and the cation. Thus, such changes suggest that dopant ions are substituted on Zr cation position. Because cation (Zr^{4+}) and dopant in (RE^{3+}) differ in charge, substitution induces distortion of the crystalline network. This mean that even the most symmetrical structure that is cubic followed by tetragonal present a high level of asymmetry that is favorable for luminescence properties. Such asymmetry is also enhanced by surface defect because of high surface-volume ratio that characterizes nanostructures.

3.3.3. TEM AND HRTEM

Electron Microscopes use a beam of highly energetic electrons to examine objects on a very fine scale. Interactions that occur inside the irradiated sample, affects the electron beam. These interactions and effects are detected and transformed into an image. This examination can yield the following information:

- Topography. Surface features of an object, its texture.
- Morphology. Shape and size of the particles making up the object.
- Crystallography. How the atoms are arranged in the object.

The average particle size was changed with concentration of Yb^{3+}–Er^{3+} ions as can be observed by TEM images. The particle size distribution and average size are presented on figure 3.12. Considering that average particle size was obtained measuring both tetragonal and monoclinic particles, results are higher than the crystallite size obtained by XRD due to the fact that particles are formed by several crystallites but are in agreement with tendency. It is also important to mention that in order to have a more precise average crystallite size it is necessary to consider a much more large number of images and then a larger number of nanocrystals to be measured.

The characteristic morphology of representative samples is shown in the image displayed in figure 3.13. For the ZrO_2:Er^{3+}(2%) sample the phase is mainly monoclinic, the ZrO_2:Yb^{3+}(2%) and ZrO_2: Yb^{3+}(4%), Er^{3+}(1%) samples are principally tetragonal but for ZrO_2:Yb^{3+}(4%) sample the phase is tetragonal entirely. Notice that crystallites present well defined faces suggesting that in general are faceted and that no agglomeration is presented. Thus, the structural characterization shows that the particle size is the result of a combination of both annealing time and dopant concentration.

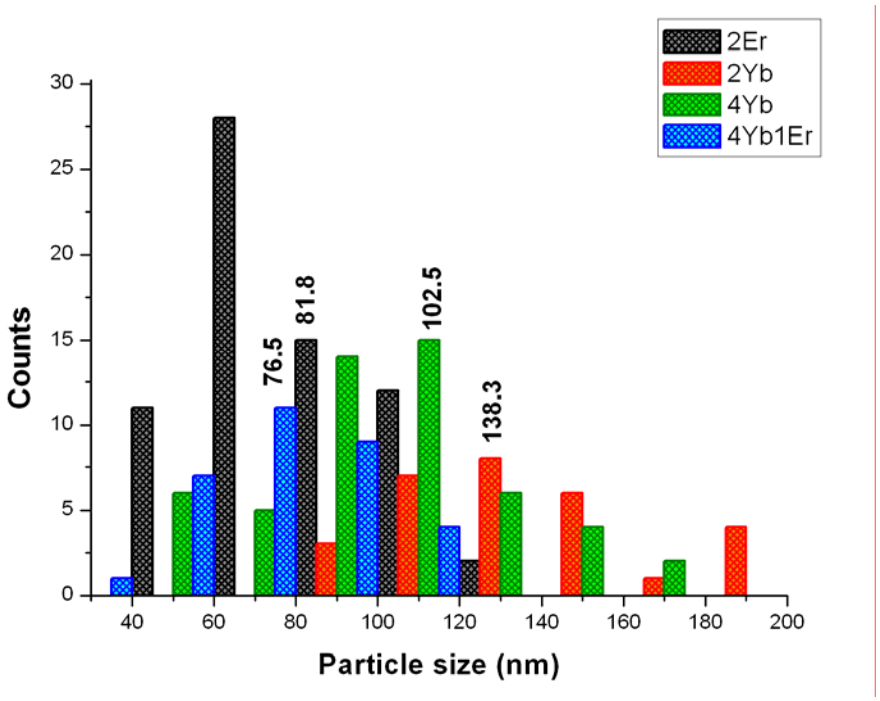

Figure 3.12: Particle size distribution and average size (labeled).

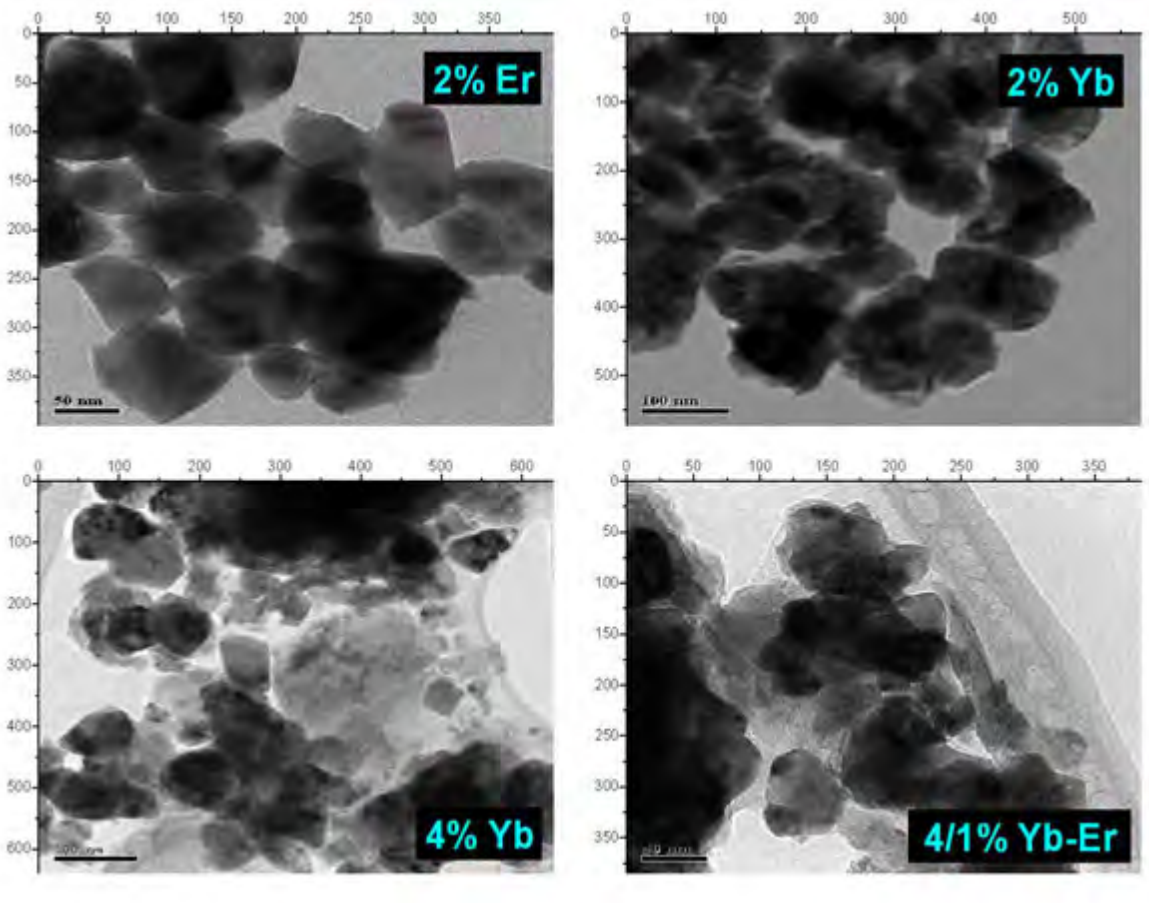

Figure 3.13: TEM micrograph of representative samples under study.

Crystalline structure was confirmed with HRTEM. The figure 3.14 shows the HRTEM and their Fourier Transform pattern (FFT), which were analyzed to identify the crystalline structure and interplanar distances for ZrO_2:Yb^{3+}(4%), Er^{3+}(1%) doped sample. Its interplanar distances obtained were 0.3009 nm, 0.2930 nm and 0.2598 nm corresponding to (1,-1,1), (2,0,0) and (1,1,1) planes respectively of the cubic phase in [0,1,-1] direction, while the interplanar distances were 0.2659 nm, 0.2946 nm and 0.2925 nm corresponding to (-1,0,1), (0,0,2) and (1,0,1) planes of the tetragonal phase in the [0,1,0] direction. Well faceted individuals nanocrystals were observed although agglomeration was present as consequence of the high annealing temperature. HRTEM confirm that the Yb^{3+} ion content not affects the particle size but affects the crystalline structure [20].

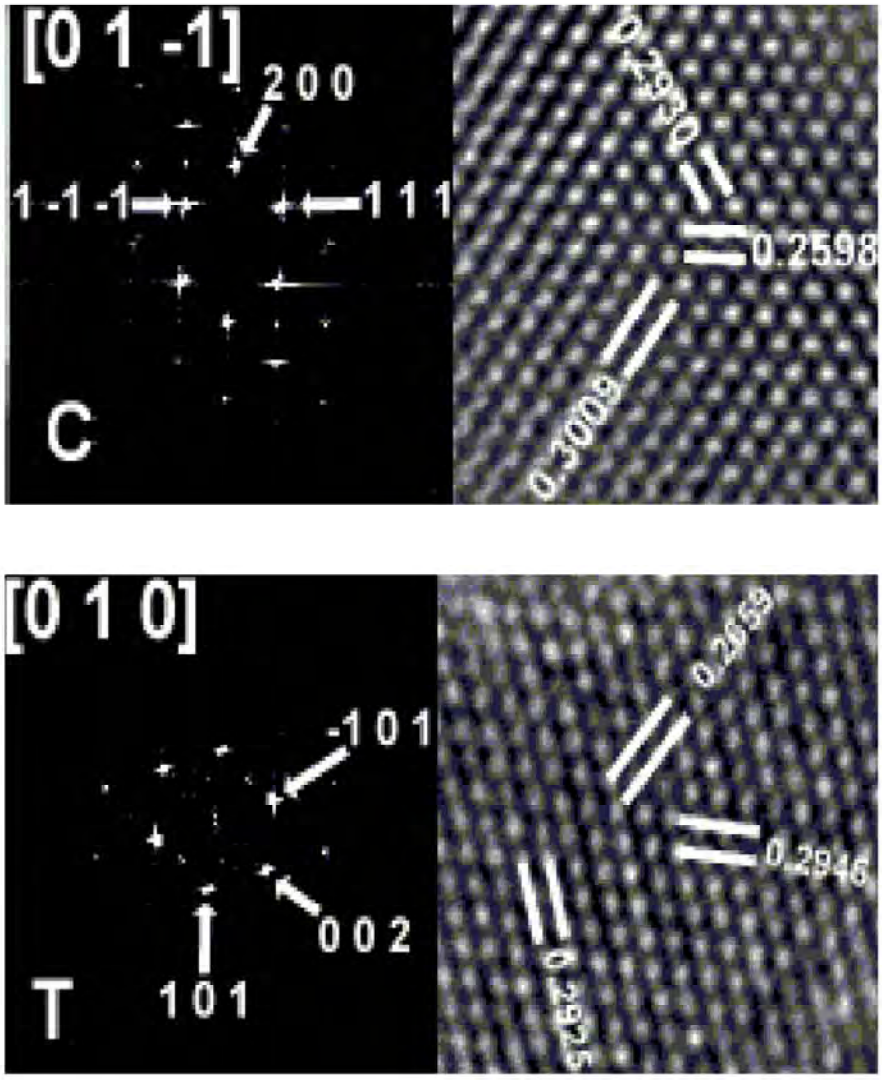

Figure 3.14: HRTEM images and their Fourier Transform patterns of 4.0/1.0% sample prepared.

REFERENCES AND NOTES

[1] Hench, L. L.; Ulrich, D. R. *Ultrastructure Processing of Ceramics Glasses and Composites*. Eds. Wiley. New York. 1984

[2] Davis, J. T.; Rideal, E. K. *Interfacial Phenomena*. Academic Press. New York. 1963

[3] As discussed by Flory, P. J. in Chapter IX of *Principles of Polymer Chemistry*. Cornell University Press. Ithaca, New York. 1953

[4] Fricke, J.; Capo. *Ultrastrucure Processing of Advanced Ceramics*. Mackenzie, J. D.; Ulrich, D. R. Eds. Wiley. New York. 1988

[5] West, J. K.; Nicles, R.; LaTorre, G. *Better Ceramics Through Chemistry III*. Brinker, C. J.; Clark, D. E.; Ulrich, D. R. Eds. Materials Research Society. Pittsburgh, PA. 1968. Vol. 121, p. 129

[6] Wilson, M. J. R. *Drying Kinetics of Pure Silica Xerogels*. Masters Theses. University of Florida, Gainesville, FL. 1989

[7] Hench, L. L.; Vasconcelos, W. *Structure Properties Relations in Gel Silica and Gel Glass Monoliths*. Ann. Rev. Mater. Sci.

[8] Klein, L. C.; Garvey, G. J. In *Ultrastructure Processing of Ceramics, Glasses and Composites*. Hench, L. L.; Ulrich, D. R. Eds. Wiley. New York. 1984; p 88

[9] Hench, L. L.; West, J. K. The Sol - Gel Process. *Chem. Rev*. **90**. 33-72 (1990)

[10] As discussed in detail by Iler, R. K. in *The Chemistry of Silica*. Wiley. New York. 1979

[11] Yoldas, B. E. *Bull. Am. Ceram. Soc*. **54**, 286 (1975)

[12] Hench, L. L.; Wang, S. H.; Nogues, J. L. In *Multifunctional Materials*. **878**, p 76 (1988) Gunshor, R. L. Ed. SPIE. Bellingham, WA.

[13] Hench, L. L.; Ulrich, D. R. *Science of Ceramic Chemical Processing*. Eds. Wiley. New York. 1986

[14] T. López-Luke, E. De la Rosa, D. Solís, P. Salas, C. Angeles-Chavez, A. Montoya, L.A. Díaz-Torres, S. Bribiesca. *Effect of the CTAB concentration on the upconversion emission of ZrO_2:Er^{3+} nanocrystals*. Opt. Mat. In press (2006)

[15] T. López-Luke, E. De la Rosa, P. Salas, C. Angeles, A. Montoya, L.A. Díaz-Torres. *Study of the annealing time and temperature with different CTAB concentrations on the up-conversion emission of ZrO_2:Er^{3+} nanocrystals*. To be submitted

[16] W. Córdova-Martínez, E. De la Rosa-Cruz, L.A. Díaz-Torres, P. Salas, A. Montoya, M. Avendaño, R. A. Rodríguez, O. Barbosa-García. *Nanocrystalline tetragonal zirconium oxide stabilization at low temperatures by using rare earth ions: Sm^{3+} and Tb^{3+}*. Opt. Mat. **20**, 263-271 (2002)

[17] R. C. Garvie, P. S. Nicholson. *J. Am. Ceram. Soc.* ***55***, 303 (1972)

[18] E. De la Rosa-Cruz, L. A. Díaz-Torres, R. A. Rodríguez-Rojas, M. A. Meneses-Nava, O. Barbosa-García. *Luminescence and visible upconversion in nanocrystalline ZrO_2:Er^{3+}*. Appl. Phys. Lett. **83**, 4903 (2003)

[19] Cullity, B. D. and Stock, S. R. *Elements of X-ray Diffraction.* 3rd edition. Prentice Hall. Upper Saddke River. NJ, 2001

[20] E. De la Rosa, D. Solís, L. A. Diaz-Torres, P. Salas, C. Angeles-Chavez, O. Meza. *Blue-Green emission in ZrO2:Yb^{3+} nanocrystals*. Submitted for publication (2006)

Chapter 4

Luminescence Properties of $ZrO_2:Yb^{3+}$, Er^{3+} Nanocrystals

4.1. INTRODUCTION

One of the most important non-radiative processes that every material shows is the multiphonon relaxation by the vibration bands of the system. When the vibration frequency is increased the non-radiative decay rate increases that in turn will reduce the quantum efficiency of the luminescent processes [1]. The host is desired to possess a minimal absorption coefficient within the wavelength range of interest, ultrafast response times, a capability to have high rare-earth concentrations, and high optical damage threshold [2]. Zirconium oxide has low phonon energy of about 470 cm^{-1} that is very small compared to that of other hosts such as ZnO or Y_2O_3. This low phonon energy opens up the possibility of higher efficient luminescence of active ions incorporated into the matrix [1]. Also it has a high refractive index of about 2.1 and is chemically and thermally stable [3, 4-6].Considerable amount of studies has been reported on the physical properties of ZrO_2 whereas few research works have been done on the luminescence properties of this material [1]. Recently there has been increasing interest in the application of nanoparticles to photonic systems because of their enhanced luminescent properties, which in turn are due to their small size [7-9].

The excellent optical, mechanical, electrical, chemical and photochemical properties of this material made it suitable for different applications such as, interferometric filter [10], coating [11], catalysis [12] and sensors [13]. Based on its thermoluminescence (TL) properties, it was proposed as a dosimeter for ionizing radiation. Further, it has been shown that the TL response and sensitivity of ZrO_2 depend on the crystalline structure, being centered at 130º for monoclinic and 400º for tetragonal structure [14]. It also has been shown that zirconium oxide shows a broad spectral response under UV irradiation. Such range agrees with the range where erythema occurs. That makes this nanocrystal feasible for solar protection and UV doses radiation measurements.

Thus combining the properties of rare-hearth ions, the properties of nanoparticles, and the good qualities of ZrO_2, the study of the upconversion emission in zirconium oxide nanoparticles is worthy of attention [2]. Electrons confinement effect is not expected due to the localization of electrons in atomic orbitals of active ions. However, excitation dynamics is influenced by the nanoscopic interaction and has been reported a dependence of the luminescence efficiency on particle size [15, 16]. In this section, the luminescence properties of the prepared samples are described. The description is divided for each type of doped nanocrystals; the absorption spectra, decay time, infrared and upconverted emissions are taken into account, although, red emission enhancement is particularly considered.

One of the luminescent properties that were analyzed was the fluorescence. The possibility of comparing intensities between samples was a desirable option; therefore, samples were pounded and placed in 1 mm capillary tubes. This guaranteed the exposed volume of each material was not unchanged during the acquisition of data. Also it was necessary to develop and making of a special mounting for this kind of tubes. The implementation for acquire photoluminescence measurements is shown in figure 4.1. The photoluminescence (PL) characterization was performed using a CW semiconductor laser diode as a pump source centered at 967 nm with an output power of 430 mW. The

fluorescence emission was analyzed with a monochromator Acton Pro 500i and a R955 photomultiplier tube (Hamamatsu) for visible and R950 for NIR, connected to a mode-locking amplifier SR360 (Stanford). The system was controlled with a PC where emission spectra were obtained. Fluorescence lifetime was measured using an SR540 chopper (Stanford), the monocromator and photomultiplier connected to a Le Croy digital Oscilloscope. All measurements were done at room temperature. Special care was taken to maintain the alignment of the set up in order to compare the intensity of the upconverted signal between different characterized samples. The 1.55 μm emission was recorded using an Acton Research modular 2300 spectrofluorometer and a PIN photodiode. All measurements were performed at room temperature.

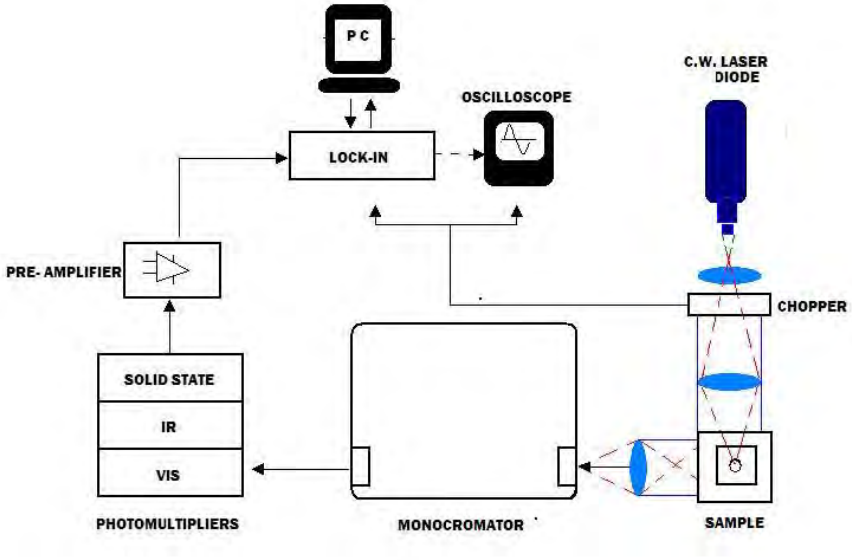

Figure 4.1: Schematic diagram of the PL implementation.

4.2. ABSORPTION SPECTRA

4.2.1. Absorption spectra of ZrO_2:Er^{3+} nanocrystals

The absorption bands of ZrO_2:Er^{3+} nanophosphor (figure 4.2) show the characteristic bands of Er^{3+} ion in addition to the absorption band of the host [1]. The absorption spectra profile of Er^{3+} ion is not very sensitive to the local lattice symmetry of the host. It is also worth to comment that incorporation of increasing amounts of Er^{3+} in both monoclinic and tetragonal ZrO_2 lattices affects the UV absorption edge, which shifts towards lower wavelengths. As the Er^{3+} concentration is added, the coordination around the Er^{3+} ions changes, inducing slight deviations in the positions of the oxygen ions from their lattice points in the monoclinic and tetragonal unitary cells. This short range disorder could explain the slight and the increasing broadening [2]. The band centered at 970 nm presents

small intensity compared to others bands; as a result, excitation energy from pumping is limited due to reduced absorption at this band.

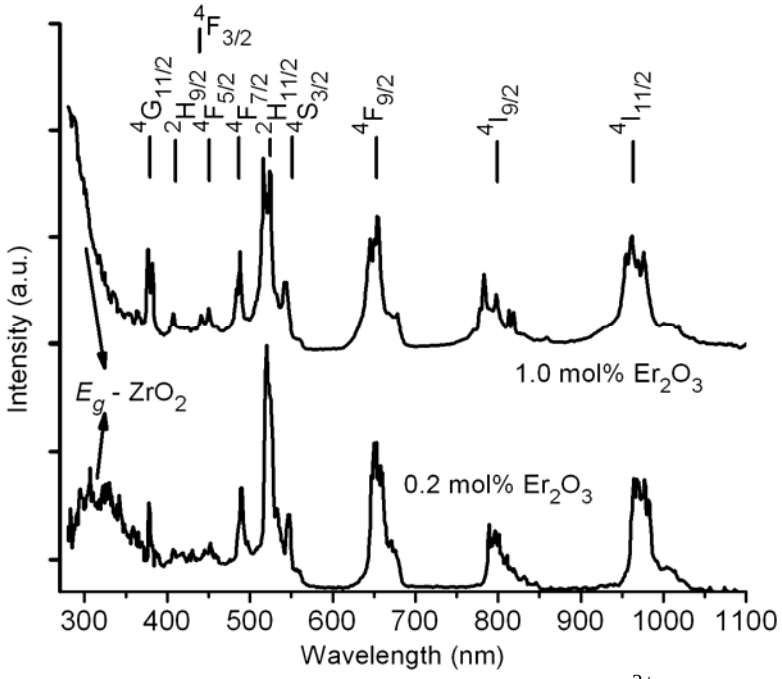

Figure 4.2: Absorption spectra of ZrO_2:Er^{3+}.

Co-doping can increase the efficiency of the upconversion process and in some cases can induce upconversion where as it is not possible in the single ion [17]. A number of well established mechanisms for rare-earth ions are known to populate high energy excited states but all have the presence of an intermediate level that possesses a long lifetime that enables a significant excited state population [18].

In order to increment absorbed energy, co-doping with Yb^{3+} ions is proposed since they present a broad and more intense absorption at this position and due to the possibility to transfer their absorbed energy to Er^{3+} ions. Several studies on Er^{3+} ion reveal high efficiency around 550 and 600 nm under 800 and 980 nm excitations [19,20]. Materials doped with Er^{3+} ions and sensitized with Yb^{3+} ions have been widely studied because Er^{3+} ions have energy levels capable of infrared pumping that closely match the region of the 980 nm peak wavelength of Yb^{3+} absorption [22]. More important, the excited estate of the Yb^{3+} ion has a much higher absorption cross section than the $^4I_{11/2}$ excited state of Er^{3+} thus rendering upconversion much more efficient. Furthermore, Yb^{3+} ion possesses only one excited state with energy around 10,000 cm^{-1} (λ= 1.0 μm), associated to a convenient wavelength since many commercial diodes are readily available [27], although, cooperative upconversion rate depends strongly on the host materials [21].

4.2.2. Absorption spectra of ZrO_2:Yb^{3+}, Er^{3+} nanocrystals

The absorption spectra of ZrO_2:Yb^{3+}, Er^{3+} are shown in figure 4.3. The low absorption cross section of Er^{3+} ions limits the pump efficiency. Ytterbium ions exhibit not only a large absorption cross section but also a broad absorption band between 800 and 1100 nm [22]. Additionally, the large spectral overlap between Yb^{3+} emission ($^2F_{5/2} \rightarrow {}^2F_{7/2}$) and Er^{3+} absorption ($^4I_{15/2} \rightarrow {}^4I_{13/2}$) results in an efficient resonant-energy transfer from Yb^{3+} to Er^{3+} in Yb^{3+} – Er^{3+} co-doped system [23].

The ground states are $^4I_{15/2}$ for Er^{3+} and $^2F_{7/2}$ for Yb^{3+}. The main absorption peaks for Er^{3+} and the corresponding energy levels are: 1524 nm ($^4I_{13/2}$), 962 nm ($^4I_{11/2}$) overlapped with the broad absorption band of Yb^{3+} ($^2F_{5/2}$), 782 nm ($^4I_{9/2}$), 652 nm ($^4F_{9/2}$), 542 nm ($^4S_{3/2}$), 525 nm ($^2H_{11/2}$), 490 nm ($^4F_{7/2}$), 452 nm ($^4F_{5/2}$), 438 nm ($^4F_{3/2}$), 406 nm ($^2H_{9/2}$) and 378 nm ($^4G_{11/2}$). The absorption band centered on 300 nm corresponds to the host (ZrO_2) gap and is shifted towards lower wavelengths as the Yb^{3+} concentration increases [24].

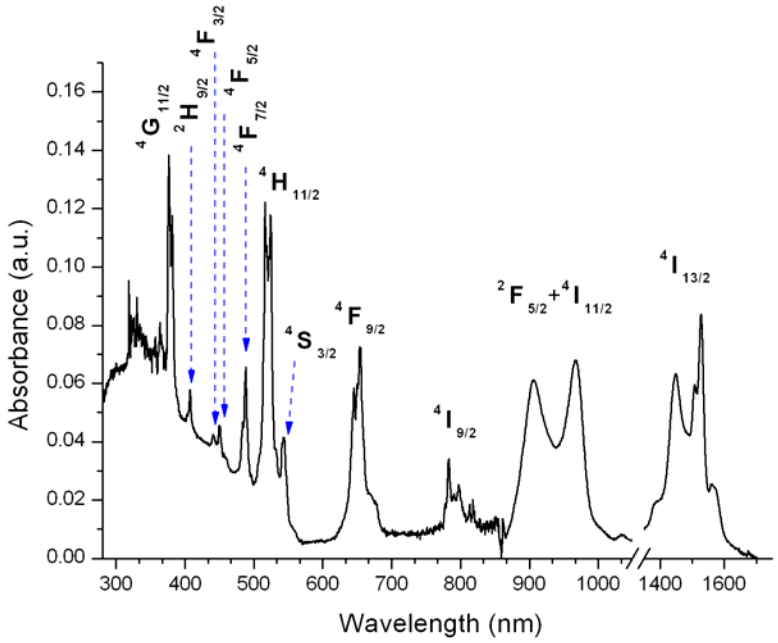

Figure 4.3: Absorption spectra of ZrO_2:Yb^{3+}, Er^{3+}.

4.3. LUMINESCENCE OF ZrO_2:Er^{3+} NANOCRYSTALS

The presence of erbium ion concentration determines the phase composition. For low concentration of dopant the dominant structure is the monoclinic phase. As the Er^{3+} ions concentration increases the tetragonal content increases obtaining a mixture of both crystalline phases [1]. Symmetry of the Zr^{4+} monoclinic and tetragonal phases are different (2/m in monoclinic and 4/mmm in tetragonal). Therefore, the symmetry of the Er^{3+} site in

the monoclinic phase is lower than in the tetragonal phase when Er^{3+} is incorporated in the ZrO_2. Lowering the site symmetry of the ion will cause an increase in transition probabilities of Er^{3+} ions in ZrO_2 and in consequence a higher luminescence for Er^{3+} ions incorporated in the monoclinic phase. Investigations on ZrO_2:Er^{3+} indicate that Er^{3+} migrates from the centre to the surface of the crystal during an annealing process [25]. This will increase the overall concentration of Er^{3+} ions placed in sites with reduced symmetry at the surface, even for the more symmetric tetragonal phase. So it is presumed that as the Er^{3+} concentration is increased the addition of the lattice distortion for charge compensation and the migration of Er^{3+} ions to the surface of the increasing tetragonal nanocrystallites accounts for an overall increase of sites with lower symmetry, giving an increase of luminescence [2].

4.3.1. Upconversion emission of ZrO_2:Er^{3+} nanocrystals

Visible, green and red, emission by the upconversion mechanism of ZrO_2:Er^{3+} are shown in figure 4.4. In this case samples were excited at 967 nm. Weak blue emission band was observed and it is shown in the inset of figure 4.4. The overall intensity is dominated by the green band. Due to the fact of using capillary tubes the emission of samples can be compared one to each other. The 2 mol% sample presented a relative high red intensity and a green intensity similar to others samples. With lower concentrations diminish the red band. The red band consists by two peaks produced by Stark splitting and centered at 680 and 660 nm that correspond to $^4F_{9/2} \rightarrow {}^4I_{15/2}$ transition. Green band has a peak near 564 nm ($^4S_{3/2} \rightarrow {}^4I_{15/2}$), and 550 nm ($^2H_{11/2} \rightarrow {}^4I_{15/2}$). Blue weak emission was obtained and its intensity also changes with ion concentration.

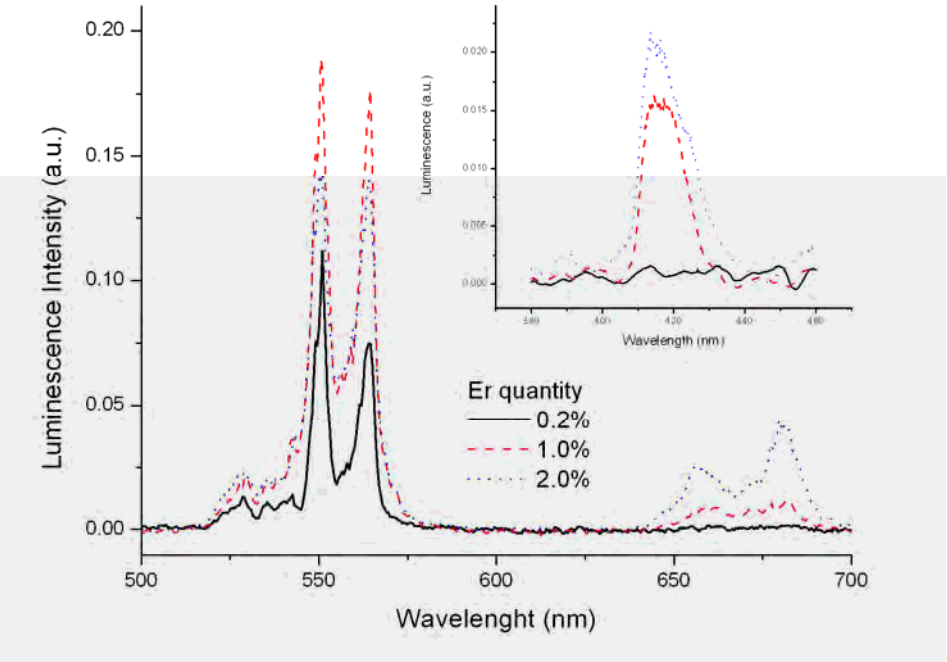

Figure 4.4: Upconverted emission spectra of ZrO_2:Er^{3+}. Inset shows blue emission.

The green emission was integrated and its relation with ion concentration analyzed. As it is shown in figure 4.5 the emission follows a nonlinear relation to ion concentration. The quadratic fit obtained suggests that ETU process is present on the emission mechanism and has considerably effect on resulted emission. Possible mechanisms are described afterwards.

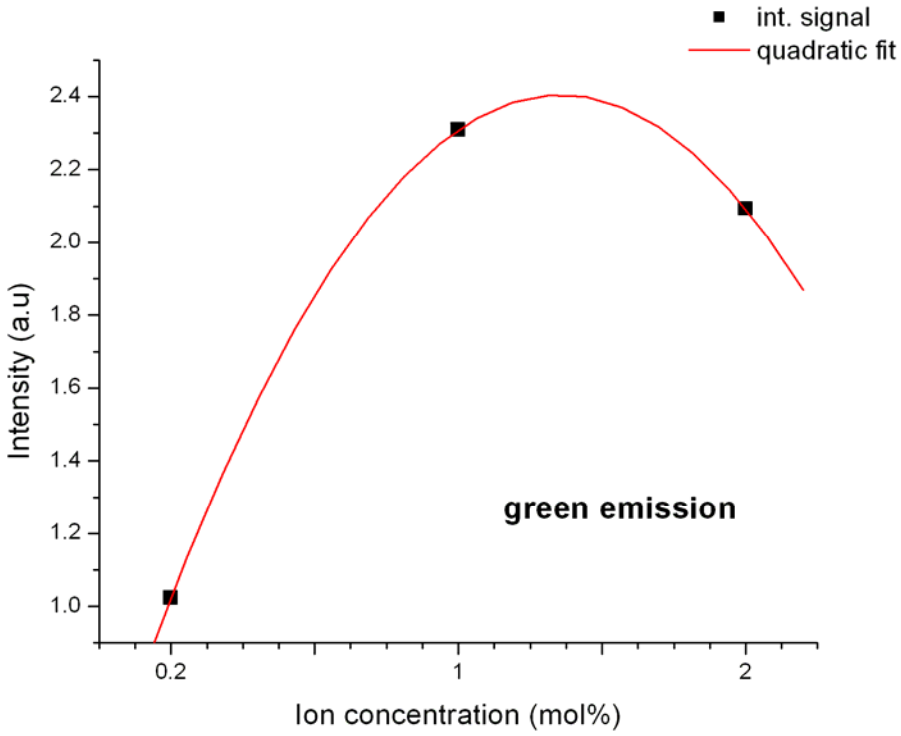

Figure 4.5: Integrated emission signal vs. ion concentration for Er^{3+} samples.

To obtain a better understanding of the upconversion process, a power dependence study of the upconverted emission intensity was performed. The emission spectra were obtained for ten different excitation power values and are shown in figure 4.6. The dependence of the signal emitted as function of the pump power is analyzed in order to infer the type of process involved on the upconverted emission. It has been shown that the intensity of the upconverted emission is proportional to some power *n* of the IR excitation. Experimental results were fitted by the equation:

$$I_{upc} = k \cdot I_{pump}^{n} \tag{4.1}$$

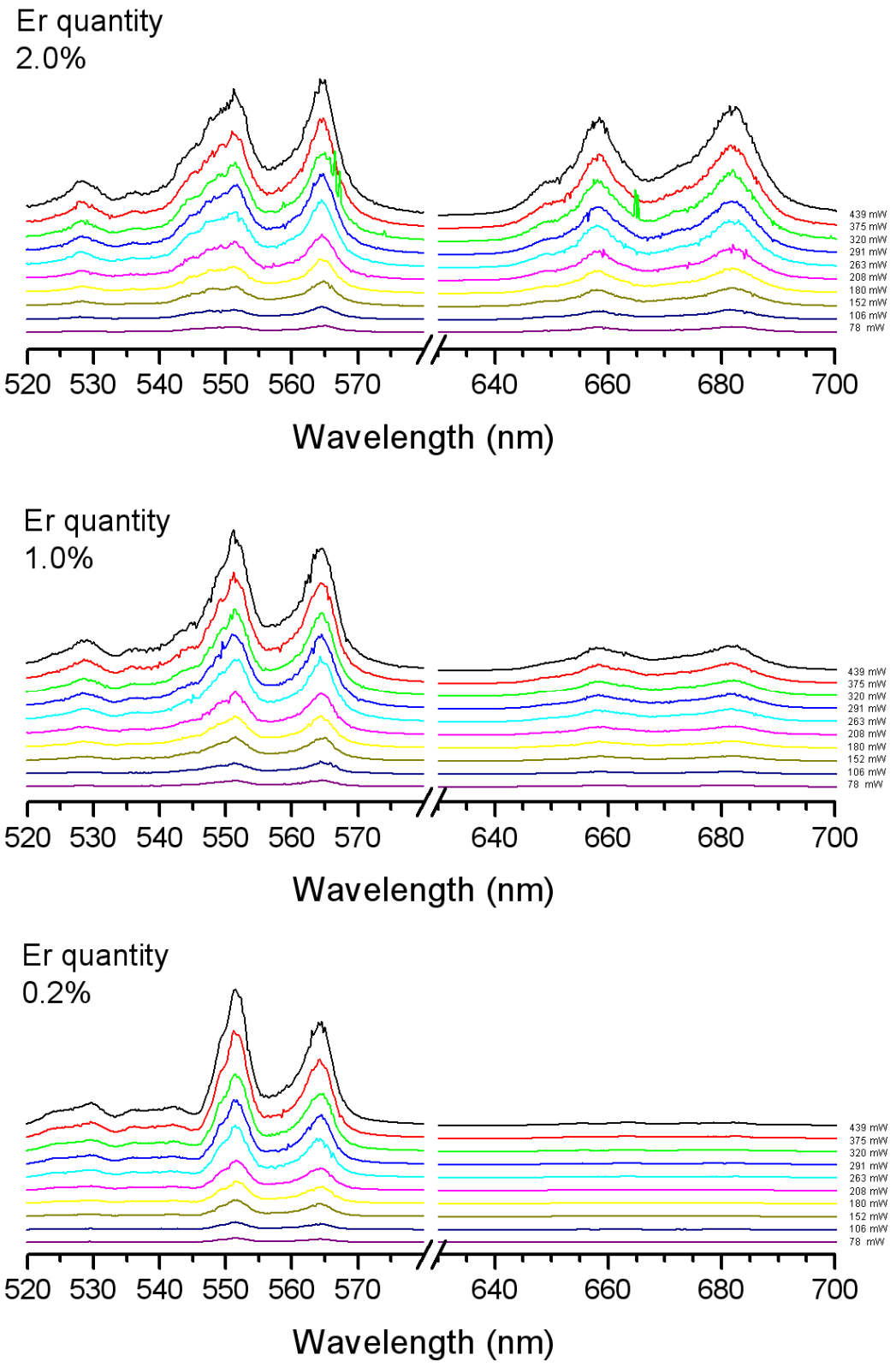

Figure 4.6: Upconverted emission spectra obtained by different excitation power.

where I_{upc} and I_{pump} stand for the upconverted and pumping signal respectively, and n is an integer denoting the number of photons required to produce such emission in the corresponding emitting level; this variable is related to the slope of each graphic, $\ln(I_{upc})$ versus $\ln(I_{pump})$, that are shown in figure 4.7 for Er^{3+} doped samples.

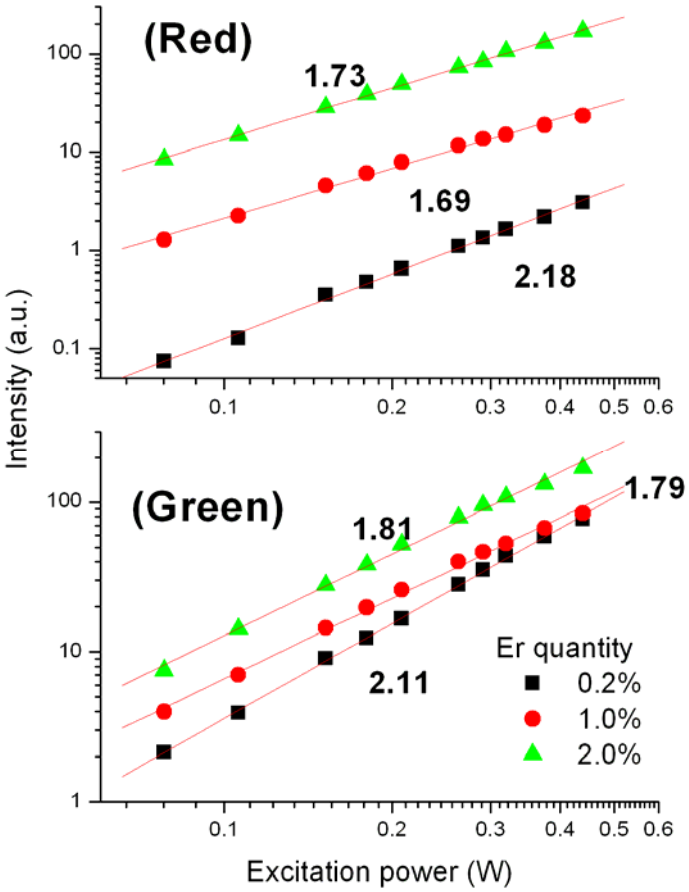

Figure 4.7: Dependence of the green and red upconversion emission as function of the pumping intensity for Er doped samples.

According to the results, the green and red bands required two-photon absorption in order to emit their respective signals. The values lower than two obtained for 1.0 and 2.0 mol% are evidences that suggest there are involved other mechanisms on the emission signals. For the red band, higher ion concentrations diminish the slope, which interpretation is described as follows. For low ion concentrations, $^4F_{9/2}$ level is fed non-radiatively by the mixed $^2H_{11/2}$ + $^4S_{3/2}$ level that require two–photon absorption to be populated. However, for higher ion concentration CR become much more important to feed the $^4F_{9/2}$ level and by this process one photon is essentially required to populate this level [1]. The slope value higher than one indicates that such level still receiving electrons from the mixed level.

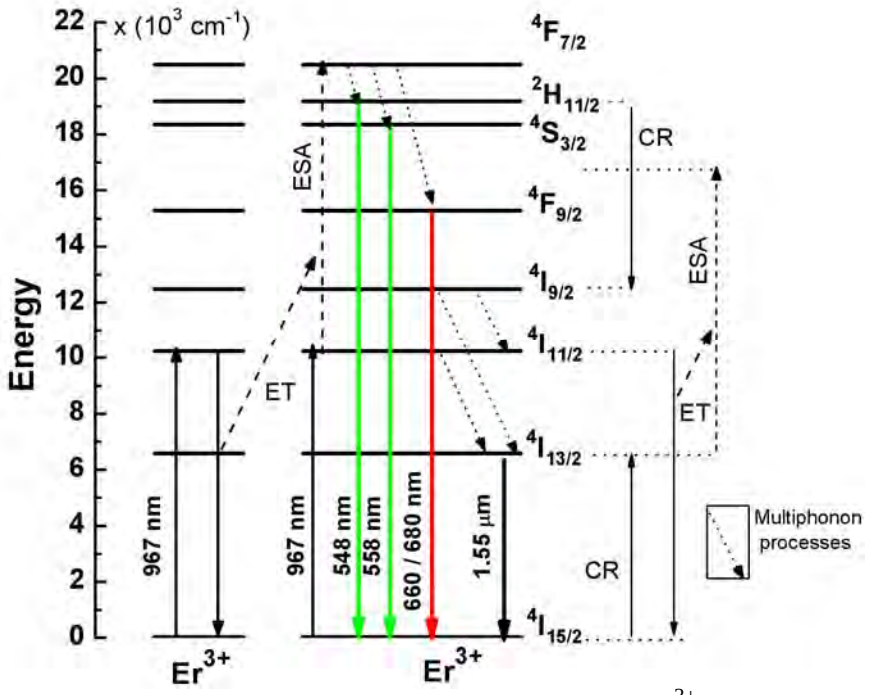

Figure 4.8: Energy levels diagram for the Er^{3+} system.

The energy level diagram of the emission processes is shown in figure 4.8. Assuming an excitation wavelength of 967 nm for the transition ($^4I_{15/2} \rightarrow {}^4I_{11/2}$) of Er^{3+}, the population in the $^4I_{11/2}$ level decays partly non-radiatively to the $^4I_{13/2}$ level and then relaxing to the ground state producing the well-known signal centered at 1.55 μm; and partly is promoted to the $^4F_{7/2}$ level by two-photon absorption due to ESA and ET among neighbouring Er^{3+} ions [1]. Once the $^4F_{7/2}$ is populated, consecutive multiphonon relaxation processes populate the mixed $^2H_{11/2}$ + $^4S_{3/2}$ and the $^4F_{9/2}$ levels that in turn decay radiatively to ground state ($^4I_{15/2}$) producing the green and red emission band.

The change in the intensity of the green and red band could be explained in terms of the CR process. CR ($^2H_{11/2}$ + $^4S_{3/2} \rightarrow {}^4I_{9/2}$) + ($^4I_{15/2} \rightarrow {}^4I_{13/2}$) becomes important at higher concentration, in this case levels $^4I_{9/2}$ and $^4I_{13/2}$ become populated. Level $^4I_{9/2}$ is partly depopulated producing the band centered at 780 nm, and partly relaxed non-radiatively to lower levels $^4I_{11/2}$ and $^4I_{13/2}$. For the population on the $^4I_{13/2}$ level, the energy could decay radiatively to ground state or undergoes an upconversion promotion above the $^4F_{9/2}$ level via the ET process ($^4I_{13/2}$ + $^4I_{11/2}$) $\rightarrow$ ($^4F_{9/2}$ + $^4I_{15/2}$) among neighboring ions. The overall result will be an enhanced red emission from the $^4F_{9/2}$ level and an increased quenching of the green luminescence from the mixed $^2H_{11/2}$ + $^4S_{3/2}$ level.

Thus, the experimental results showing the enhanced emission of the red band and the reduction of the green band suggest that in fact, follows the CR + ET mechanism described above (figure 4.6). This result implies that in ZrO_2:Er^{3+} it is possible to control the emission by controlling the Er^{3+} concentration [1].

4.3.2. NIR emission of ZrO_2:Er^{3+} nanocrystals

The NIR emission spectra were obtained for Er^{3+} doped samples, from figure 4.9 typical bands can be identified. The band centered at 1535 nm along with band at 1512 nm present an increment in luminescence intensity by increasing ion concentration. These spectra are in agreement with the spectra reported previously by others authors for different host materials [26].

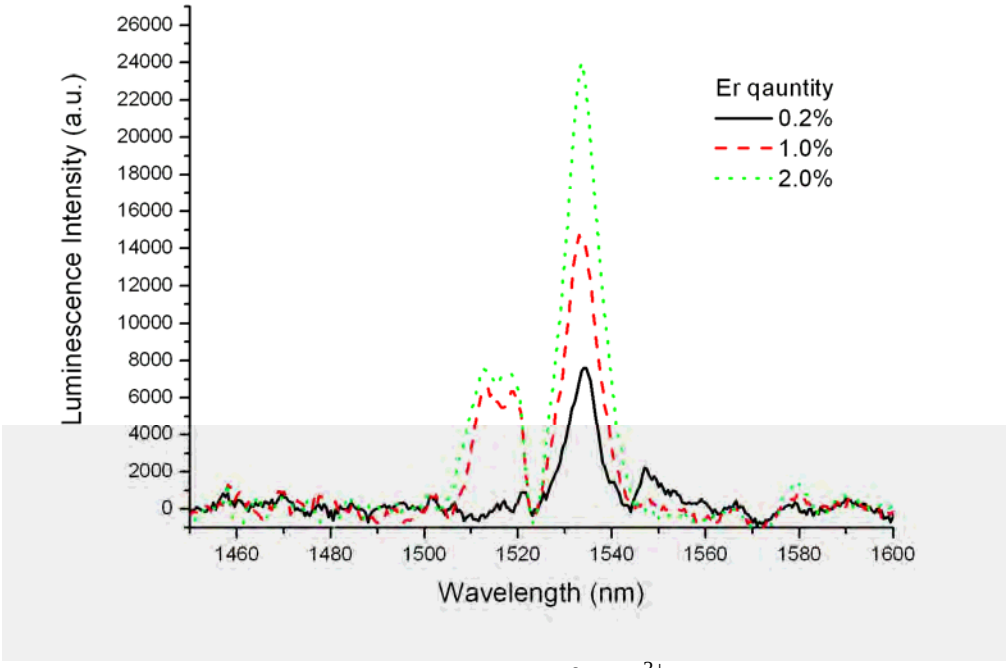

Figure 4.9: NIR emission spectra for Er^{3+} doped samples.

4.3.3. Fluorescence decay time of ZrO_2:Er^{3+} nanocrystals

The decay times calculated for NIR and green emissions by ion concentration are shown in figure 4.10. It is noticed that there are an increment on decay time values as ion concentration increases excluding 2 mol%, which its NIR decay time decreases and visible (VIS) decay time maintain its prior concentration value. The captured data and fitting adjustment of VIS and NIR decay curves are shown in figure 4.11 and 4.12 respectively. In the captured data of most samples were possible to fix two fitting curves, which the first one is faster than the second one. This behavior corresponds to the effect of different non-radiative mechanisms partially related with impurities during synthesis of samples. The larger the slope length is the more influence of non-radiative processes over emission. Calculated decay times are slightly lower than others reported due to concentration [26].

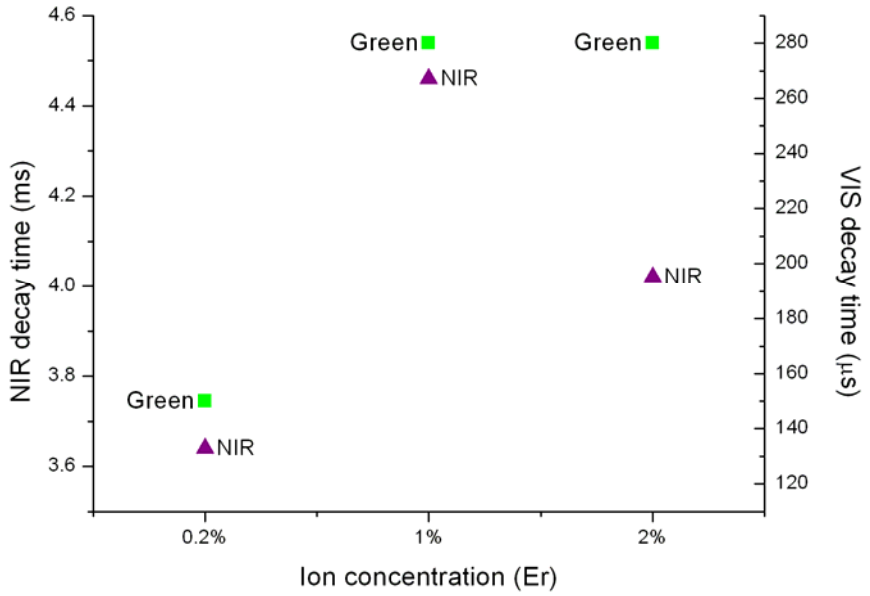

Figure 4.10: NIR and visible (VIS) decay times for Er^{3+} samples.

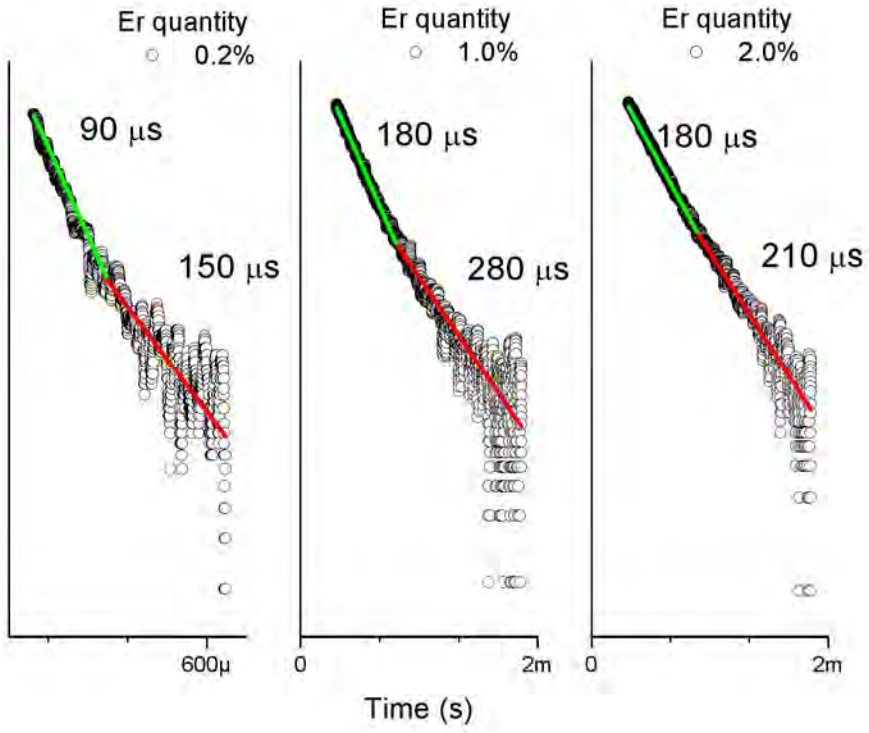

Figure 4.11: VIS decay curves and fitting values.

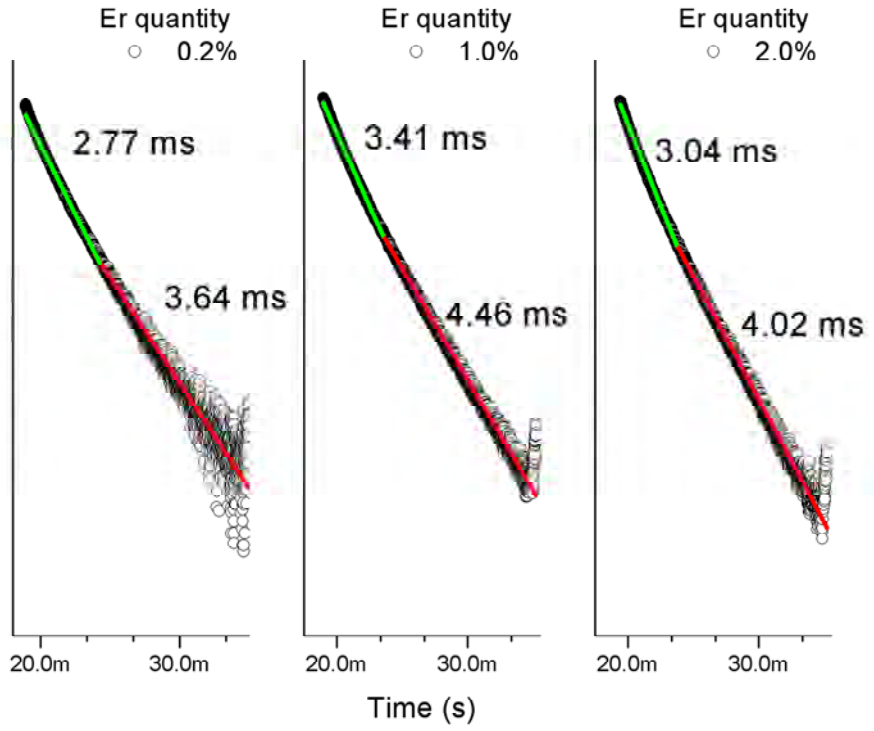

Figure 4.12: NIR decay curves and fitting values.

4.4. LUMINESCENCE OF ZrO_2:Yb^{3+}, Er^{3+} NANOCRYSTALS

The main arguments that justify the use of ytterbium as a synthesizer of erbium ions is the high absorption cross section as was described previously on section 4.3. In next section the luminescence properties are considered

4.4.1. Upconversion emission of ZrO_2: Yb^{3+}, Er^{3+} nanocrystals

The nanophosphors emission spectra in the visible wavelength range, under 967 nm excitation, are shown in figures 4.13(a) and 4.13(b) for samples grouped by constant doped concentration of Yb^{3+} and Er^{3+} respectively. The main difference between groups is the changing in intensity relation between green and red emissions. The spectra exhibit four distinct emission bands, the red band centered on 670 nm (two peaks) produced by the transition $^4F_{9/2} \rightarrow {}^4I_{15/2}$; the green band centered on 544 nm produced by the transition $^2H_{11/2} + {}^4S_{3/2} \rightarrow {}^4I_{15/2}$; two weak bands, the blue centered on 410 nm corresponding to the transition $^2H_{9/2} \rightarrow {}^4I_{15/2}$, and the UV centered on 385 nm which corresponds to the transition $^4G_{11/2} \rightarrow {}^4I_{15/2}$ (not shown). The emission intensity of these four visible bands depends on the Yb^{3+} concentration. The green emission is dominant for low concentration but diminishes as the concentration increases, while the UV, blue and red emissions increase [39]. The intensity ratio of green luminescence to that of red luminescence has

decreased with an increase of concentration of Yb^{3+}. The same behavior has been observed in Y_2O_3 [27].

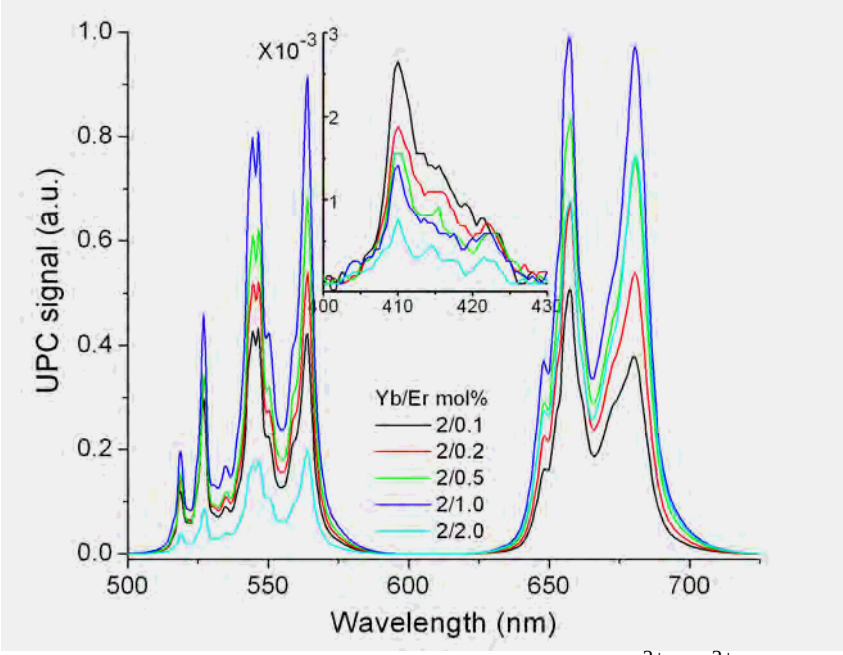

Figure 4.13(a): Visible emission spectra of ZrO_2:Yb^{3+}, Er^{3+}. The inset shows the blue emission band.

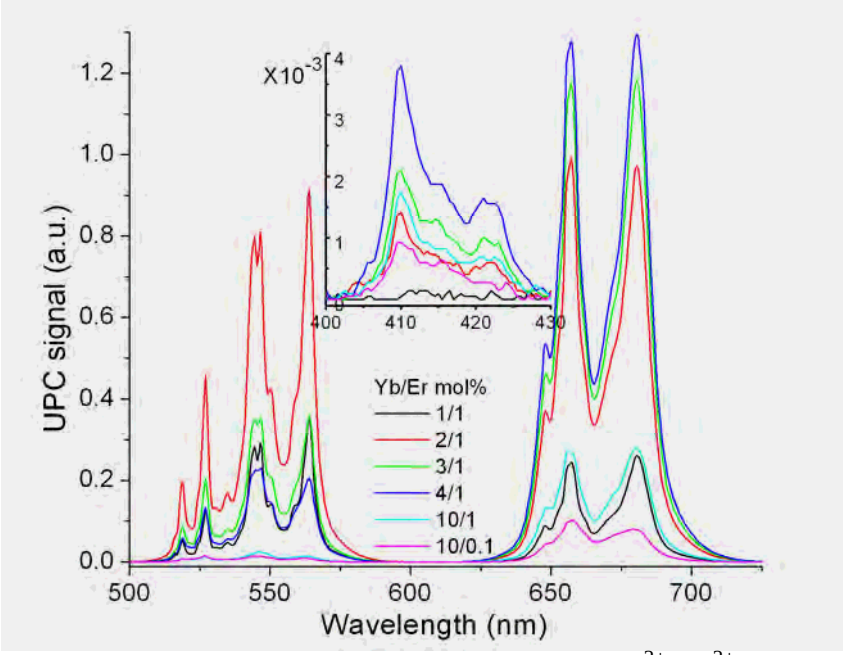

Figure 4.13(b): Visible emission spectra of ZrO_2:Yb^{3+}, Er^{3+}. The inset shows the blue emission band.

Once more, the emission signal intensity of the samples was compared with their ion concentration. In this case, which are two ions involved, the data were separated as shown in figure 4.14. Results suggest that on visible bands ETU processes are implied; although, on constant erbium doped samples, the fitting is better than on constant ytterbium doped samples.

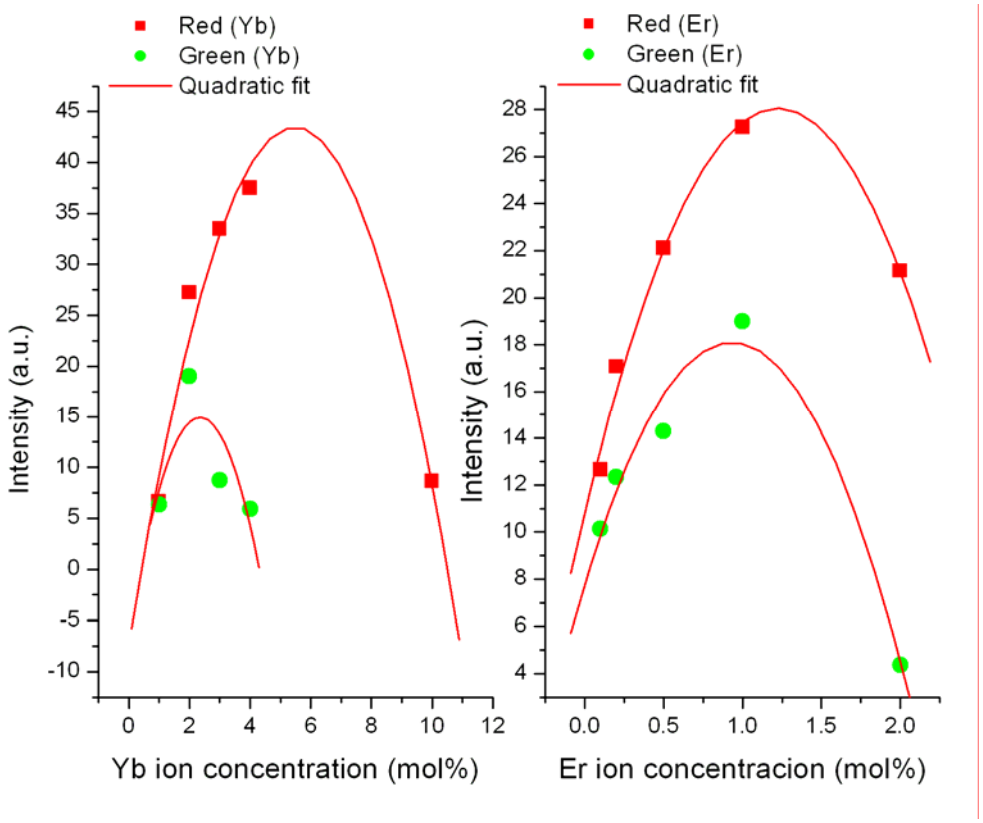

Figure 4.14: Relation between emission intensity and ion concentration. Constant 1 mol% Er and 2 mol% Yb samples are shown on left and right side respectively.

The dependence of the upconverted integrated signal intensity (I_{upc}) was analyzed as function of the pumping intensity (I_{pump}) to elucidate the mechanism to produce the UC emission (figures 4.14, 4.15 and 4.16).

The energy level diagram of the emission processes is shown in figure 4.18. The green and red emissions originate from the transitions $^2H_{11/2}$ + $^4S_{3/2}$ → $^4I_{15/2}$ and $^4F_{9/2}$ → $^4I_{15/2}$ of Er^{3+}, respectively. In Er^{3+} ion doped materials these transitions are due to ESA and ETU mechanisms respectively [28]. The ESA mechanism is comprised of only one Er^{3+} ion while the ETU mechanism occurs by the ET process, where two excited ($^4I_{11/2}$) Er^{3+} ions interact with each other and one is de-excited to $^4I_{15/2}$ and the other is excited to $^4F_{7/2}$. This ET process is ion-concentration dependent. The $^4F_{7/2}$ (Er^{3+}) state decays non-radiatively to the $^4F_{9/2}$ (Er^{3+}) level and then decays radiatively producing red emission band centered at 670 nm. A third mechanism for upconversion is ET from Yb^{3+} ($^2F_{5/2}$) to Er^{3+} ($^4I_{11/2}$). The

increase of Yb^{3+} concentration promotes the ET from Yb^{3+} ($^2F_{5/2}$) to Er^{3+} ($^4I_{11/2}$). Thus, the $^4F_{9/2} \rightarrow {}^4I_{15/2}$ transition is considerably accelerated [29].

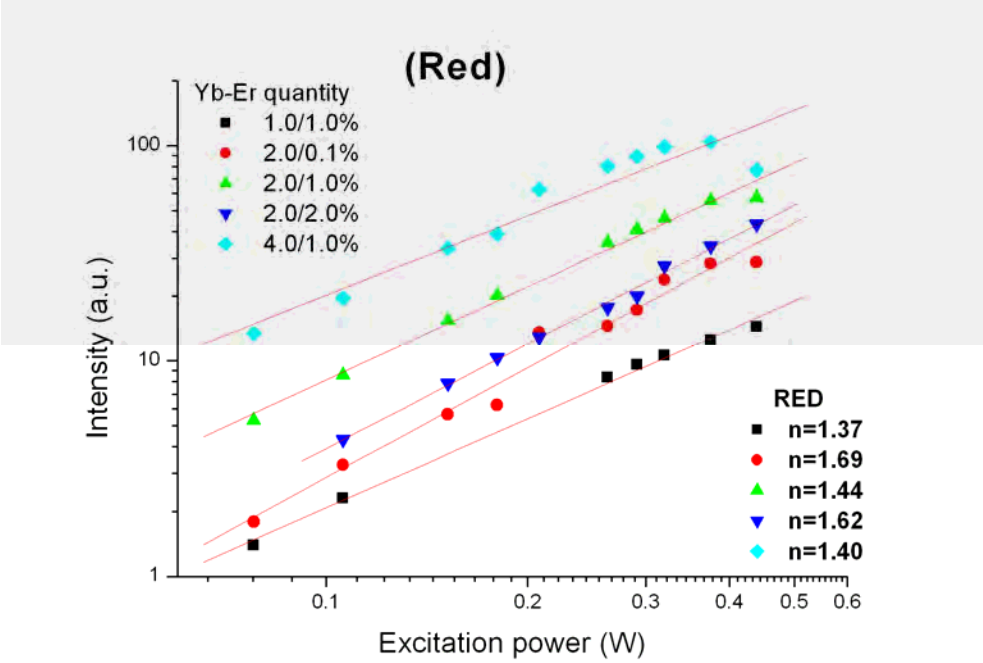

Figure 4.15: Dependence of the red upconversion emission as function of the pumping intensity.

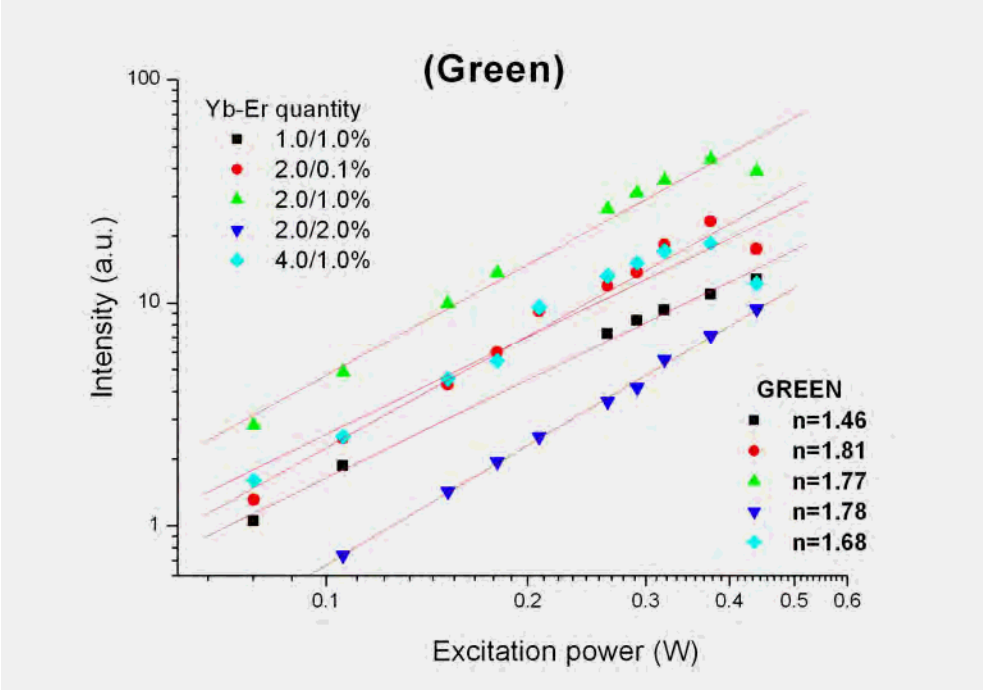

Figure 4.16: Dependence of the green upconversion emission as function of the pumping intensity.

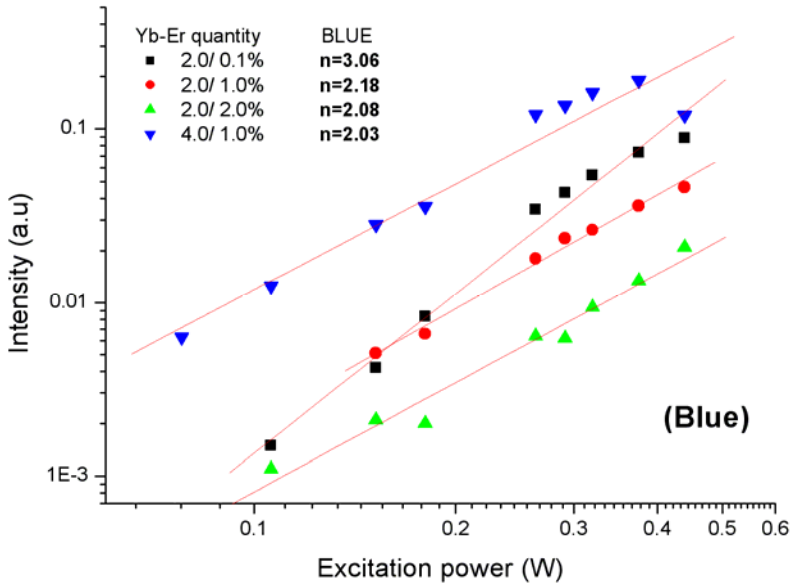

Figure 4.17: Dependence of the blue upconversion emission as function of the pumping intensity.

In summary, analyzing the energy diagram, the $^4F_{9/2}$ level can be reached by absorption of two pump photons, and by CR mechanism followed by ET from another Er^{3+} or Yb^{3+}. Thus from this discussion it has been proposed that the power dependence on the red emission signal should be $n < 2$, in this case $n \approx 1.5$ [32], as it shown in figure 4.15.

The green emission must be also due to additional mechanism. Excitation to the $^2H_{11/2}$ + $^4S_{3/2}$ level is due to two photon absorption by Er^{3+} excited states absorption ESA, or by the gradual energy transfer from excited Er^{3+} (or Yb^{3+}) ions to excited Er^{3+} ions (ET). The power dependence also should be $n < 2$, as it shown in figure 4.16; in this case $n \approx 1.7$ was obtained for all Yb^{3+} concentrations [39].

The electrons in the mixed levels $^2H_{11/2}$ + $^4S_{3/2}$ can acquire one pumping photon by ET among neighbouring ions or by ESA promoting electron to $^4G_{7/2}$ that relax to $^4G_{11/2}$ producing UV emission and to $^2H_{9/2}$ producing the blue emission. In this case it is suggested that one cooperative photon and one pumping photon that is equivalent to half cooperative photon are required to produce UV and blue emission, although, this argument could not been proved during this analysis. This explanation is in correspondence with the obtained value $n \approx 2$ for all Yb^{3+} concentration [39] except for ZrO_2:Yb^{3+}(2%), Er^{3+}(0.1%) sample that has the lowest Er^{3+} concentration, as it shown in figure 4.17.

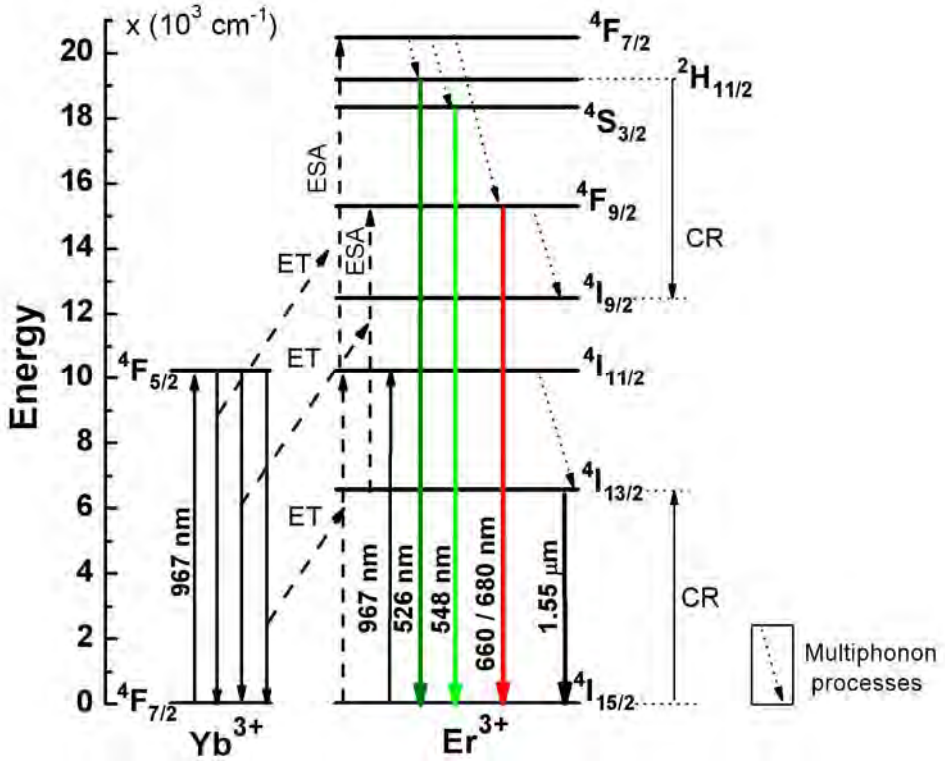

Figure 4.18: Energy levels diagram for the Yb^{3+}– Er^{3+} system.

The cooperative-upconversion emission increases with higher Er^{3+} concentrations. The energy-transfer process was found to increase with Yb^{3+} concentration. The cooperative-upconversion that results from Er^{3+} – Er^{3+} interaction was almost constant. The high transfer efficiency can be ascribed to the fact that both Yb^{3+} and Er^{3+} concentrations are high to cause excitation diffusion among Yb^{3+} and Er^{3+} ions [29].

4.4.2. NIR emission of ZrO_2: Yb^{3+}, Er^{3+} nanocrystals

The 1.5 µm NIR emission spectra obtained for ZrO_2:Yb^{3+}, Er^{3+} doped samples are shown in figure 4.19, where the emission of 0.2 mol% of Er^{3+} is included for reference. The band centered at 1578 nm and specially the peaks at 1533 nm and 1512 nm presents an increment in their luminescence by ion concentration with apparent no relation. If sample ZrO_2:Yb^{3+}(2%), Er^{3+}(0.5%) is considered, there is a decrement in emission when increasing Er^{3+} concentration; that suggest a quenching phenomena. By the other hand, increasing Yb^{3+} concentration on ZrO_2:Yb^{3+}(2%), Er^{3+}(1%) sample also implies a decrement in the emission. That behavior suggests that ytterbium requires higher concentration to present quenching than erbium.

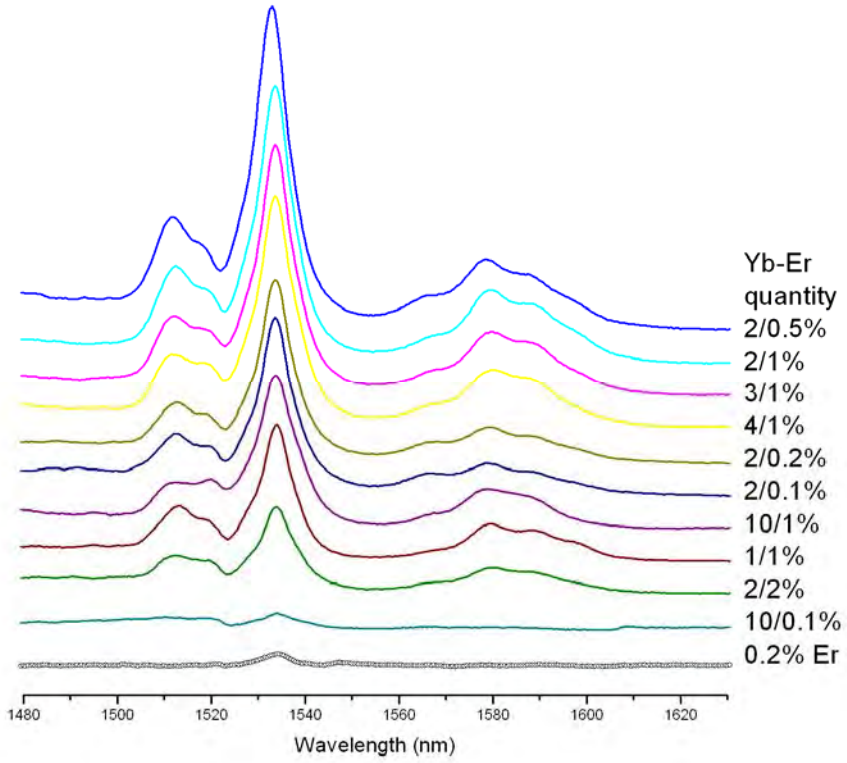

Figure 4.19: NIR (1.5 μm) emission spectra for Yb^{3+}, Er^{3+} doped samples.

4.4.3. Fluorescence decay time of ZrO_2: Yb^{3+}, Er^{3+} nanocrystals

The decay times calculated for NIR, IR and VIS emission are reported on table 4.1. The energy transfer efficiency from ytterbium to erbium $(^2F_{5/2} - {}^4I_{15/2}) \rightarrow (^4F_{7/2} - {}^4I_{11/2})$ was added and calculated by the following reduced equation [30].

$$\eta = 1 - \frac{\tau_{Yb-Er}}{\tau_{Yb}} \tag{4.2}$$

Where τ_{YbEr} and τ_{Yb} are decay times for codoped and Yb^{3+} low doped concentration samples respectively. Low efficiency values are obtained except from the ZrO_2:Yb^{3+}(2%), Er^{3+}(2%) sample. In order to note the behavior of the fast slope on decay times, figures 4.20 and 4.21 are presented. The slopes changes in length suggest their relevance on the emission mechanism of each sample. Decay times calculated for NIR (1.5 μm) and green emissions by ion concentration are shown in figure 4.22. It has been noticed that with constant Yb^{3+} ion concentration there is a decrement on NIR decay time values as Er^{3+} ion concentration increases. In the opposite case, with constant Er^{3+} ion concentration NIR decay time values increases as Yb^{3+} ion concentration is increased, excluding the ZrO_2:Yb^{3+}(10%), Er^{3+}(1%) sample, which NIR decay time is similar to prior ZrO_2:Yb^{3+}(3%), Er^{3+}(1%) sample value.

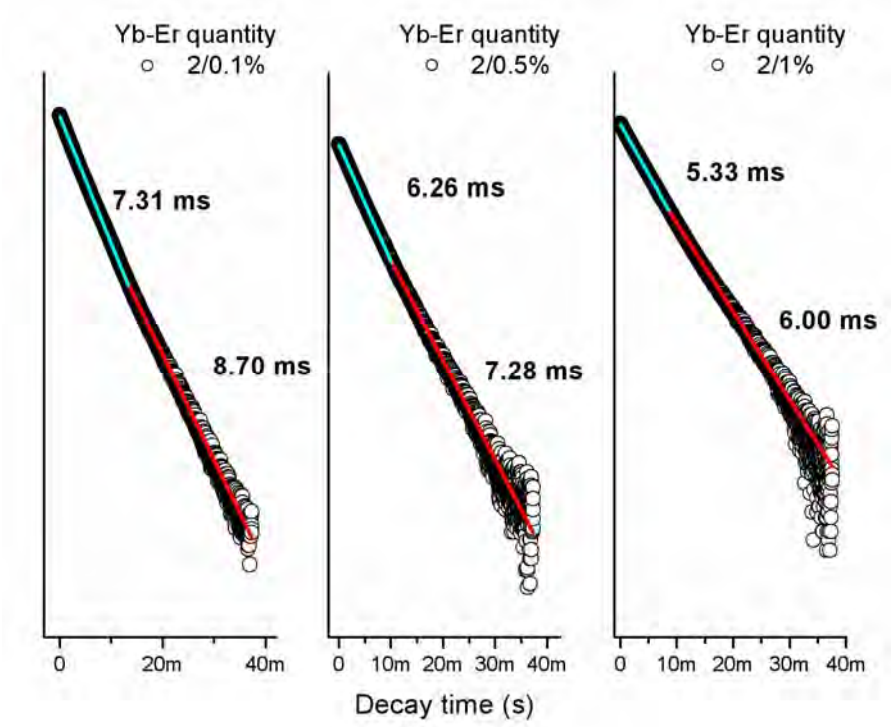

Figure 4.20 NIR decay curves and fitting values.

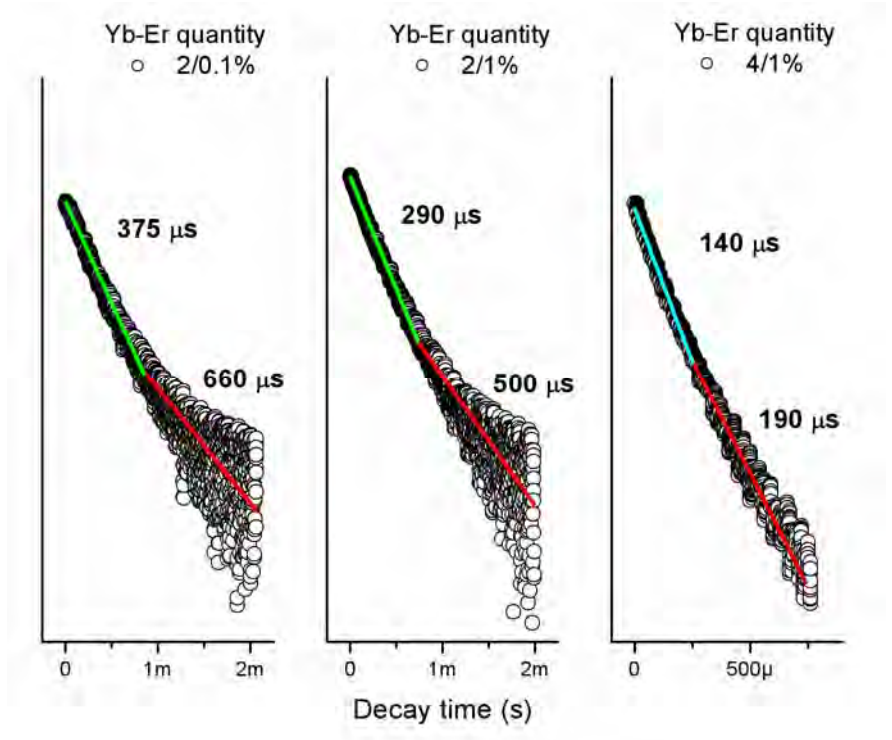

Figure 4.21 VIS decay curves and fitting values.

Decay times of both bands IR (1040 nm) and visible (green and red emission) diminish as the Er^{3+} concentration increases (figure 4.23); also, the decrement is slower than in Yb^{3+} case, which has an exception in tendency on ZrO_2:Yb^{3+}(2%), Er^{3+}(1%) sample. In fact τ_{nir} decrease faster than τ_{cuc} suggesting that additional process are present, which its interpretation was already described in this section.

TRANSITION	$^4I_{13/2}$–$^4I_{15/2}$		$^4F_{9/2}$–$^4I_{15/2}$		$^2S_{3/2}$+$^2H_{11/2}$–$^4I_{15/2}$		($^2F_{5/2}$–$^4I_{15/2}$)→($^4F_{7/2}$–$^4I_{11/2}$)
Decay time [µs]	**Fast**	**Slow**	**Fast**	**Slow**	**Fast**	**Slow**	**Energy Transfer Efficiency**
2/0.1 mol%	7310	8700	450	753	375	660	0.103
2/0.2 mol%	6620	7490	430	690	350	620	0.103
2/0.5 mol%	6260	7280	420	690	300	550	0.103
2/1 mol%	5330	6000	430	660	290	500	0.273
2/2 mol%	2930	4150	400	655	200	370	0.686
1/1 mol%	4850	5830	420	528	280	430	0.373
2/1 mol%	5330	6000	430	660	290	500	0.273
3/1 mol%	5350	6550	270	360	180	240	NA
4/1 mol%	5890	6840	210	310	140	190	0.132
10/1 mol%	6120	6530	100	150	160	160	NA
10/0.1 mol%	6970	8460	20	30	85	70	NA

Table 4.1: Decay times obtained for the samples under study.

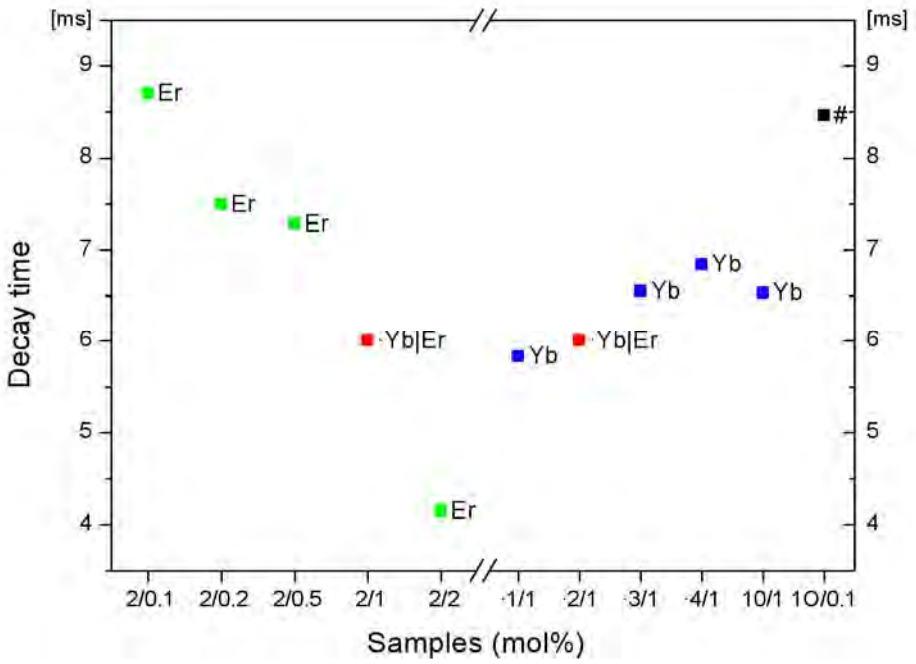

Figure 4.22: NIR (1.5 µm) decay times for ZrO_2:Yb^{3+}, Er^{3+} samples. Left side presents Yb^{3+} constant samples. Right side presents Er^{3+} constant samples.

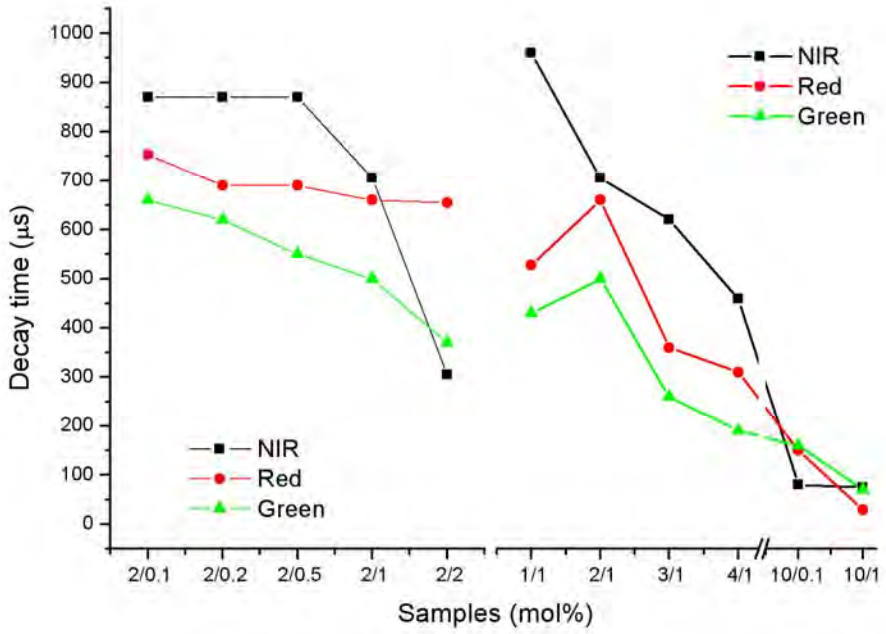

Figure 4.23: IR (1040 nm) and VIS decay times for ZrO_2:Yb^{3+}, Er^{3+}samples. Left side presents Yb^{3+} constant samples. Right side presents Er^{3+} constant samples.

In samples with constant Er^{3+} concentration the red emission ($^4F_{9/2}$ → $^4I_{15/2}$) increases relative to the green with an increase in the concentration of Yb^{3+} (figure 4.24). In similar way the samples with constant Yb^{3+} concentration the red become stronger as the concentration of the Er^{3+} ions is increased. In single doped Er^{3+} nanocrystals a resonant cross relaxation (CR) of type $^4F_{7/2}$ → $^4F_{9/2}$ and $^4F_{9/2}$ ← $^4I_{11/2}$ could directly populate the red emitting $^4F_{9/2}$ state either when exciting resonantly the $^4I_{11/2}$ state with 980 nm excitation. This CR process is concentration dependent so increasing the number of Er^{3+} ions would increase the efficiency of the mechanism. It should also be noted that the Yb^{3+} to Er^{3+} concentration ratio is not the key to red emission enhancement [18].

According to figure 4.25, the best luminescent sample ZrO_2:Yb^{3+}(2%), Er^{3+}(1%) presented a good luminescence and acceptable red to green emission relation of 143:100 however red emission was no perceptible to naked eye at all due to the green emission presence. Synthesizing a mainly red emission sample was expected; as a consequence, the red/green emission ratio became a considered factor during analysis of samples. In agreement with this, the ZrO_2:Yb^{3+}(10%), Er^{3+}(1%) sample was suitable for that requirement, achieved a emission ratio of 1356:100. Nonetheless, the upconversion emission was 80% lower than the best luminescent sample under study.

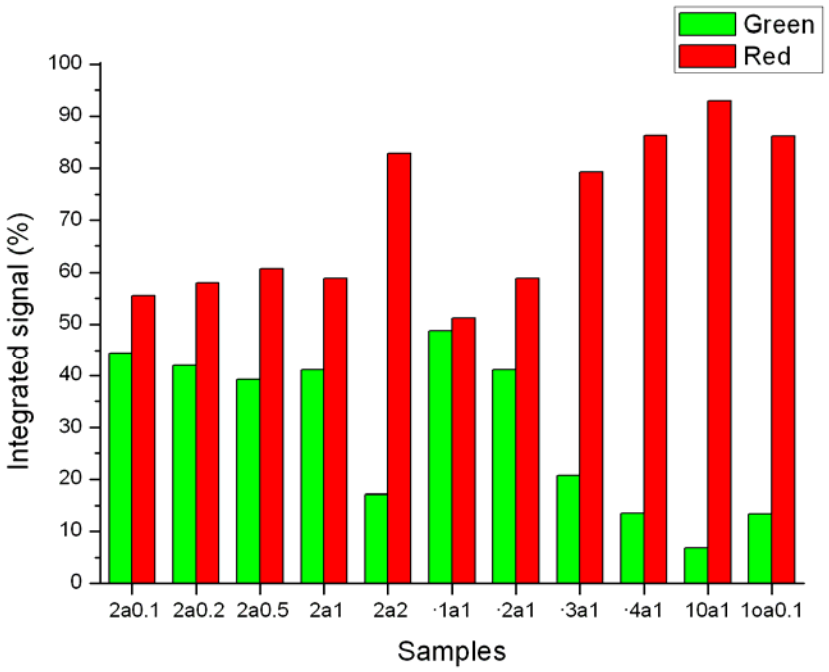

Figure 4.24: Green and red emission intensity by sample.

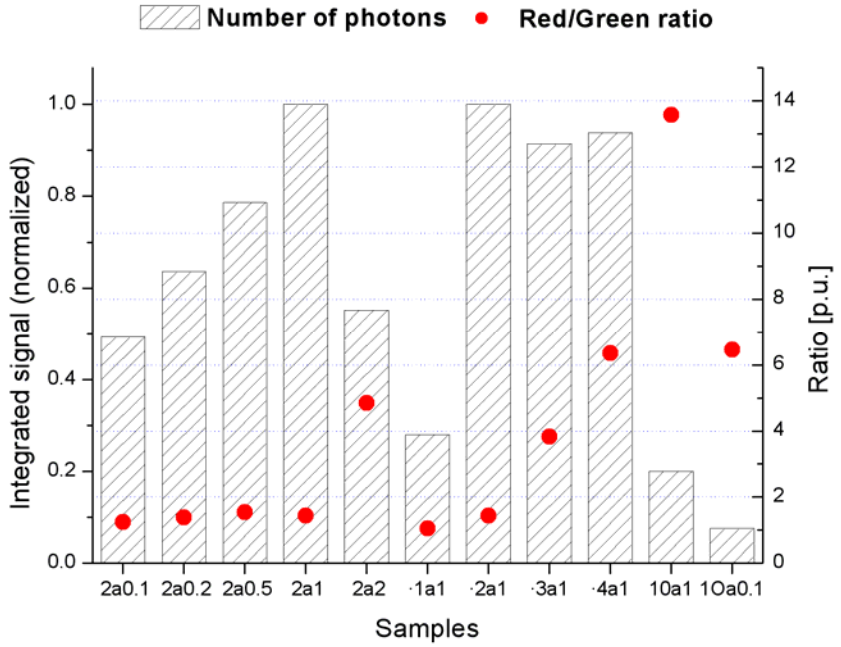

Figure 4.25: Photons implicated on emission by sample and red/green ratio.

This way, the experimental results showed that was a possible range not considered in this study, in which a more suitable sample can be obtained between samples ZrO_2:Yb^{3+}(4%), Er^{3+}(1%) to ZrO_2:Yb^{3+}(10%), Er^{3+}(1%); thus, obtain a sample with both notable good red/green emission ratio and proper luminescence could not be discarded.

4.5. LUMINESCENCE OF ZrO_2:Yb^{3+} NANOCRYSTALS

The special electronic configuration of Yb^{3+} makes the 4*f* electrons less shielded than in other ions of the lanthanide series, showing higher tendency to interact with the lattice and neighbor ions [18]. Yb^{3+} ion is generally used as sensitizer but it has also been studied as active ion in different matrices such as YAG, Y_2O_3 and heavy metal halide crystals [31-33]. The main interest is to be used for high power laser in the IR range and for switches using the intrinsic bistability properties [40]. It has been reported that the interaction of two Yb ions produce visible emission. This emission is named cooperative upconversion (CUC) and was first observed by Nakazawa in $YbPO_4$ [34]. CUC emission was explained in terms of the relaxation of a virtual state formed by the ionic interaction of two Yb^{3+} ions bridged by an oxygen atom and enhanced for the high surface area of nanocrystals [19].

In nanocrystalline oxide ceramics the rare-earth impurity ions diffuse to the outer part of the nanocrystallite [25]. Then, it is suggested is a gradient of Yb^{3+} concentration from the center to the surface that promotes a higher concentration of Yb^{3+} pairs at the distorted lattices near the surface and minimizes outer cell distances due to surface reconstruction of the crystallites at higher Yb^{3+} concentrations. Thus, the nanosized nature of the phosphors allows an enhanced cooperative absorption [35].

4.5.1. Cooperative absorption of ZrO_2:Yb^{3+} nanocrystals

The absorption spectra, displayed in figure 4.26, present the characteristic broad absorption band of Yb^{3+} ion corresponding to $^2F_{7/2} \rightarrow {}^2F_{5/2}$ transition. Such band present characteristics peaks centered at 910, 942, 972 and 1020 nm and are in agreement with the results reported by other groups in different matrices. The crystalline structure changes due to the increment of Yb ions. There are no absorption evidences of other rare earth ions, in particular Er^{3+} and Tm^{3+} ions.

A broad absorption band centered at 453 nm was observed for every Yb^{3+} concentration used. It is named cooperative absorption and is produced by simultaneous excitation of two Yb ions. Few papers have proposed that in some cases such pairs are bridged by an oxygen atom forming the system Yb–O–Yb [36,37]. In this case, the overlapping between the Yb–4*f* and the O–2*p* orbitals enhance the interaction of active ion an then the cooperative absorption. Because this band is strong and corresponds to the second harmonic of the infrared (IR) band it is considered as the physical evidence of the process described above [38].

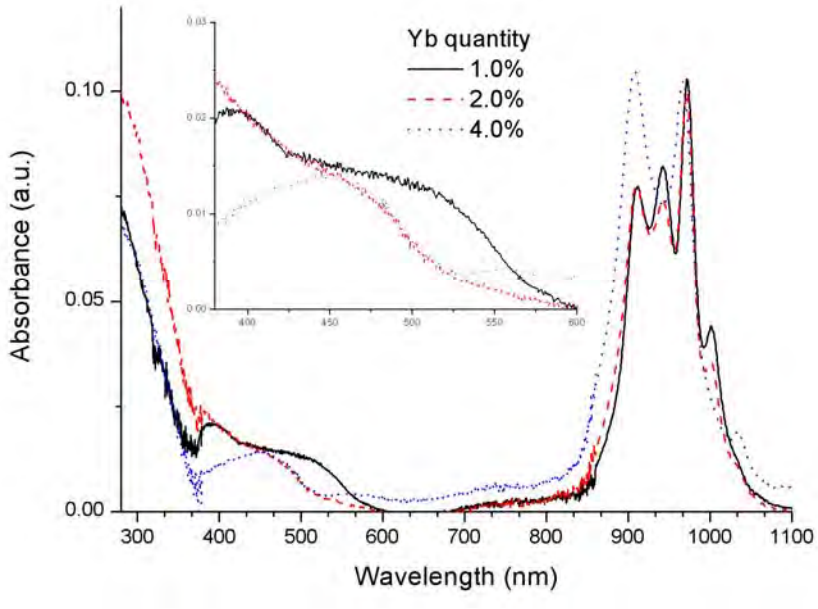

Figure 4.26: Absorption spectra of ZrO_2:Yb^{3+}.

4.5.2. Cooperative emission of ZrO_2:Yb^{3+} nanocrystals

Visible emission is shown in figure 4.27. CUC emission occurs at 505 nm. It is approximately twice the energy of the IR luminescence of single ion suggesting that is the result of the radiative relaxation of excited Yb^{3+} pairs accompanied by the emission of a visible photon. The peaks at 477 and 488 nm are characteristic of Tm^{3+} emission $^1G_4 \rightarrow {}^3H_6$ as a result of the energy transfer by Yb^{3+}. The lines at 525, 542 and 564 nm, and the red band are characteristic of the $^2H_{11/2} + {}^4S_{3/2} \rightarrow {}^4I_{15/2}$ and $^4F_{9/2} \rightarrow {}^4I_{15/2}$ transitions of Er^{3+} ion due to the energy transfer from Yb^{3+} to Er^{3+} ion and is similar to the emission obtained in the system Yb^{3+} – Er^{3+} [39]. There was not observed blue emission produced by traces of Er^{3+} ions. Because the presence of Er^{3+} and Tm^{3+} impurities was not detected in the absorption spectra it has to be very low concentration, although their traces present very efficient upconversion processes. Assuming that Er^{3+} and Tm^{3+} traces are derived from impurities on Yb precursor, when increasing Yb^{3+} ion concentration there were no increment of the green and red emission bands, suggesting that the dominant effect is the Yb pair formation and hence the CUC emission at 505 nm.

The cooperative upconversion emission of ZrO_2:Yb^{3+} nanocrystals are much higher than signal reported for different host in bulk samples [24,40]. These results suggest that the high efficiency of the CUC emission is result of the small crystallite size and the kind of host. Thus, the strong visible emission of ZrO_2:Yb^{3+} nanophosphor could be explained in terms of the high surface area and low phonon energy of the nanocrystals.

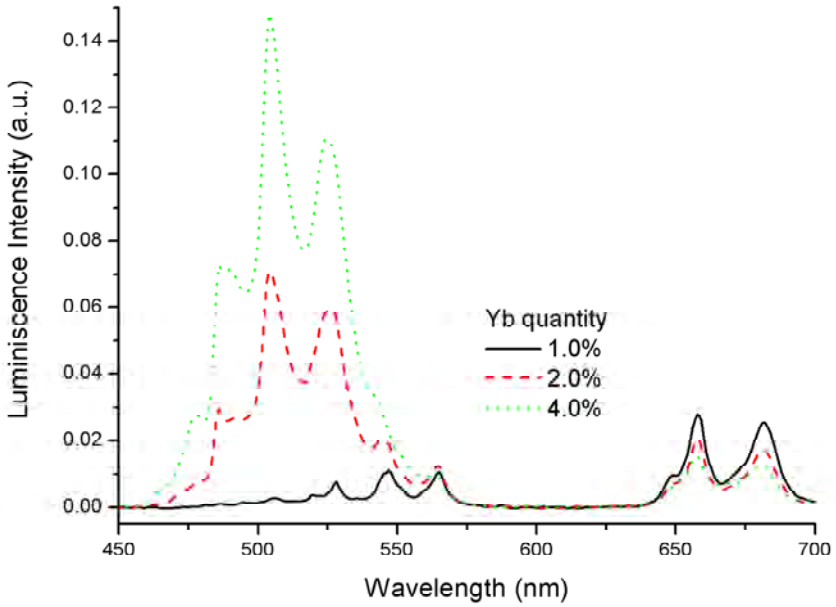

Figure 4.27: Emission spectra of ZrO_2:Yb^{3+}.

The dependence of the upconverted integrated signal intensity (I_{upc}) is analyzed as function of the pumping intensity (I_{pump}) to elucidate the mechanism to produce the CUC emission (figure 4.28). For CUC emission $n \approx 2$ confirming that such emission is the result of two-photon process.

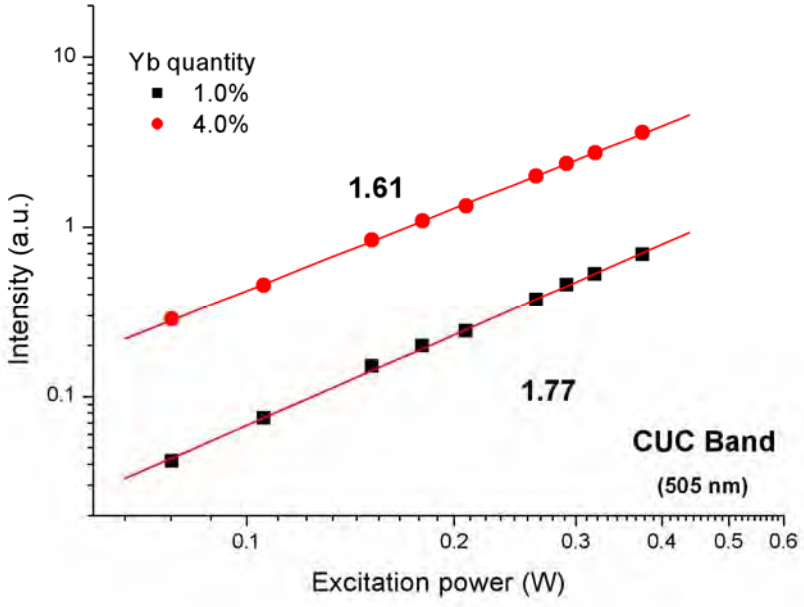

Figure 4.28: CUC (505nm) integrated signal as function of the pumping intensity.

The green and red emission band requires also a two photon process induced by energy transfer from the sensitizer Yb to Er impurities. The low value in the number of photons suggests the presence of CR process (figure 4.29). The emission produced by traces of Tm^{3+} ions requires the absorption of two photons. This is possible only by non-radiative energy transfer of one Yb–O–Yb molecule to Tm^{3+} ion [27]. According to obtained results is possible to propose the energy level diagram that is shown in figure 4.30.

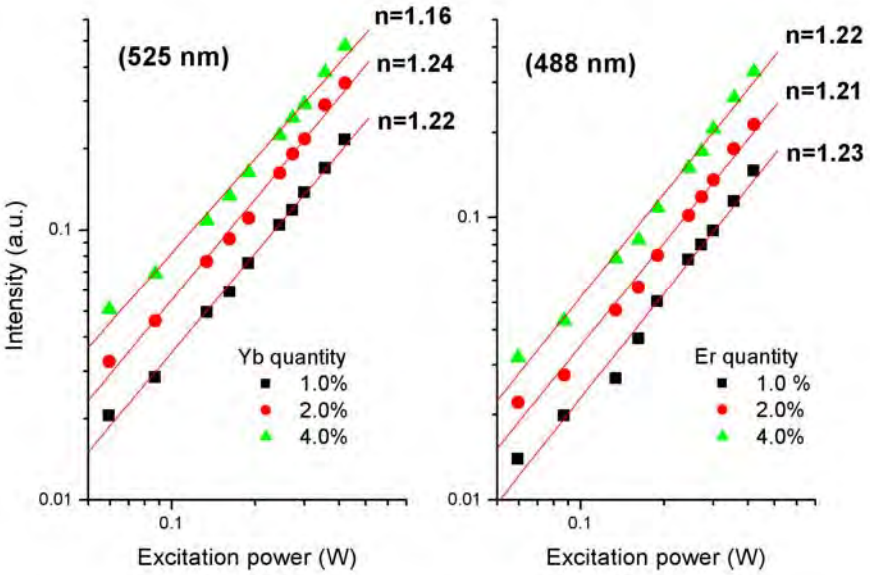

Figure 4.29: Dependence of the Er^{3+}(525 nm)and Tm^{3+}(488 nm) upconversion emission as function of the pumping intensity.

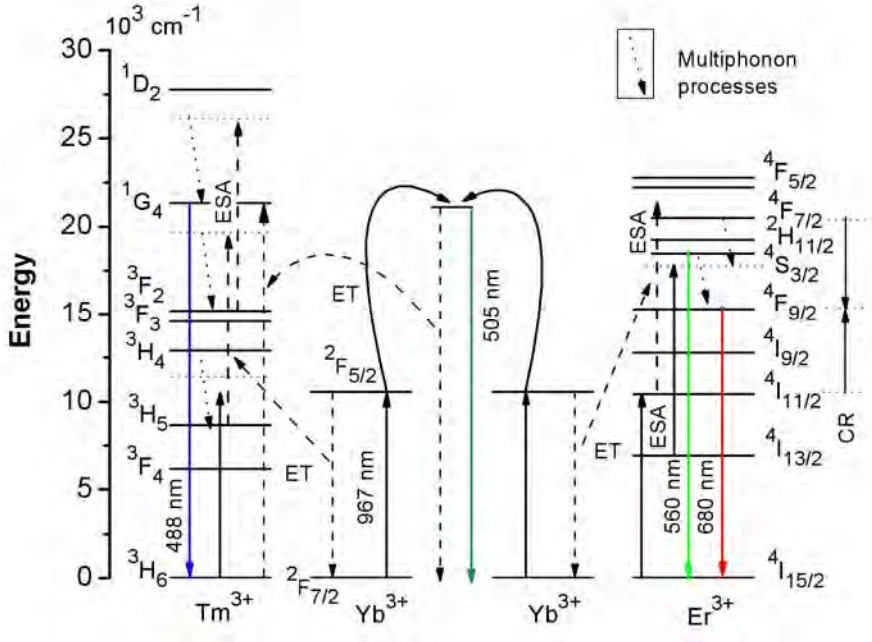

Figure 4.30: Energy levels diagram for the Yb^{3+} system.

4.5.3. Fluorescence decay time of ZrO_2:Yb^{3+} nanocrystals

Decay times of both bands IR and visible (505 nm) diminish as the Yb^{3+} concentration increases (figure 4.31). The ratio $\tau_{cuc}/\tau_{nir} \approx 0.5$ suggests that CUC emission is the result of the simultaneous excitation of both active ions in the molecule Yb–O–Yb; although, such ratio is not maintained as the concentration increases, in fact τ_{nir} decreases faster than τ_{cuc} suggesting that additional processes are presented. Probably the increment of active ions promotes the formation of Yb cluster by ionic interaction in addition to the formation of Yb–O–Yb molecules reducing the NIR emission efficiency faster than the CUC emission produced by molecular interaction. The difference between ionic Yb–Yb and molecular Yb–O–Yb interaction is that the former orbital separation of Yb is larger inducing a poor interaction. In the molecular system the orbital of oxygen atom is overlapped with the orbital of both ions, working as a bridge enhancing the ionic interaction and resulting in strong CUC emission. With the increment of the ion concentration more pairs Yb–O–Yb are formed that in turn diminish both IR and visible emission band. The partial quenching of the IR signal is the result of the decreasing of single Yb ion emission, while the quenching of the visible band is the result of cluster formation of molecules Yb–O–Yb [36]. Clustering, and then fluorescence quenching, of both ions and molecules is confirmed by little deviation at fast time of both visible and infrared emission. Such deviation is small at low concentration but grows as concentration increases (figure 4.32).

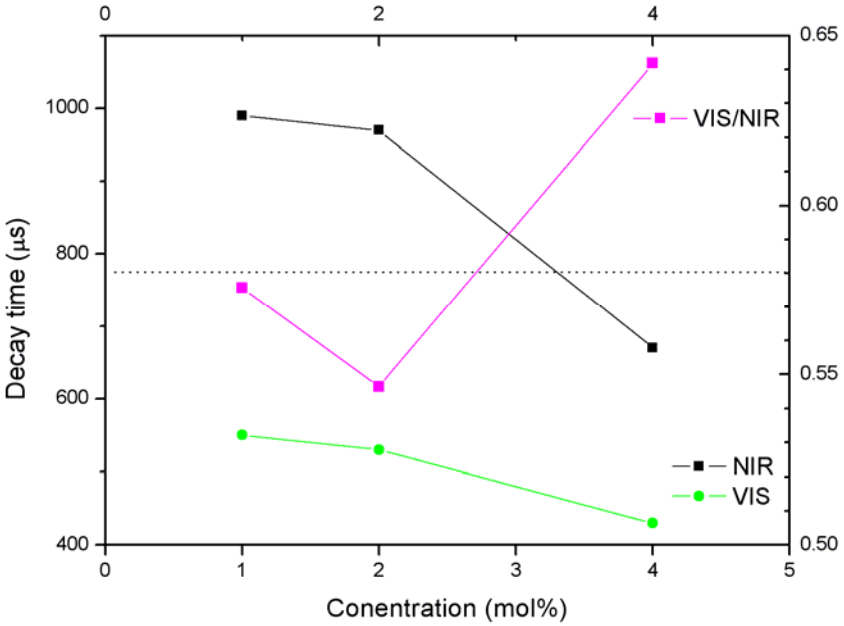

Figure 4.31: Decay times for infrared (NIR) and visible (VIS) bands. NIR /VIS ratio is included.

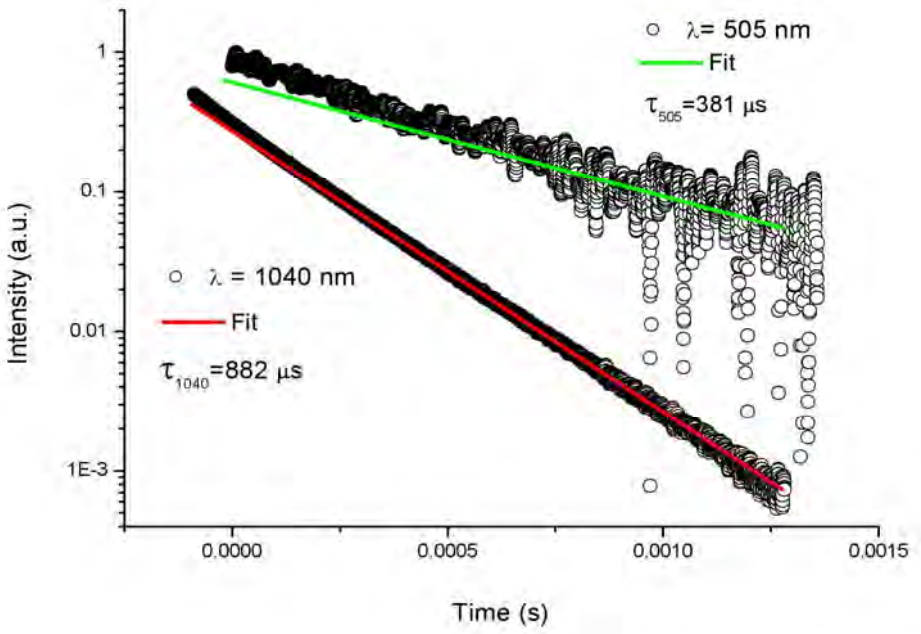

Figure 4.32: Decay times for infrared (NIR) and visible (VIS) bands for ZrO_2:Yb^{3+}(3%) sample.

REFERENCES AND NOTES

[1] E. De la Rosa; L. A. Diaz-Torres; P. Salas; R. A. Rodríguez. *Visible Light emission under UV an IR excitation of rare hearth doped ZrO_2 nanophosphor*. Opt. Mat. **27,** 1320-1325 (2005)

[2] L. A. Diaz-Torres; E. De la Rosa-Cruz; P. Salas; and C. Angeles-Chavez. *Concentration enhanced red upconversion in nanocrystalline ZrO_2:Er under IR excitation.* J. Phys. D: App. Phys. **37**, 2489-2495 (2004)

[3] De la Rosa, E.; Diaz-Torres, L. A.; Rodríguez, R. A.; Meneses-Nava, M. A.; and Barbosa-García, O. *Luminescence and visible upconversion in nanocrystalline ZrO_2:Er^{3+}*. Appl. Phys. Lett. **83**, 4903-05 (2003)

[4] Ramos-Brito, F.; Garcia-Hipolito, M.; Martinez-Martinez, R.; Martinez-Sanchez, E.; and Falcony, C. *Preparation and characterization of photoluminiscent praseodymium-doped ZrO_2 nanostructured powders.* J. Phys. D: Appl. Phys. **37**, L13-16 (2004)

[5] De la Rosa, E.; Diaz-Torres, L. A.; Salas, P.; Castaño, V. M.; and Hernandez, J. M. *Evidence of non-radiative energy transfer from the host to the active ions in monoclinic ZrO_2:Sm^{3+}*. J. Phys. D: Appl. Phys. **34**, L83-6 (2001)

[6] Córdova-Martínez, W; De la Rosa-Cruz, E.; Díaz-Torres, L. A.; Salas, P.; Montoya, A.; Avendaño, M.; Rodríguez, R. A.; and Barbosa-García, O. *Nanocrystalline tetragonal zirconium oxide stabilization at low temperatures by using rare-earth ions: Sm^{3+} and Tb^{3+}*. Opt. Mater. **20**, 263-71 (2002)

[7] Capobianco, J. A.; Vetrone, F.; Boyer, J. C.; Speghini, A.; and Bettinelli, M. *Visible upconversion of Er^{3+} doped nanocrystalline and bulk Lu_2O_3*. Opt. Mater. **19**, 259-68 (2002)

[8] Chen, L.; Liu, Y.; and Li, Y. *Preparation and characterization of ZrO_2:Eu^{3+} phosphors*. J. Alloys Compounds v. **381** (1-2), 266-271 (2004)

[9] Kapoor, R.; Friend, C. S.; Biswas, A.; and Prasad, P-N. *Highly efficient infrared-to-visible energy upconversion in Er^{3+}:Y_2O_3*. Opt. Lett. **25**, 338-40 (2000)

[10] H. A. Mcleod, in: *Thin Film Optical Filters*, second ed., Adam Hilger, Bristol. 1986

[11] I. M. Thomas. *Preparation of dielectric HR mirrors from colloidal oxide suspensions containing organic polymer binders*. SPIE 2288, **50** (1954)

[12] H. Armendáriz; B. Coq; D. Tichit; R. Dutartre; F. Figueras. *Influences of some synthesis parameters and activation procedures on the one-step sol-gel synthesis of sulfated-zirconia catalysts, followed by TG-DSC and mass spectrometry.* J. Catal. **173**, 345-354 (1998)

[13] Z. A. Ansori; R. N. Karekar; R. C. Aiyer. *RC Humidity sensor using planar optical waveguides with claddings of various oxide materials*. Thin Solid Films **305**, 330 (1997)

[14] P. Salas; E. De la Rosa-Cruz; D. Mendoza-Anaya; P. González-Martínez; V. M. Castaño; R. Rodríguez. *High temperature thermoluminescence induced on UV-irradiated tetragonal zirconia prepared by sol-gel* .Mater. Lett. **45**, 241 (2000)

[15] P. K. Sharma; M. H. Jilavi; R. Nass; H. Schmidt. *Tailoring the particle size from μm →nm scale by using a surface modifier and their size effect on the fluorescence properties of europium doped yttria*. J. Lumin. **82**, 187-193 (1999)

[16] R. S. Meltzer; W. M. Yen; H. Zheng; S. P. Feofilov; M. J. Dejneka; B. Tissue; H. B. Yuan. *Effect of the matrix on the radiative lifetimes of rare earth doped nanoparticles embedded in matrices*. J. Lumin. v. **94**& **95**, 217-220 (2001)

[17] G. M. Salley; R. Valiente; H. U. Güdel. *Luminescence upconversion mechanisms in Yb^{3+}–Tb^{3+} systems*. J. Lumin. **94** & **95**, 305–309 (2001)

[18] Fiorenzo Vetrone, et al. *Significance of Yb^{3+} concentration on the upconversion mechanisms in codoped Y_2O_3:Er^{3+}, Yb^{3+} nanocrystals*. J. App. Phys. **96**, 1 (2004)

[19] S. Tanabe; T. Ohyagi; N. Soga; T. Hanada. *Compositional dependence of Judd-Ofelt parameters of Er^{3+} ions in alkali-metal borate glasses*. Phys. Rev. B **46**, 3305-3310 (1992)

[20] M. P. Hehlen; N. J. Cockroft; T. R. Gosnell. *Spectroscopic properties of Er^{3+}- and Yb^{3+}-doped soda-lime silicate and aluminosilicate glasses*. Phys. Rev. B **56**, 9302-9318 (1997)

[21] Bor-Chyuan Hwang; Shibin Jiang; Tao Luo; Jason Watson; Gino Sorbello; Nasser Peyghambarian. *Cooperative upconversion and energy transfer of new high Er^{3+} and Yb^{3+} – Er^{3+} doped phosphate glasses*. J. Opt. Soc. Am. B. **17**, 5, 833-839 (2000)

[22] X. Zou; H. Toratani. *Evaluation of spectroscopic properties of Yb^{3+} –doped glasses*. Phys. Rev. B **52**, 15889-15897 (1995)

[23] V. P. Gapontsev; S. M. Matitsin; A. A. Isineev; V. B. Kravchenko. *Erbium glass lasers and their applications*. Opt. Laser Technol. **14**, 189-196 (1989)

[24] L.A. Diaz-Torres; E. De la Rosa; P. Salas; H. Desirena. *Enhanced cooperative absorption and upconversion in Yb^{3+} doped YAG nanophosphors*. Opt. Mat. **27,** 1305-1310 (2005)

[25] De Vicente, F. S.; De Castro, A. C.; De Souza, M. F.; and Siu Li, M. *Luminiscence and structure of Er^{3+} doped zirconia films deposited by electron beam evaporation*. Thin. Solid Films **418**, 222-7 (2002)

[26] Glauco S. Maciel; Amitava Patra. *Influence of nano environment on luminescence lifetime of Er^{3+}-activated ZrO_2 nanocrystals*. J. Opt. Soc. Am. B, No. **3**, Vol. 21. March 2004

[27] A. Patra; C. S. Friend; R. Kapoor; P. N. Prasad. *Upconversion in Er^{3+}:ZrO_2 Nanocrystals*. J. Phys. Chem. B **106**, 1909-1912 (2002)

[28] M. Takahashi; M. Izuki; R. Kanno; Y. Kawamoto. *Upconversion characteristics of Er^{3+} in transparent oxyfluoride glass-ceramics*. J. Appl. Phys. **83** (7), 3920-3922 (1998)

[29] P. Salas; C. Angeles-Chávez; J. A. Montoya; E. De la rosa; L. A. Diaz-Torres; H. Desirena; A. Martínez; M. A. Romero-Romo; J. Morales. *Synthesis, characterization and luminescence properties of ZrO_2: Yb^{3+} – Er^{3+} nanophosphor*. Opt. Mat. **27**, 1295-1300 (2005)

[30] M. Inokuti and F. Hirayama. *Influence of energy transfer by the exchange mechanism on donor luminescence*. J. Chem. Phys. 43, 1978-1989 (1965)

[31] J. Dong; M. Bass; Y. Mao; P. Deng; F. Gan. *Dependence of the Yb^{3+} emission cross section and lifetime on temperature and concentration in yttrium aluminum garnet*. J. Opt. Soc. Am. B **20**, 1975-1979 (2003)

[32] S. M. Redmond; S. C. Rand; S. L. Oliveira. *Bistable emission of a black-body radiator*. Appl. Phys. Lett. **85**, 5517-5519 (2004)

[33] M. P. Hehlen; A. Kuditcher; S. C. Rand; S. R. Luthi. *Site-Selective, Intrinsically Bistable Luminescence of Yb^{3+} Ion Pairs in $CsCdBr_3$.* Phys. Rev. Lett. **82**, 3050-3053 (1999)

[34] E. Nakazawa; S. Shionoya. *Cooperative Luminescence in $YbPO_4$.* Phys. Rev. Lett. **25**, 1710-1712 (1970)

[35] R. N. Bhargava; D. Gallaghar; X. Hong; A. Nurmikko. *Optical properties of manganese-doped nanocrystals of ZnS.* Phys. Rev. Lett. **72**, 416-149 (1994)

[36] T. Ishii. *First–principles calculations for the cooperative transitions of Yb^{3+} dimer clusters in $Y_3Al_5O_{12}$ and Y_2O_3 crystals.* J. Chem. Phys. **122**, 024705-1 – 024705-6

[37] H. J. Schugar, E. I. Solomon, W. L. Cleveland and L. Goodman. *Simultaneous pair electronic transitions in Yb_2O_3.* J. Am. Chem. Soc. **97:22**, 6442-6450 (1975)

[38] Self auto-convolution and additional modelling of Yb pairs can be consulted on O. Meza. *Pair driven IR fluorescence quenching of Yb^{3+} in ZrO_2:Yb^{3+}*. Master's thesis. Centro de Investigaciones en Óptica. León, Gto., Mexico. July 2006

[39] E. De la Rosa; D. Solis; L. A. Diaz-Torres; P. Salas; C. Angeles-Chavez; O. Meza. *Blue-green emission in ZrO_2:Yb^{3+} nanocrystals*. Submitted for publication

[40] M.A. Noginov, G. B. Loutts, C. S. Steward, B. D. Lucas, D. Fider, V. Peters, E. Mix and G. Hiber. *Spectroscopic study of Yb doped oxide crystals for intrinsic bistability*. J. Lumin. **96**, 129-140 (2002)

Chapter 5

Conclusions and Perspectives

Conclusions

Sixteen ZrO_2 nanocrystalline samples, single and codoped, with different concentrations of Erbium and Ytterbium ions were synthesized by sol-gel method and annealed for 5 h. at 1000 ºC. The structural and morphological characterization showed that the introduction of different ion concentrations affect the crystalline structure stability. ZrO_2: Yb^{3+} (2%), Er^{3+} (1%) codoped sample presented 100% tetragonal phase with a crystallite size of ~ 78 nm. Cubic mixed with tetragonal crystalline structure was obtained for ZrO_2: Yb^{3+} (4%), Er^{3+} (1%) codoped sample and 100 wt% of cubic structure was obtained for samples codoped with Yb^{3+}(4%) or higher concentration. Thus, Yb^{3+} ion affect more strongly to stabilize structures with higher asymmetry. Moreover, ZrO_2: Yb^{3+}, Er^{3+} codoped samples presented a noticeable reduction on residuals which induce minor non-radiative relaxation. The samples were pumped at 968 nm with a semiconductor laser source. The up-converted luminescence properties and the change in the peak intensities of the measured green and red bands were studied. These bands can be ascribed to the $^2H_{11/2}$ + $^4S_{3/2}$ → $^4I_{15/2}$ and $^4F_{9/2}$ → $^4I_{15/2}$ Erbium transitions. With this research work it is expected to have control of the intensity variations of the peaks by changing the Yb^{3+} and Er^{3+} dopant concentrations. Thus, the strongest red emission signal was obtained for the ZrO_2: Yb^{3+} (4%), Er^{3+} (1%) codoped sample and the red and green emission bands had a relationship of 636:100. The ZrO_2: Yb^{3+} (10%), Er^{3+} (1%) sample was suitable for almost pure red emission, with a ratio value of 13.56 times the green emission. Unfortunately the total emission was 80% weaker compared with the strongest measured ZrO_2: Yb^{3+} (2%), Er^{3+} (1%) sample. In codoped samples the red/green ratio is dominated by cross relaxation (CR) process, i.e. ($^2H_{11/2}$ + $^4S_{3/2}$ → $^4I_{9/2}$) + ($^4I_{15/2}$ → $^4I_{13/2}$). For the red enhancement we found that the dopant concentration ratio value was not unique, that is, we found that more than one dopant concentration value ratio for different red enhancement. Therefore we proved that it is possible to control the red/green emission ratio in ZrO_2:Yb^{3+}, Er^{3+} nanophosphors and get enhancement of the red emission.

In single doped Er^{3+} nanocrystals, cross relaxation of type ($^2H_{11/2}$ + $^4S_{3/2}$ → $^4I_{9/2}$) + ($^4I_{15/2}$ → $^4I_{13/2}$) becomes important at higher concentration. Levels $^4I_{9/2}$ and $^4I_{13/2}$ become populated, and level $^4I_{9/2}$ is partly depopulated producing the band centered at 680 nm, and partly relaxed non-radiatively to lower levels $^4I_{11/2}$ and $^4I_{13/2}$. Energy on the $^4I_{13/2}$ level could decay radiatively to ground state or undergoes upconversion promotion above the $^4F_{9/2}$ level via the ET process ($^4I_{13/2}$ + $^4I_{11/2}$) → ($^4F_{9/2}$ + $^4I_{15/2}$) among neighboring ions. In this concentration dependent process, increasing the number of Er^{3+} ions would increase the efficiency of the mechanism that in turn increase red emission from the $^4F_{9/2}$ level and diminish green emission band by quenching the mixed $^2H_{11/2}$ + $^4S_{3/2}$ level. In similar way, in codoped samples the red/green emission ratio is dominated by the CR process.

Perspectives

There are several aspects pending and considered as future work. Aseptic conditions and well control on dosage are important points when synthesizing because it could not be discarded contamination on used tools due to the free handle of them at laboratory and the unavailability of specialized dosing devices. In addition, a scope of new temperature routes is desirable as well as additional cleaning techniques, in order to find a better way of annealing, in which the residuals could be diminished and maintain an acceptable crystal structure stabilization. To control the crystal size and reduce dispersion of size is necessary to consider the applying of surfactants during sol-gel process. This is a broad area of research, hence turning into a time-consuming task. However, obtaining improved excitation dynamics effects on nanocrystals is feasible. Another aspect is the possible alteration of the emission properties due to aging of the synthesized samples, which has to be considered to assert that described phenomena does not change evidently. In the same way, is advisable to do a scan of the excitation wavelength used for pumping; something that could not be implemented by this time. Finally, it is advised a more adequate pre-amplifier when taking decay time measurements as a result of alterations on obtained data. When fitting the data, is notorious the appearance of a secondary slope at the beginning of relaxation of the captured signal; thus some data can not be guaranteed as useful. Also, a practical pulsed laser with will be suitable for more intense analysis.

In my estimation, the purposed objectives in this presented work are considered achieved; though, more pending activities are required to obtain a better description and knowledge of the processes taking place on this nanocrystals.